Design and improvement of magnetic coupling structure for lumped inductive power transfer systems

Amos Onyedikachi Anele

▶ **To cite this version:**

Amos Onyedikachi Anele. Design and improvement of magnetic coupling structure for lumped inductive power transfer systems. Electric power. Université Paris Saclay (COmUE); Tshwane University of Technology, 2016. English. NNT : 2016SACLV038 . tel-01471800

HAL Id: tel-01471800
https://theses.hal.science/tel-01471800

Submitted on 20 Feb 2017

HAL is a multi-disciplinary open access archive for the deposit and dissemination of scientific research documents, whether they are published or not. The documents may come from teaching and research institutions in France or abroad, or from public or private research centers.

L'archive ouverte pluridisciplinaire **HAL**, est destinée au dépôt et à la diffusion de documents scientifiques de niveau recherche, publiés ou non, émanant des établissements d'enseignement et de recherche français ou étrangers, des laboratoires publics ou privés.

université
PARIS-SACLAY

NNT : 2016SACLV038

THESE DE DOCTORAT
DE
L'UNIVERSITE PARIS-SACLAY
PREPAREE A

UNIVERSITÉ DE VERSAILLES SAINT-QUENTIN-EN-YVELINES

ECOLE DOCTORALE N° 580
Sciences et Technologies de l'Information et de la Communication

Spécialité de doctorat (Génie Électrique)

Par

Mr. Amos Onyedikachi ANELE

Conception et amélioration de la structure de couplage magnétique pour des systèmes de transfert de puissance inductive localisés

Thèse présentée et soutenue en salle Casimir, Laboratoire LISV, à Vélizy, le 28/06/2016 :

Composition du Jury :

Professeur des Universités, HRICOVINI Karol, à Cergy-Pontoise/Laboratoire de Physique des Matériaux et des Surfaces - EA 2527 - Cergy-Pontoise - Président
Professeur des Universités, CHASSAGNE Luc, à l'Université de Versailles Saint-Quentin-en-Yvelines/Laboratoire d'Ingénierie des Systèmes de Versailles (LISV) - Vélizy - Directeur de thèse
Professeur des Universités, HAMMAM Yskandar, à l'Université de Technologie de Tshwane - Pretoria (Afrique du Sud) - Co-Directeur de thèse
Professeur des Universités, LINARES Jorge, à l'Université de Versailles Saint-Quentin-en-Yvelines/Laboratoire Groupe d'Etude de la Matière Condensée (GEMAC) - Versailles - Co-Directeur de thèse
Professeur des Universités, DJOUANI Karim, à l'Université de Technologie de Tshwane - Pretoria (Afrique du Sud) - Co-Directeur de thèse
Professeur des Universités, BERNARD Yves, à l'Université Paris Sud 11/Laboratoire de Génie Electrique de Paris - UMR 8507 - Gif/Yvette - Rapporteur
Professeur, DOUMBIA Mamadou Lamine, à l'Université du Québec à Trois-Rivières/Département de Génie Electrique et Informatique - (Québec - Canada) - Rapporteur
Professeur, Augustin MPANDA, à l'ESIEE - Amiens - Examinateur
Professeur des Universités, Yasser ALAYLI, , à l'Université de Versailles Saint-Quentin-en-Yvelines/Laboratoire d'Ingénierie des Systèmes de Versailles (LISV) - Vélizy - Invité

université PARIS-SACLAY
ÉCOLE DOCTORALE
Sciences et technologies de l'information et de la communication (STIC)

Conception et l'amélioration de la structure de couplage magnétique pour des systèmes de transfert de puissance inductive localisées

Mots clés : systèmes IPT, les champs magnétiques, la structure de couplage magnétique , inductance mutuelle

Résumé : Compte tenu du contexte économique du marché des hydrocarbures et les problématiques environnementales, le développement des véhicules électriques (VE) prend de l'ampleur car ils sont considérés comme plus écologiques. Aujourd'hui, les véhicules électriques sont considérés comme une solution favorable pour une énergie plus verte. L'électricité qu'ils consomment peut être générée à partir d'un large éventail de sources qui comprennent les combustibles fossiles, l'énergie nucléaire et les énergies renouvelables. Toutefois, les utilisateurs et les propriétaires de véhicules électriques ont encore des réticences car cela nécessite un stockage d'énergie électrique à bord pour assurer une bonne autonomie.

Le système de transfert de puissance par effet inductif (LIPT en anglais) est une nouvelle technologie qui permet le transfert d'énergie électrique par champ magnétique et un système de bobines primaires et secondaires. Le champ magnétique est un champ haute-fréquence à plusieurs dizaines de kilohertz. Par rapport au système de câble conventionnel, le système LIPT est capable de fournir une recharge qui est pratique mais également efficace des véhicules électriques. Cependant, actuellement son principal facteur limitant est la mauvaise performance de sa structure de couplage magnétique (MCS). L'objectif de cette thèse est d'améliorer la performance des systèmes MCS pour les systèmes de LIPT afin de concevoir des systèmes à meilleur rendement.

Dans un premier temps, sur la base de modèles mathématiques issus de la littérature, un code Matlab a été mis en oeuvre pour calculer l'inductance mutuelle des systèmes de bobines mise en jeu dans le MCS. Puis, le calcul et la validation expérimentale des champs magnétiques entre le primaire et le secondaire a été effectué.

Dans un second temps, un modèle d'un système LIPT pour la charge d'une batterie de véhicule électrique est présenté. Sur la base des spécifications techniques d'une Renault ZOE, les résultats obtenus montrent que, en adaptant la fréquence de la bobine primaire et en compensant avec un système série-série de condensateurs, un système à 3 kW et un système à 22 kW peuvent atteindre des performances permettant la recharge d'une Renault Zoe dans de bonnes conditions.

Enfin, une analyse par éléments finis (FEA) sous COMSOL est développée pour la conception, le calcul et l'optimisation de systèmes MCS plus complexes de nouveaux LIPT. Les modèles de MCS conçus intègrent des bobines d'air évidées avec des configurations appropriées de noyaux magnétiques (par exemple en ferrite), avec des études également sur des parties couvrantes des bobines primaires et secondaires en acier. Les performances des modèles conçus sont déterminées par les valeurs de l'inductance mutuelle et la tension induite qui sont deux critères d'évaluations.

Design and improvement of magnetic coupling structure for lumped inductive power transfer systems

Keywords : IPT systems, magnetic fields, magnetic coupling structure, mutual inductance

Abstract : Taking into account high oil prices and environmental awareness, the development of electric vehicles (EVs) is considered as a healthier mode of transportation. Amongst other eco-friendly vehicles, EVs are considered as a favourable solution for a greener energy because the electricity they consume can be generated from a wide range of sources which include fossil fuel, nuclear power and renewable energy. However, users and owners of EVs feel uncomfortable because EVs require sufficient electrical energy battery storage on-board to provide sufficient driving autonomy.

Lumped inductive power transfer (LIPT) system is a new technology that allows the transfer of electric power between its air-cored primary and secondary coils via a high frequency magnetic field to a consuming device. Unlike the conventional plug-in system, LIPT system is capable of providing a safe, efficient and convenient overnight recharging of EVs. However, its main limiting factor is the poor performance of its magnetic coupling structure (MCS), which is intended to transfer power efficiently. Thus the problem statement of this thesis is to improve the performance of MCS models for LIPT systems.

Firstly, based on a more efficient and relevant mathematical model available in the literature, MATLAB code is implemented to compute the mutual inductance between air-cored filamentary circular (FC) coils. Also, the computation and experimental validation of the magnetic fields between two FC coils are presented.

Furthermore, computational models of an IPT system for EV battery charge are presented in this thesis. Based on the technical specifications of Renault ZOE, the results obtained show that by supplying a higher frequency AC voltage to the primary coil of the MCS and compensating the primary and secondary sides of the air-cored coils with series-series capacitors, the 3 kW single-phase and 22 kW three-phase IPT systems modelled using MATLAB/Simulink are capable of delivering the electricity needed to power the Renault ZOE.

Finally, in order to recommend a suitable and cost-efficient MCS model that can help transfer electric power more efficiently for the battery charging of EVs and E-bikes, a 3-D finite element analysis (FEA) package called COMSOL multiphysics is used to design, compute and investigate a more complex and realistic MCS model of LIPT systems. The designed MCS models incorporate air-cored coils with proper configuration of magnetic cores (e.g ferrite), structural steel covering for the bottom part of the primary coil and top part of the secondary coil and lastly, iron plate which serves as a covering for the primary coil installed underground and the chassis or underbody structure of EVs. The performances of the designed models are determined by the values of the mutual inductance and induced voltage obtained from COMSOL.

Université Paris-Saclay
Espace Technologique / Immeuble Discovery
Route de l'Orme aux Merisiers RD 128 / 91190 Saint-Aubin, France

DECLARATION

"I hereby declare that the thesis submitted for the degree Doctor Technologiae (DTech): Engineering: Electrical, at the Tshwane University of Technology is my own original work and has not previously been submitted to any other institution of higher education. I further declare that all sources cited or quoted are indicated and acknowledged by means of a comprehensive list of references".

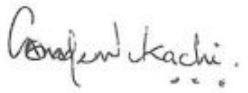

Anele A.O. Date: 29-08-2016

Copyright © University of Paris-Saclay 2016

DEDICATION

This thesis is dedicated to my dearly loved wife, Mrs. Onosetale Blessing Anele, and my daughter, Flourish Onyinyechi Onosetale Anele.

ACKNOWLEDGEMENTS

Firstly, I would like to appreciate my dearest Father, the Almighty GOD, for His love and favour upon my life. Thank You for giving me the ability to successfully complete this research study and thesis writing.

I would also like to express my gratitude and respect to my main supervisor, Prof. Yskandar Hamam (TUT, South Africa). I am delighted to have such an exceptional research Professor as an advisor. I appreciate your availability and motivation during this research study. Thank you, sir, for your excellent supervision and for being an excellent role model. In addition, I would like to appreciate my co-supervisor, Prof. Karim Djouani (TUT, South Africa) for his guidance and support.

I would like to specially thank my main supervisor, Prof. Luc Chassagne (LISV laboratory, UVSQ, France), for his constant kindness towards me. Thank you, sir, for your availability, guidance and support during this research work. Furthermore, I would like to thank my co-supervisor, Prof. Jorge Linares (GEMaC laboratory, UVSQ, France), for his excellent supervision. Thank you, sir, for lending me your brand new Laptop (with a higher RAM) for the accomplishment of the magnetic coupling structure design, computation and analysis. I would like to specially appreciate Prof. Yasser Alayli (LISV laboratory, UVSQ, France) for his excellent supervision. Thank you, sir, for the cotutelle doctoral program offer via Prof. Yskandar Hamam.

I appreciate the Tshwane University of Technology (TUT) and Versailles Engineering Systems Laboratory (LISV), University of Versailles (UVSQ) for the grant given to

me to study for my doctorate degree. I would also like to thank the management staff of the French South African Institute of Technology and Faculty of Engineering and the Built Environment as well as LISV laboratory and the Doctoral School of UVSQ for their administrative and financial assistance.

Finally, I would like to thank my sweetie sweet, Mrs. Onosetale Blessing Anele, my dearly loved parents, Mr Lawrence Anele and Mrs. Christiana Anele as well as my dear parents-in-law, Rev. John Uuijiatalor and his wife, Evg. Mrs. Patricia Uuijiatalor for their prayers, encouragement and patience during this research study.

ABSTRACT

Taking into account high oil prices and environmental awareness, the development of electric vehicles (EVs) is considered as a healthier mode of transportation. Amongst other eco-friendly vehicles, EVs are considered as a favourable solution for a greener energy because the electricity they consume can be generated from a wide range of sources which include fossil fuel, nuclear power and renewable energy. However, users and owners of EVs feel uncomfortable because EVs require sufficient electrical energy battery storage on-board to provide sufficient driving autonomy.

Lumped inductive power transfer (LIPT) system is a new technology that allows the transfer of electric power between its air-cored primary and secondary coils via a high frequency magnetic field to a consuming device. Unlike the conventional plug-in system, LIPT system is capable of providing a safe, efficient and convenient overnight recharging of EVs. However, its main limiting factor is the poor performance of its magnetic coupling structure (MCS), which is intended to transfer power efficiently. Thus the problem statement of this thesis is to improve the performance of MCS models for LIPT systems.

Firstly, based on a more efficient and relevant mathematical model available in the literature, MATLAB code is implemented to compute the mutual inductance between air-cored filamentary circular (FC) coils. Also, the computation and experimental validation of the magnetic fields between two FC coils are presented.

Furthermore, computational models of an IPT system for EV battery charge is presented in this thesis. Based on the technical specifications of Renault ZOE, the results obtained show that by supplying a higher frequency AC voltage to the primary coil of the MCS and compensating the primary and secondary sides of the air-cored coils with series-series capacitors, the 3 kW single-phase and 22 kW three-phase IPT systems modelled using MATLAB/Simulink are capable of delivering the electricity needed to power the Renault ZOE.

Finally, in order to recommend a suitable and an effective MCS model that can help transfer electric power more efficiently for the battery charging of EVs and E-bikes, a 3-D finite element analysis (FEA) package called COMSOL multiphysics is used to design, compute and investigate a more complex and realistic MCS model of LIPT systems. The designed MCS models incorporate air-cored coils with proper configuration of magnetic cores (e.g ferrite), structural steel covering for the bottom part of the primary coil and top part of the secondary coil and lastly, iron plate which serves as a covering for the primary coil installed underground and the chassis or underbody structure of EVs. The performance of the designed models are determined by the values of the mutual inductance and induced voltage obtained from COMSOL.

Contents

LIST OF FIGURES

LIST OF TABLES

ABBREVIATIONS

AC	Alternating Current
DC	Direct Current
DIPT	Distributed Inductive Power Transfer System
E-Bikes	Electric Bikes
EVs	Electric Vehicles
FC	Filamentary Circular
FEA	Finite Element Analysis
HEVs	Hybrid Electric Vehicles
HFCVs	Hydrogen Fuel Cell Vehicles
ICEVs	Internal Combustion Engine Vehicles
IPT	Inductive Power Transfer System
LIPT	Lumped Inductive Power Transfer System
MCS	Magnetic Coupling Structure
RMS	Root Mean Square

Chapter 1

INTRODUCTION

1.1 Background and Justification

Recently, international debates on environmental issues are of major concern to developed countries. As a result, their great priority is to reduce the emissions of greenhouse gases (e.g. carbon dioxide, methane, nitrous oxide and fluorinated gases) in the atmosphere (Wu et al., 2011; Amos et al., 2014b; Anele et al., 2015a). The largest source of greenhouse gas emissions from human activities is from burning fossil fuels for electricity, heat and transportation. Amongst other primary sources of greenhouse gas emissions (e.g. commercial and residential, electricity production, land use and forestry, industry and agriculture), this research study focuses on the transportation system. This is because the transportation sector is the largest consumer of fossil fuel worldwide (Wu et al., 2011; Amos et al., 2013b). Thus cleaning up carbon pollution protects our environment and supports a strong, clean-energy economy.

In order to successfully reduce the amount of carbon pollution that grows rapidly as millions of people gain access to public and personal transportation, automakers are now moving from the manufacturing of internal combustion engine vehicles (ICEVs) to hybrid electric vehicles (HEVs), electric vehicles (EVs) and hydrogen fuel cell vehicles (HFCVs). Amongst other eco-friendly vehicles (e.g. HEVs and HFCVs), EVs are considered as a favourable solution for a greener energy because the electricity they consume can be generated from a wide range of sources which include fossil fuel, nuclear power and renewable energy (e.g. hydroelectricity, wind, solar and biomass) (Amos et al., 2013b, 2014b). However, users and owners of EVs feel uncomfortable because EVs require sufficient electrical energy battery storage on-board to provide sufficient driving autonomy.

Conventional plug-in systems are commonly employed for EV battery charging. However, it presents safety risk in wet conditions (e.g. electrocution due to its exposed charge terminal). Also, its charge terminal may freeze onto the EV during harsh climates and its long cable may be a source of inconvenience to the EV user during charging (Wu et al., 2011; Budhia et al., 2011). Currently, LIPT system is a modern technology that allows the transfer of electric power between its air-cored primary and secondary coils via a high frequency magnetic field to a consuming device (Amos et al., 2014a). LIPT systems have many features which include resistance to chemicals, no residues and no trailing wires. Also, its operation in wet conditions (e.g. water, ice and snow) presents no safety risk and its system is not affected by such conditions; thus it is completely reliable and maintenance-free (Boys & Covic, 2012).

Generally, LIPT system is divided into closely and loosely coupled systems (Budhia et al., 2011). Closely coupled LIPT system operate with relatively small air gaps, but requires user intervention during charging whereas loosely coupled LIPT system operate with relatively large air gaps, and requires no human intervention during charging (Wang et al., 2000; Budhia et al., 2011). Unlike the plug-in system, LIPT system is capable of providing a safe, efficient and convenient overnight recharging of EVs. However, its main limiting factor is the poor performance of its MCS which is intended to transfer power efficiently.

MCS consists of air-cored primary and secondary coils. Its aim is to couple the magnetic flux between its coils so that maximum electrical energy can be transferred to the on-board battery storage system of a consuming device. However, it is faced with the problem of weak coupling due to its coils' separation distance, misalignment (e.g. lateral and angular) and the relatively large leakage reactance associated with its coils (Chopra & Bauer, 2011; Anele et al., 2015a,c,b). Thus the aim of this thesis is to investigate the best design of MCS model for LIPT systems that is suitable and effective for the battery charging of EVs and E-bikes.

1.2 Problem Statement

LIPT system is a modern technology that is capable of providing a safe, efficient and convenient overnight recharging of EVs. However, its main limiting factor is the poor performance of its MCS which is intended to transfer power efficiently. Thus

the problem statement of this thesis is to improve the performance of MCS models for a closely and loosely coupled LIPT systems.

The objective of this thesis is to investigate the best design of MCS for LIPT systems that is suitable and effective for the battery charging of EVs and E-bikes. In order to achieve this aim, the problem statement is divided into four sub-problems. This is done mainly to show the link between each chapter of the thesis, and the connection is presented in the concluding part of each chapter.

1.2.1 Sub-Problem 1

According to (Akyel et al., 2009; Fotopoulou & Flynn, 2011; Babic et al., 2009; Acero et al., 2013; Han & Wang, 2015), the computation of the mutual inductance between the coils is of importance to electrical engineers and physicists because within certain limits of coil separation distance and misalignment (e.g. lateral and angular), a minimal amount of electric power is guaranteed.

Based on a more efficient and general model available in the literature (Akyel et al., 2009; Babic et al., 2009), rederived mathematical models (Anele et al., 2015a) for calculating the mutual inductance between air-cored FC coils with and without misalignment is studied. The computation of the mutual inductance between FC coils arbitrarily positioned with respect to each other (Anele et al., 2015c) is also presented.

1.2.2 Sub-Problem 2

Air-cored coils are widely used in electromagnetic applications. Thus it is vital to measure the magnetic fields around them. According to (Babic & Akyel, 2012; Han & Wang, 2015), it is also important to study the effect of coil separation distance and misalignment on the magnetic fields between air-cored coils.

Based on the relevant model given in (Babic & Akyel, 2012; Akyel et al., 2009), the computation and experimental validation of the magnetic fields between two FC coils (Anele et al., 2015c) are presented in this thesis.

1.2.3 Sub-Problem 3

One of the issues to be solved for EVs to become a success is the technical solution of its charging system (Barth et al., 2011; Subotic & Levi, 2015).

According to the study presented in (Wang et al., 2005; Neves et al., 2011; Chopra & Bauer, 2011; Schmuelling et al., 2012; Koo et al., 2012; Budhia et al., 2013; Musavi & Eberle, 2014; García et al., 2015), the performance of IPT systems for EVs is improved when the relatively large leakage reactance associated with its air-cored coils are compensated with series-series capacitors.

Based on the technical specifications of Renault ZOE, 3 kW single-phase and 22 kW three-phase computational models of an IPT system for EV battery charge (Anele et al., 2015b) are presented in this thesis.

1.2.4 Sub-Problem 4

Sub-problems 1 to 3 deal with a non realistic MCS for LIPT systems. This is because the mathematical models formulated (see sub-problems 1 and 2) and the computational models designed using MATLAB/Simulink (see sub-problem 3) do not incorporate air-cored coils with proper configuration of magnetic cores (e.g ferrite), structural steel covering for the bottom part of the primary coil and top part of the secondary coil and lastly, iron plate which serves as a covering for the primary coil installed underground and the chassis or underbody structure of EVs.

According to (Babic et al., 2009; Budhia et al., 2013; Aditya et al., 2015), it is possible to accurately and rapidly compute the AC magnetic fields, mutual inductance and induced voltage of a more complex and realistic models with the use of FEA packages.

Several MCS models for LIPT systems have been presented in (Covic et al., 2000; Stielau & Covic, 2000; Nakao et al., 2002; Sergeant et al., 2008; Villa et al., 2009; Huang et al., 2009; Budhia et al., 2013; Musavi & Eberle, 2014; Raval et al., 2014; Huang et al., 2015; Kalwar et al., 2015; Aditya et al., 2015). Nonetheless, the aim of this thesis is to investigate the best design of MCS model that is suitable and effective for the battery charging of EVs and E-bikes.

Based on that, COMSOL is used to design, compute and investigate a more complex and realistic MCS model for a closely and loosely coupled LIPT systems.

1.3 Hypothesis of the Study

In this thesis, it is hypothesized that the MCS model for LIPT systems can have a strong AC magnetic field intensity, mutual coupling and induced voltage provided

- a higher frequency AC voltage is supplied to its primary coil.
- the number of turns for its primary and secondary coils are increased.
- the radii of the coils are decreased.
- the reactive parts of the coils are compensated by series-series capacitors.
- its air-cored coils are incorporated with proper configuration of ferrite cores.

MATLAB and COMSOL are used to validate these hypotheses.

1.4 Research Methodology

The following are the systematic study methods employed to achieve the objective of this research work:

- Implementation of MATLAB codes to compute the mutual inductance between air-cored FC coils with and without lateral and angular misalignment, and also the computation of the mutual inductance between FC coils arbitrarily positioned with respect to each other.

- MATLAB computation and experimental validation of the magnetic fields between two FC coils.
- Modelling of 3 kW single phase and 22 kW three phase IPT systems using MATLAB/Simulink.
- 3-D FEA modelling, computation and investigation of a more complex and realistic MCS for a closely and loosely coupled LIPT systems for E-bikes and EVs respectively.

1.5 Delimitations

This research work is delimited as follows.

- The non-conducting magnetic material that covers the coils of the inductive charging system, which is employed for experimental measurement is not considered in the models formulated in chapter 4.
- No experimental results or measurements are implemented to validate the results obtained via MATLAB/Simulink simulations in chapter 5.
- The 3-D FEA modelling, computation and investigation of the MCS for LIPT systems is achieved using COMSOL and no implementation of a physical prototype is constructed. Amongst other air-cored coils, circular cylindrical coil is considered in chapter 6. In addition, leakage magnetic fields are not measured and simulated.

- Magnetic fields is the Physics studied in the MCS model, and it is calculated using AC frequency domain solver. This is because AC/DC module of COMSOL offers a frequency domain form of the magnetic fields interface.

- The more complex and realistic MCS model incorporate air-cored coils with proper configuration of ferrite cores, structural steel covering for the bottom part of the primary coil and top part of the secondary coil and iron plate, which serves as a covering for the primary coil installed underground and the chassis or underbody structure of EVs.

- The performance of the designed MCS models are determined by the values of the mutual inductance and induced voltage obtained from COMSOL.

1.6 Significance of the Study

This research study is worth doing because of the useful and relevant information it provides to electrical engineers and researchers in the field of MCS model development for IPT systems (most especially, case studies for EVs and E-bikes).

1.7 Contribution of the Study

Amongst others, the following research outputs are the contributions made in this research study:

- AO Anele, Y. Hamam, L. Chassagne, J. Linares, Y. Alayli, K. Djouani, "Computation and experimental measurement of the magnetic fields between filamentary circular coils", International Journals for Research Group, 2016.

- AO Anele, Y. Hamam, L. Chassagne, J. Linares, Y. Alayli, K. Djouani, "Computation of the mutual inductance between air-cored coils of wireless power transformer", Journal of Physics Conference Series (4th IC MSquare 2015), June 2015, Mykonos, Greece.

- AO Anele, Y. Hamam, L. Chassagne, J. Linares, Y. Alayli, K. Djouani, "Evaluation of the magnetic fields and mutual inductance between circular coils arbitrarily positioned in space", Journal of Physics Conference Series (4th IC MSquare 2015), June 2015, Mykonos, Greece.

- AO Anele, Y. Hamam, L. Chassagne, J. Linares, Y. Alayli, K. Djouani, "Computational models of an inductive power transfer system for electric vehicle battery charge", Journal of Physics Conference Series (4th IC MSquare 2015), June 2015, Mykonos, Greece.

- Amos O. Anele, Yskandar Hamam, Yasser Alayli, Karim Djouani, "Investigating the impacts of lateral and angular misalignment between circular filament", Journal of Machine to Machine Communications, January 2014.

- Amos O. Anele, Yskandar Hamam, Yasser Alayli, Karim Djouani, "Effects of coil misalignment on the magnetic and magnetic force components between circular filament", Journal of Machine to Machine Communications, Jan. 2014.

- A.O. Anele, Y. Hamam, Yasser Alayli, K. Djouani, "Computation of the mutual inductance between circular filaments with coil misalignment", IEEE AFRICON Conference, September, 2013, Mauritius.

- A.O. Anele, Y. Hamam, Yasser Alayli, K. Djouani, "Effects of misalignment between filamentary circular coils arbitrarily positioned in space", PACT Conference, July, 2013, Lusaka, Zambia.

- A.O. Anele, Y. Hamam, Yasser Alayli, K. Djouani, "Computation of magnetic field and force between circular filaments arbitrarily positioned in space", PACT Conference, July, 2013, Lusaka, Zambia.

1.8 Outline of Thesis

The remainder of this thesis is organized as follows:

Chapter 2: covers literature review on IPT systems for EVs, mutual inductance and magnetic fields computation between air-cored coils, IPT models for EV battery charge and design of MCS models for LIPT systems.

Chapter 3: section 3.2 presents the rederived formulas for calculating the mutual inductance between FC coils with and without lateral and angular misalignment. Section 3.3 presents the computation of the mutual inductance between FC coils arbitrarily positioned in space and lastly, section 3.4 concludes this chapter.

Chapter 4: section 4.2 presents the models for calculating the magnetic flux through the secondary coil, the mutual inductance between the FC coils and the induced voltage in the secondary side of the coil. Section 4.3 presents the formulated model for calculating the magnetic fields between two FC coils. In addition, the computed results obtained for the magnetic fields are validated with experimental measurement. Lastly, section 4.4 concludes this chapter.

Chapter 5: section 5.2 presents the analysis of the IPT transformers and the effects of capacitive compensation. Section 5.3 presents the computational IPT models of 3 kW single phase and 22 kW three phase for EV battery charge and lastly, section 5.4 concludes this chapter.

Chapter 6: section 6.2 presents the MCS model description for E-bikes (closely-coupled LIPT system) and EVs (loosely-coupled LIPT system). Section 6.3 presents the results of the MCS models for E-bikes. Section 6.4 presents the results of the MCS models for EVs. Section 6.5 presents the results of the MCS model with misalignment: a case study for EVs and section 6.6 concludes this chapter.

Chapter 7: presents the concluding remarks of this thesis and recommends possible future research works.

Chapter 2

LITERATURE REVIEW

2.1 Introduction

This chapter covers literature review on IPT systems for EVs, the computation of the magnetic fields and mutual inductance between air-cored coils, IPT models for EV battery charge and design of MCS models for IPT systems.

2.2 Literature Review on IPT Systems for EVs

One of the major priorities of developed countries is to reduce the emissions of greenhouse gases (e.g. carbon dioxide, methane, nitrous oxide and fluorinated gases) in the atmosphere (Wu et al., 2011; Amos et al., 2013c,a; Kim, 2012; Musavi & Eberle, 2014). The primary sources of these emissions include commercial and residential, electricity production, land use and forestry, industry, agriculture and transportation.

The largest source of greenhouse gas emissions from human activities is from burning fossil fuels for electricity, heat and transportation. Based on that information, this research study focuses on the aspect of transportation system. This is because the transportation sector is the largest consumer of fossil fuel worldwide (Wu et al., 2011; Amos et al., 2013b, 2014b).

Cleaning up carbon pollution protects our environment and supports a strong, clean-energy economy. Thus in order to successfully reduce the amount of carbon pollution that grows rapidly as millions of people gain access to public and personal transportation, automakers are now moving from the manufacturing of ICEVs to HEVs, EVs or HFCVs (Wu et al., 2011; Amos et al., 2013b). Amongst other eco-friendly vehicles (e.g. HEVs and HFCVs), EVs are considered as the favourable solution for a greener energy because the electricity they consume can be generated from a wide range of sources which include fossil fuel, nuclear power and renewable energy (e.g. hydroelectricity, wind, solar and biomass) (Amos et al., 2013b, 2014b). However, users and owners of EVs feel uncomfortable because EVs require sufficient electrical energy battery storage on-board to provide sufficient driving autonomy.

Formerly, the transfer of electric power to a moving vehicle is based on conventional plug-in or brush and bar contact methods (Budhia et al., 2011; Agbinya, 2012; Hasanzadeh & Vaez-Zadeh, 2015). The applications of these techniques are cranes, ground floor transportation systems, monorails, elevators, battery charging systems and other transportation systems (Wu et al., 2011; Kalwar et al., 2015). Although these principles are well known and proven, it presents safety risk (e.g. electrocution

due to its exposed charge terminal) in wet conditions (see Fig. 2.1). Also, its charge terminal may freeze onto the EV during harsh climates (e.g. snow) and its long cable may be a source of inconvenience to the EV user during charging (Budhia et al., 2011; Amos et al., 2013b; Wei et al., 2014).

FIGURE 2.1: Conventional plug-in system for EV battery charging (Wu et al., 2011; Amos et al., 2014b)

IPT systems are a modern technology that allow the transfer of electric power between its air-cored primary and secondary coils via a high frequency magnetic field to a consuming device (Wang et al., 2000; Amos et al., 2013b; Subotic & Levi, 2015; Kalwar et al., 2015). It is now recognized as a system that is capable of providing a safe, efficient and convenient overnight recharging of EVs (Budhia et al., 2011). Generally, they are grouped into either a distributed IPT (DIPT) system or lumped IPT (LIPT) system. DIPT systems (see Figs. 2.2a and 2.2b) are employed where

continuous power is needed whereas LIPT systems (see Figs. 2.2c and 2.2d) are utilized for cases where power needs to be transferred at a fixed location (Budhia et al., 2011; Huang et al., 2015). DIPT systems comprise a primary coil that is arranged in a long loop forming a track and one or more secondary coils that couple to a small portion of the track to provide constant power to loads (Wang et al., 2005; Budhia et al., 2011). LIPT systems is based on distinct primary coil and secondary coil, and maximum power transfer is guaranteed when the coils are closely aligned and have sufficient mutual coupling (Covic et al., 2000; Budhia et al., 2013; Auvigne, 2015). LIPT systems are considered to be more suitable than DIPT systems because EVs are generally parked in known fixed locations (e.g. parking lots, taxi ranks and garages) for the recharging of their batteries (Budhia et al., 2011; Mou & Sun, 2015).

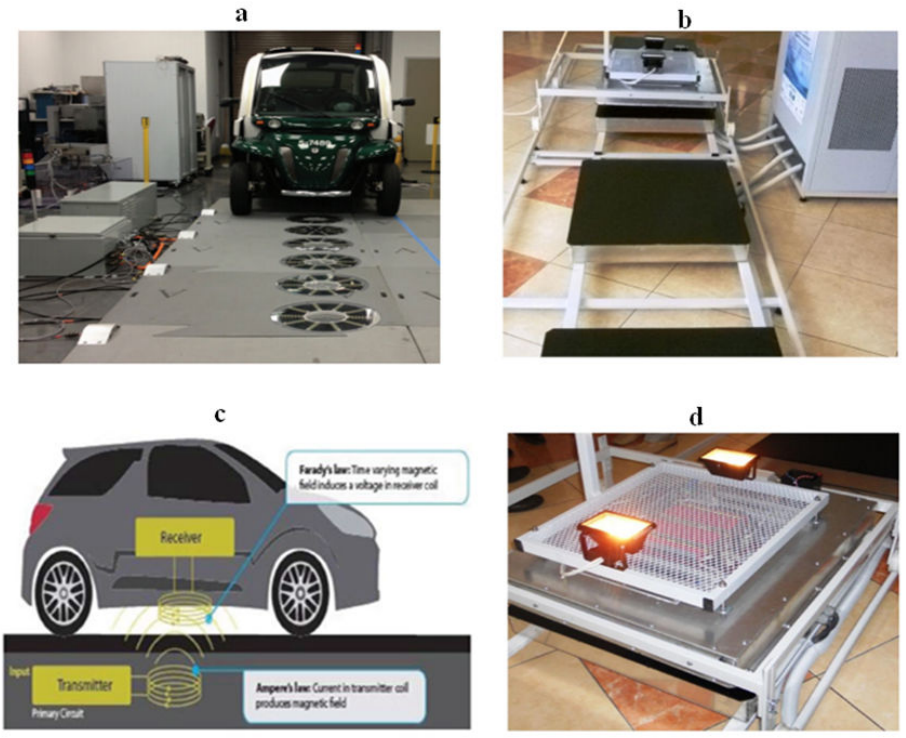

FIGURE 2.2: IPT systems for EV battery charging
Figures (a) and (b) refer to DIPT system whereas (c) and (d) refer to LIPT system (Wu et al., 2011; Amos et al., 2013b; Madzharov & Tonchev; Miller et al., 2014)

According to (Budhia et al., 2011), the capacity of LIPT systems vary from 0.5 W to 50 kW. They can be used to recharge small electronic devices (Kim et al., 2001; Hui & Ho, 2005; Van der Pijl et al., 2006), recreational people movers (Covic et al., 2000), automatic guided vehicles (Hata & Ohmae, 2004; Sergeant et al., 2008) and EVs (Nakao et al., 2002; Laouamer et al., 1997). LIPT systems may be further divided into either closely coupled or loosely coupled LIPT systems. The application of a closely-coupled LIPT system is suitable for early EVs (Klontz et al., 1995; Severns et al., 1996; Dai & Ludois, 2015). In addition, it operates with relatively small air gaps and requires user intervention. Loosely coupled LIPT systems operate with a large air gap and require no user intervention (see Fig. 2.2b). Thus a closely and loosely coupled LIPT systems are the subjects of investigation in this thesis.

2.3 Mutual Inductance Computation

Electric power may be transferred via the MCS of LIPT systems when the magnetic fields generated by the primary coil is partly picked up by the secondary coil (see Fig. 2.2b), but insufficient mutual coupling is obtained due to certain limits of coil separation distance and misalignment (e.g lateral and angular) (Anele et al., 2015a,c; Akyel et al., 2009; Fotopoulou & Flynn, 2011; Babic et al., 2009; Acero et al., 2013; Han & Wang, 2015). Thus the effect of these limits is investigated in this thesis.

The computation of the mutual inductance between air-cored coils is of fundamental practical interests to electrical engineers and researchers in the field of electromagnetic

structures of LIPT systems. Several contributions have been made in the literature concerning the computation of the mutual inductance between air-cored coils. In this view, mathematical modellings based on the application of Maxwell's formula, Neumann's formula, Biot-Savart law, Lorentz and magnetic vector potential have been presented in (Maxwell, 1881; Butterworth, 1916; Snow, 1954; Grover, 1944, 1946; Kim et al., 1997; Akyel et al., 2009; Conway, 2008; Babic et al., 2009; Han & Wang, 2015).

Maxwell was the first to give the formula for two circles whose axes intersect (Maxwell, 1881). Butterworth and Snow gave formulas for circular loops with parallel axes (Butterworth, 1916; Snow, 1954). However, according to (Akyel et al., 2009; Babic et al., 2009), these formulas were slowly convergent and not useable with a wide range of parameters. Based on Butterworths formula, Grover (Grover, 1944, 1946) formulated a more efficient and general model for calculating the mutual inductance between two FC coils with misalignment (see equation (2.1) and Fig. 2.3).

$$M = \frac{2\mu_0}{\pi}\sqrt{R_P R_S}\int_0^{\pi}\frac{[cos\theta - \frac{d}{R_S}cos\phi]\Psi(k)}{k\sqrt{V^3}}d\phi \tag{2.1}$$

where

$\alpha = \frac{R_S}{R_P}$, $\beta = \frac{c}{R_P}$, $\xi = \beta - \alpha cos\phi sin\theta$, $k^2 = \frac{4\alpha V}{(1+\alpha V)^2+\xi^2}$, $\Psi(k) = (1-\frac{k^2}{2})K(k) - E(k)$

$V = \sqrt{1 - cos^2\phi sin^2\theta - 2\frac{d}{R_S}cos\phi cos\theta + \frac{d^2}{R_S^2}}$

$K(k) = \int_0^{\frac{\pi}{2}} \frac{1}{\sqrt{1-k^2 sin^2\theta}}d\theta$ and $E(k) = \int_0^{\frac{\pi}{2}} \sqrt{1-k^2 sin^2\theta}d\theta.$

where μ_0 is the magnetic permeability of free space, R_P and R_S are the radii of the primary and secondary coils respectively, d is the lateral misalignment, α is the shape

factor of the coils' physical geometry, c is the separation distance between the coils' centres, θ is the angular misalignment, k is a variable, parameter $\Psi(k)$ is function of k, ϕ is the angle of integration at any point of the secondary coil, β, V and ξ are dimensionless parameters, $K(k)$ and $E(k)$ are the complete elleptic integral of the first and second kinds respectively.

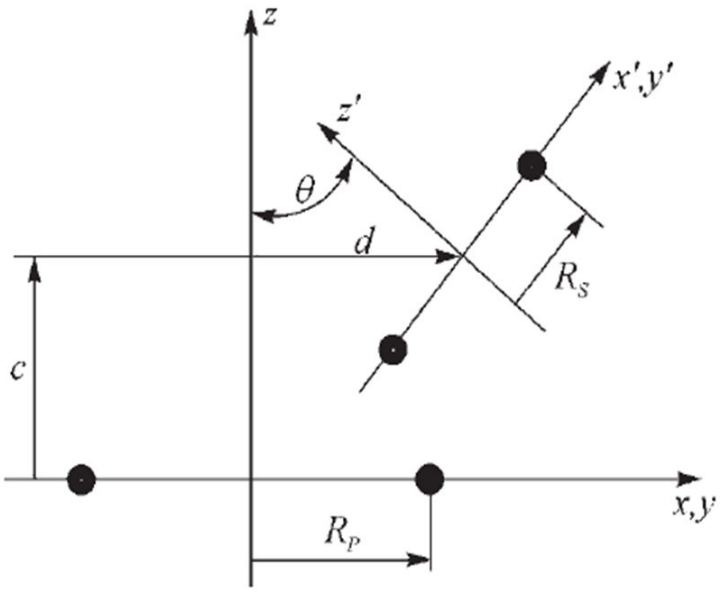

FIGURE 2.3: Filamentary circular coils with misalignment (Akyel et al., 2009)

In order to confirm the validity of the developed model, Kim obtained another mutual inductance model using a semi-analytical method "magnetic vector potential approach" (Kim et al., 1997). However, using the same approach employed by Kim, Babic retrieved Grover's formula through well detailed derivations (Babic et al., 2009). It was discussed that the method simplifies the mathematical procedures for computing the mutual inductance, its associated programming and significantly reduces its computation time. Also, it was shown by Babic that the formula developed by Kim gave misleading results.

2.3.1 Mutual Inductance Model: Coils with Misalignment

Based on section 2.3, rederived mathematical models for calculating the mutual inductance between two FC coils with and without misalignment (e.g. lateral and angular) are presented in this thesis (Anele et al., 2015a). Rather than presenting only numerical results as given in (Babic et al., 2009), the computed results are also graphically implemented using MATLAB codes. Lastly, the results are compared with the ones presented by (Kim et al., 1997; Babic et al., 2009; Conway, 2008).

2.3.2 Mutual Inductance Model: Most General Case

In addition to section 2.3, the formula for calculating the mutual inductance (most general case) between inclined FC coils placed in any position (see Fig. 2.4a) as a function of the primary and secondary coils' radii R_P and R_S, parameters a, b and c defining the centre of the secondary coil and coordinates (x_C, y_C, z_C) defining the centre of the secondary coil is given in (Akyel et al., 2009) as

$$M = \frac{\mu_0 R_S}{\pi} \int_0^{2\pi} \frac{[p_1 cos\varphi + p_2 sin\varphi + p_3]\Psi(k)}{k\sqrt{V_0^3}} d\varphi \tag{2.2}$$

where $\alpha = \frac{R_S}{R_P}$, $\beta = \frac{x_C}{R_P}$, $\gamma = \frac{y_C}{R_P}$, $\delta = \frac{z_C}{R_P}$, $\ell = \sqrt{a^2 + c^2}$, $L = \sqrt{a^2 + b^2 + c^2}$, $p_1 = \pm\frac{\gamma c}{\ell}$, $p_2 = \mp\frac{\beta\ell^2 + \gamma ab}{\ell L}$, $p_3 = \frac{\alpha c}{L}$, $p_4 = \mp\frac{\beta ab - \gamma\ell^2 + \delta bc}{\ell L}$, $p_5 = \mp\frac{\beta c - \delta a}{\ell}$, $k = \sqrt{\frac{4V_0}{A_0 + 2V_0}}$, $\Psi(k) = (1 - \frac{k^2}{2})K(k) - E(k)$, $A_0 = 1 + \alpha^2 + \beta^2 + \gamma^2 + \delta^2 + 2\alpha(p_4 cos\varphi + p_5 sin\varphi)$,

$V_0^2 = \alpha^2[(1-\frac{b^2c^2}{\ell^2L^2})cos^2\varphi + \frac{c^2}{\ell^2}sin^2\varphi + \frac{abc}{\ell^2L}sin2\varphi] + \beta^2 + \gamma^2 \mp 2\alpha\frac{\beta ab - \gamma\ell^2}{\ell L}cos\varphi \mp \frac{2\alpha\beta c}{\ell}sin\varphi,$

$K(k) = \int_0^{\frac{\pi}{2}} \frac{1}{\sqrt{1-k^2sin^2\theta}}d\theta$ and $E(k) = \int_0^{\frac{\pi}{2}} \sqrt{1-k^2sin^2\theta}d\theta.$

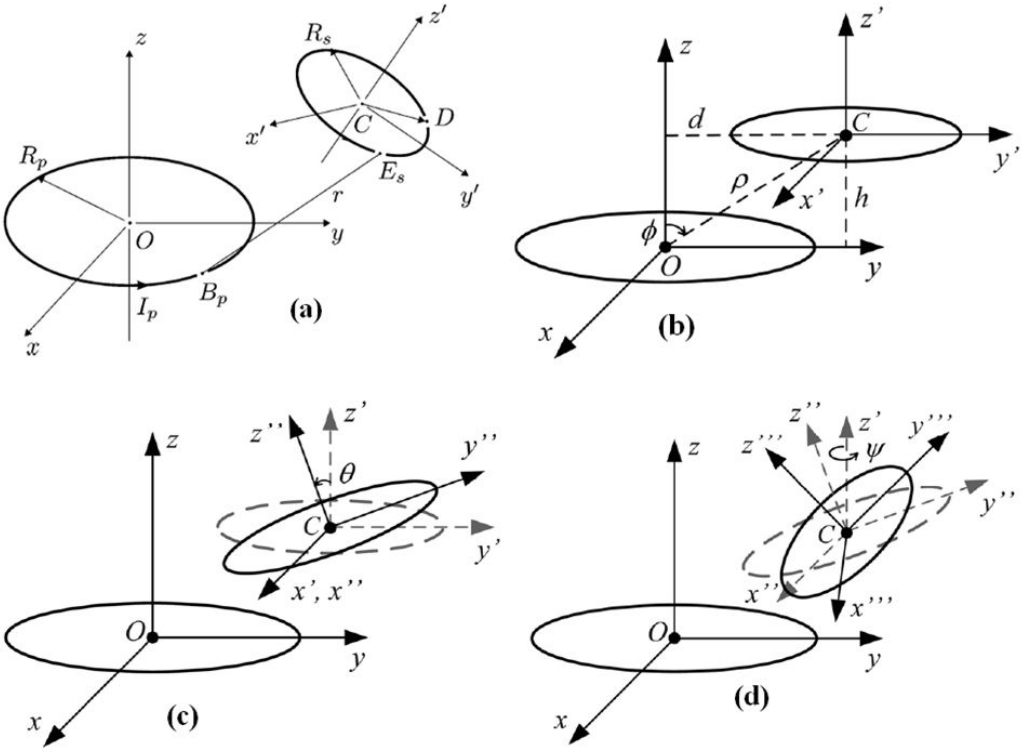

FIGURE 2.4: Geometric configurations and common notation
(a) Circular coils with arbitrary misalignment. The geometric configurations and common notation used in the examples studied in (Akyel et al., 2009) correspond to the following cases: (b) lateral misalignment only ($\theta = 0$, $\psi = 0$, axes $y - z$ and $y' - z'$ are coplanar), (c) lateral and angular misalignment ($\psi = 0$, axes $y - z$ and $y' - z'$ are coplanar) and (d) arbitrary lateral and angular misalignment (no coplanar axes anymore).

where μ_0 is the magnetic permeability of free space, k is a variable, parametr $\Psi(k)$ is function of k, α, β, γ, ℓ, L, p_1, p_2, p_3, p_4, p_5, A_0 and V_0 are dimensionless parameters, φ is the angle of integration at any point of the secondary coil, $K(k)$ and $E(k)$ are the complete elliptic integral of the first and second kinds respectively.

Based on the model given in equation (2.2), MATLAB code is implemented to compute the mutual inductance between two FC coils arbitrarily positioned with respect

to each other (Anele et al., 2015c). Also, the computed results are compared with the numerical results previously published in (Akyel et al., 2009; Grover, 1944).

2.4 Magnetic Fields: Computation and Validation

According to (Babic & Akyel, 2012), the magnetic fields in an arbitrary point $Es(x_S, y_S, z_S)$ produced by the primary coil of the radius R_P carrying the current I_P (see Fig. 2.4a) is given by

$$\begin{aligned} B_x(x_S, y_S, z_S) &= -\frac{\mu_0 I_P z_S x_S k}{8\pi\sqrt{R_P}(x_S^2 + y_S^2)^{5/4}} L_0 \\ B_y(x_S, y_S, z_S) &= -\frac{\mu_0 I_P z_S y_S k}{8\pi\sqrt{R_P}(x_S^2 + y_S^2)^{5/4}} L_0 \\ B_z(x_S, y_S, z_S) &= -\frac{\mu_0 I_P k}{8\pi\sqrt{R_P}(x_S^2 + y_S^2)^{3/4}} S_0 \end{aligned} \tag{2.3}$$

where $x_S = x_C + R_S u_x cos\varphi + R_S v_x sin\varphi$, $y_S = y_C + R_S u_y cos\varphi + R_S v_y sin\varphi$, $z_S = z_C + R_S u_z cos\varphi + R_S v_z sin\varphi$, $\overrightarrow{u} = [u_x, u_y, u_z] = [-\frac{ab}{\ell L}, \frac{\ell}{L}, -\frac{bc}{\ell L}]$, $\overrightarrow{v} = [v_x, v_y, v_z] = [-\frac{c}{\ell}, 0, \frac{a}{\ell}]$, $L_0 = 2K(k) - \frac{2-k^2}{1-k^2}E(k)$, $S_0 = 2\sqrt{x_S^2 + y_S^2}K(k) - \frac{2\sqrt{x_S^2+y_S^2} - (R_P + \sqrt{x_S^2+y_S^2})k^2}{1-k^2}E(k)$, $k^2 = \frac{4R_P\sqrt{x_S^2+y_S^2}}{(R_P+\sqrt{x_S^2+y_S^2})^2+z_S^2}$

x_S, y_S and z_S are the parametric coordinates of the secondary coil, $\overrightarrow{u}$ is the unit vector lying in the secondary coil plane between points C and D, $\overrightarrow{v}$ is the cross product of the unit vector of the axis z' and $\overrightarrow{u}$, S_0 and L_0 are dimensionless parameters whereas $K(k)$ and $E(k)$ are the complete elliptic integrals of the first and second kinds respectively.

Based on equation (2.3), the computation and experimental validation of the magnetic fields between two FC coils are presented in this thesis (Anele et al., 2015c).

2.5 IPT Models for EV Battery Charge

One of the issues to be solved for EVs to become a success is the technical solution of its charging system (Wang et al., 2005; Neves et al., 2011; Chopra & Bauer, 2011; Schmuelling et al., 2012; Koo et al., 2012; Khaligh & Dusmez, 2012; Barth et al., 2011; Budhia et al., 2013; Musavi & Eberle, 2014; Anele et al., 2015b; Subotic & Levi, 2015; García et al., 2015).

The aim of the MCS model for LIPT systems is to transfer maximum power to the on-board battery storage system of EVs. However, it is faced with the problem of weak coupling (i.e., it suffers from poor efficiency) due to the relatively large leakage reactance associated with its primary and secondary coils (Neves et al., 2011; Koo et al., 2012; Musavi & Eberle, 2014; Anele et al., 2015b).

According to (Wang et al., 2005; Barth et al., 2011; Schmuelling et al., 2012; Neves et al., 2011; Chopra & Bauer, 2011; García et al., 2015; Anele et al., 2015b), it is discussed that the performance of the MCS model for LIPT systems can be improved by compensating the reactive parts of the air-cored coils with capacitors. Furthermore, it is mentioned that series-series (SS) compensating technique is preferred amongst others such as parallel-series (PS), series-parallel (SP) and parallel-parallel (PP). This is because SS capacitor technique helps to improve the power transfer capability of

the transmission line due to its partial compensation of the series leakage reactances. Thus the maximum power transfer efficiency via the MCS to the on-board battery storage system of EVs is improved.

Based on the technical specifications of Renault ZOE, 3 kW single-phase and 22 kW three-phase computational models of an IPT system for EV battery charge (Anele et al., 2015b) are presented in this thesis.

2.6 Magnetic Coupling Structure of LIPT Systems

The main limiting factor of a closely and loosely coupled LIPT systems is the poor performance of its MCS which is intended to transfer power efficiently. Thus the problem statement of this thesis is to improve the performance of MCS models for LIPT systems. MCS consists of air-cored coils, and its aim is to couple the magnetic flux between its primary and secondary coils so that maximum electrical energy can be transferred to the on-board battery storage system of a consuming device (e.g. E-bikes, EVs etc). However, it is faced with the problem of weak coupling due to its coils' separation distance, misalignment (e.g. lateral and angular) and the relatively large leakage reactance associated with its coils (Budhia et al., 2011; Anele et al., 2015a,c,b; Subotic & Levi, 2015; Kalwar et al., 2015; Agbinya, 2012).

Sections 2.3 to 2.5 deal with a non realistic MCS model for LIPT systems. This is because the models presented do not incorporate air-cored coils with magnetic core materials (e.g. ferrite). According to (Babic et al., 2009; Budhia et al., 2013; Aditya

et al., 2015), it is possible to accurately and rapidly compute the AC magnetic fields, mutual inductance and induced voltage of a more complex and realistic models with the use of FEA packages. Several MCS models for LIPT systems have been presented in (Covic et al., 2000; Stielau & Covic, 2000; Nakao et al., 2002; Sergeant et al., 2008; Villa et al., 2009; Huang et al., 2009; Budhia et al., 2013; Musavi & Eberle, 2014; Raval et al., 2014; Huang et al., 2015; Kalwar et al., 2015; Aditya et al., 2015).

Ferrite core couplers for inductive chargers was presented by (Nakao et al., 2002). It was discussed that some researchers have reported the possibility of efficient and large power transmission using large ferrite core discs. However, practical usage requires lighter disc weight and greater side lag allowance between the feeder and receiver discs of a coupler. In (Budhia et al., 2011), Budhia discussed that the magnetic structures of LIPT systems for EVs can be made to be lower cost, more robust and lighter than commonly used inductive couplers which include pot cores, U-shaped cores, ferrite discs or plates and E-cores. It was further dicusssed that these conventional techniques are comparatively fragile and expensive due to the geometry of the large pieces of ferrite required to achieve the desired flux path. Thus the design and optimization of circular magnetic structures for lumped inductive power transfer systems was presented in (Budhia et al., 2011). 3-D FEA (JMAG) modeling was used to optimize the circular power pads. It was discussed that the technique employed for modelling is viable, since measured and simulated results differ by 10%. However, the MCS model designed using JMAG does not incorporate the EV underbody structure and proper configuration of ferrite cores.

The design considerations for variable coupling lumped coil systems was presented in (Huang et al., 2015). Huang investigated the impact of coupling variations and reflected impedance on the overall system behaviour of an IPT lumped coil system. However, the IPT model designed does not take into consideration the non-conducting magnetic material that covers the coils, the chassis of EV and ferrite cores. In (Aditya et al., 2015), modelling and calculation of key design parameters for an inductive power transfer system using finite element analysis was presented. However, the study carried out is for a non realistic case of LIPT systems for EVs.

Thus to achieve the objective of this thesis which is to investigate the best design of MCS model for LIPT systems that is suitable and effective for the battery charging of EVs and E-bikes, COMSOL multiphysics software is used to design, compute and analyse a more complex and realistic MCS model for a closely and loosely coupled LIPT systems (case studies for E-bikes and EVs respectively). Unlike the scientific papers cited, the designed models incorporate air-cored coils with proper configuration of ferrite cores, structural steel covering for the bottom part of the primary coil and top part of the secondary coil as well as iron plate which serves as a covering for the primary coil installed underground and the chassis or underbody structure of EVs. Furthermore, the design, computation and analysis of the MCS model with misalignment (both lateral and angular) are presented. Lastly, the performance of the designed models are determined by the values of the mutual inductance and induced voltage obtained from COMSOL.

Chapter 3

MUTUAL INDUCTANCE MODELLING and COMPUTATION

3.1 Introduction

In this chapter, section 3.2 presents the rederived formulas for calculating the mutual inductance between FC coils with and without lateral and angular misalignment (Anele et al., 2015a). Section 3.3 presents the computation of the mutual inductance between FC coils arbitrarily positioned in space (Anele et al., 2015c) and lastly, section 3.4 concludes this chapter.

3.2 Mutual Inductance: Coil with Misalignment

In equation (2.1), the number of turns for the primary and secondary coils (i.e., N_P and N_S) are not expressed. Thus taking N_P and N_S into account, the rederived

models of equation (2.1) are given in the following subsections:

3.2.1 Case 1: without Coil Misalignment

Figure 3.1 shows the case where the secondary coil has no lateral and angular misalignment (i.e., $d = 0$ and $\theta = 0$). Thus the rederived model for this case is

$$M = \frac{2\mu_0 N_P N_S}{\pi}\sqrt{R_P R_S}\int_0^{\pi}\frac{\Psi(k)}{k}d\phi \tag{3.1}$$

where

$\alpha = \frac{R_S}{R_P}$, $\beta = \frac{c}{R_P}$, $\xi = \beta$, $k^2 = \frac{4\alpha}{(1+\alpha)^2+\xi^2}$, $\Psi(k) = (1 - \frac{k^2}{2})K(k) - E(k)$, $K(k) = \int_0^{\frac{\pi}{2}} \frac{1}{\sqrt{1-k^2 sin^2\theta}}d\theta$ and $E(k) = \int_0^{\frac{\pi}{2}} \sqrt{1-k^2 sin^2\theta}d\theta$.

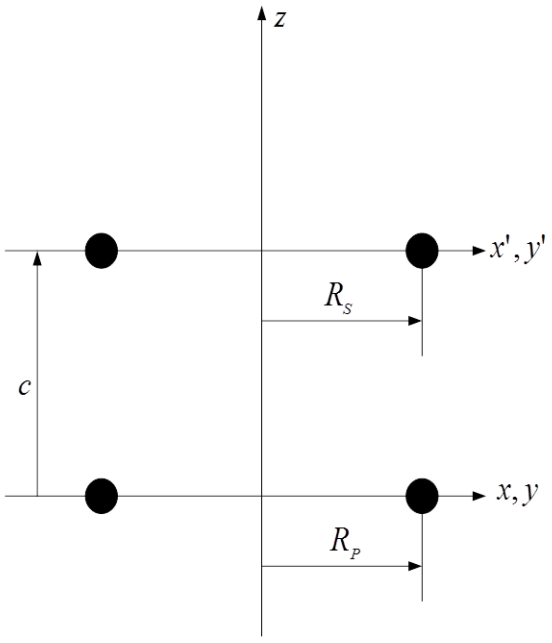

FIGURE 3.1: Case 1: without coil misalignment
(Anele et al., 2015a)

3.2.2 Case 2: Coil with only Lateral Misalignment

Figure 3.2 shows the case where the secondary coil has only lateral misalignment (i.e., $\theta = 0$). Thus the rederived model for this case is

$$M = \frac{2\mu_0 N_P N_S}{\pi}\sqrt{R_P R_S}\int_0^{\pi}\frac{[1-\frac{d}{R_S}cos\phi]\Psi(k)}{k\sqrt{V^3}}d\phi \tag{3.2}$$

where

$\alpha = \frac{R_S}{R_P}, \quad \beta = \frac{c}{R_P}, \quad \xi = \beta, \quad k^2 = \frac{4\alpha V}{(1+\alpha V)^2+\xi^2}, \quad \Psi(k) = (1-\frac{k^2}{2})K(k) - E(k)$

$K(k) = \int_0^{\frac{\pi}{2}}\frac{1}{\sqrt{1-k^2 sin^2\theta}}d\theta, \quad E(k) = \int_0^{\frac{\pi}{2}}\sqrt{1-k^2 sin^2\theta}d\theta \quad \text{and} \quad V = \sqrt{1-2\frac{d}{R_S}cos\phi+\frac{d^2}{R_S^2}}$

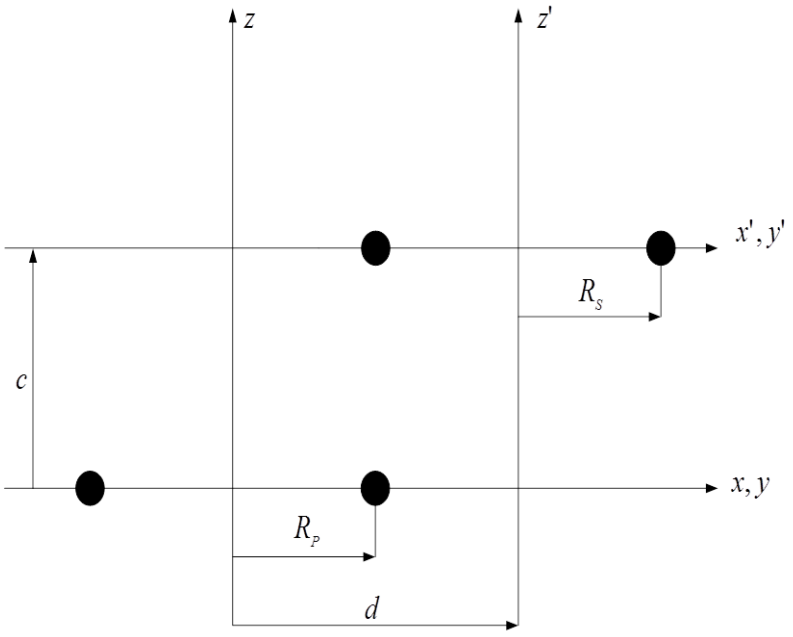

FIGURE 3.2: Case 2: coil separation distance with only lateral misalignment (Anele et al., 2015a)

3.2.3 Case 3: Coil with only Angular Misalignment

Figure 3.3 shows the case where the secondary coil has only angular misalignment (i.e., $d = 0$). Thus, the rederived model for this case is

$$M = \frac{2\mu_0 N_P N_S}{\pi}\sqrt{R_P R_S}\, cos\theta \int_0^{\pi} \frac{\Psi(k)}{k\sqrt{V^3}} d\phi \tag{3.3}$$

where

$\alpha = \frac{R_S}{R_P}$, $\beta = \frac{c}{R_P}$, $\xi = \beta - \alpha cos\phi sin\theta$, $k^2 = \frac{4\alpha V}{(1+\alpha V)^2+\xi^2}$, $\Psi(k) = (1-\frac{k^2}{2})K(k) - E(k)$

$V = \sqrt{1 - cos^2\phi sin^2\theta}$, $K(k) = \int_0^{\frac{\pi}{2}} \frac{1}{\sqrt{1-k^2 sin^2\theta}} d\theta$ and $E(k) = \int_0^{\frac{\pi}{2}} \sqrt{1 - k^2 sin^2\theta} d\theta$

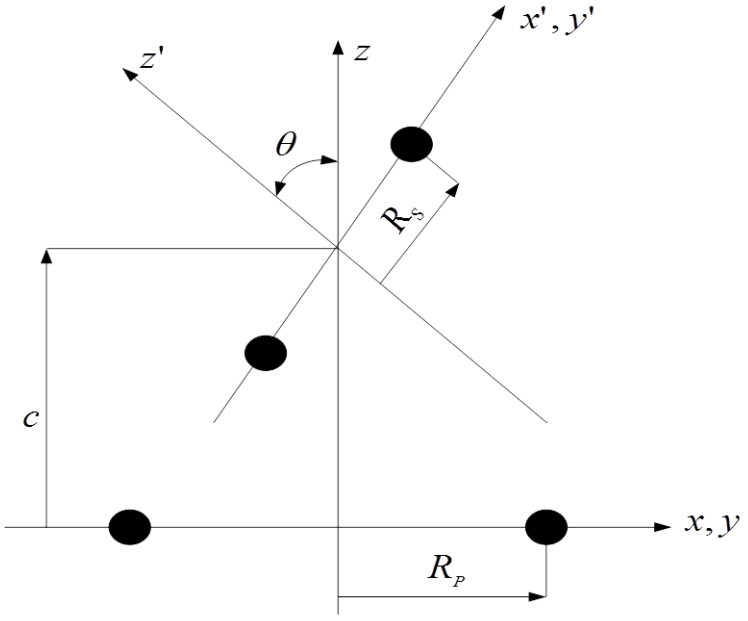

FIGURE 3.3: Case 3: coil separation distance with only angular misalignment (Anele et al., 2015a)

3.2.4 Case 4: Coil with Lateral and Angular Misalignment

Figure 2.3 shows the case where the secondary coil has both lateral and angular misalignment. Thus taking N_P and N_S into account, the rederived model for this case is given by

$$M = \frac{2\mu_0 N_P N_S}{\pi}\sqrt{R_P R_S}\int_0^{\pi}\frac{[cos\theta - \frac{d}{R_S}cos\phi]\Psi(k)}{k\sqrt{V^3}}d\phi \tag{3.4}$$

where the constant parameters and variables are already given in equation (2.1).

3.2.5 Presentation and Discussion of Results

Two or more coils are said to have the property of "Mutual Inductance" when they are magnetically linked together by a common magnetic flux. Thus the results obtained for the computation of the mutual inductance between FC coils with and without lateral and angular misalignment are shown in Figs. 3.4 - 3.7. The graphical implementation of these results is achieved by using MATLAB simulation software to calculate the rederived models given in equations (3.1), (3.2), (3.3) and (3.4). Also, the results presented in this section are compared with those of (Babic et al., 2009; Kim et al., 1997), and the parameters (see Table 3.1) used to achieve these results are based on the example treated in (Babic et al., 2009).

Mutual inductance is very much dependent upon the relative positions or spacing of the coils, and in all cases (see Figs. 3.4 - 3.7), the results obtained show that as the values of the coil separation distance and misalignment increase the mutual

inductance between the coils decrease. Furthermore, based on the example solved in (Babic et al., 2009), the dependence of the mutual inductance on the separation distance "c" was calculated for different values of the lateral misalignment "d" (see Table 3.1). Figure 3.5 and Table 3.1 are used to validate the results presented in (Kim et al., 1997; Babic et al., 2009). Although different values of coil separation distance (i.e., $c = 0,\ 0.05\ m$ and $0.1\ m$) are studied in this thesis, the authors of (Kim et al., 1997) and (Babic et al., 2009) focused only on $c = 0$.

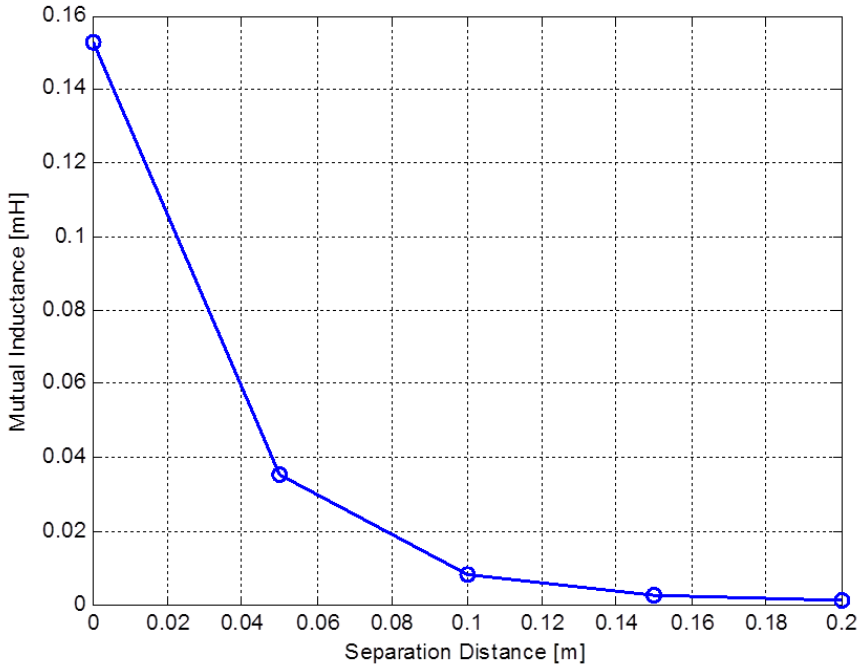

FIGURE 3.4: Mutual inductance computation without coil misalignment
Case 1: coil separation distance only (see Fig. 3.1)

According to (Babic et al., 2009; Anele et al., 2015a), Fig. 3.5 and Table 3.1 show that from lateral misalignment $d = 0$ to $15.5\ mm$ (i.e., for the cases where the secondary coil is located inside the primary coil; this statement can be justified by comparing the diameters of the primary and secondary coils), the value of the M increases from

$\approx 0.153\ mH$ to $\approx 0.182\ mH$. However, there are discrepancies compared to the results presented by (Kim et al., 1997). In addition, from $d = 69.5\ mm$ to $1000\ mm$ (i.e., the region where the secondary coil is located outside the primary coil), negative values are obtained for M, and for larger d the values of M approached zero.

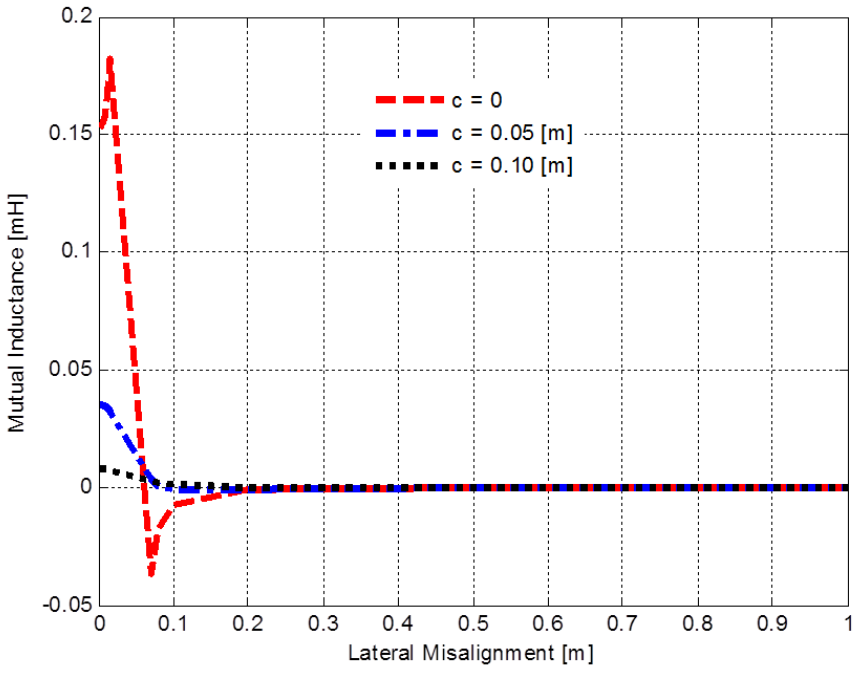

FIGURE 3.5: Mutual inductance computation versus lateral misalignment
Case 2: coil separation distance with only lateral misalignment (see Fig. 3.2)

TABLE 3.1: Example studied in (Babic et al., 2009; Anele et al., 2015a)

$R_P = 42.5\ mm,\quad R_S = 20.0\ mm,\quad N_P = 150,\quad N_S = 50$

$d\ (mm)$	$c\ (mm)$	$M\ (10^{-4}H)$ (Babic et al., 2009)	$M\ (10^{-4}H)$ (Anele et al., 2015a)	$M\ (10^{-4}H)$ (Kim et al., 1997)	Discrepancy
0.0	0	1.529	1.529	1.529	0.000
1.0	0	1.530	1.530	1.531	0.001
2.5	0	1.535	1.535	1.540	0.005
5.0	0	1.552	1.552	1.576	0.024
7.0	0	1.576	1.576	1.623	0.047
10.0	0	1.630	1.630	1.729	0.099
15.0	0	1.793	1.793	2.026	0.233
15.5	0	1.816	1.816	2.066	0.250
69.5	0	−0.364	−0.364	1.579	1.943
80.0	0	−0.178	−0.178	1.051	1.229
100.0	0	−0.072	−0.072	0.610	0.682
200.0	0	−0.007	−0.007	0.138	0.145
500.0	0	0.000	0.000	0.022	0.022
1000.0	0	0.000	0.000	0.005	0.005

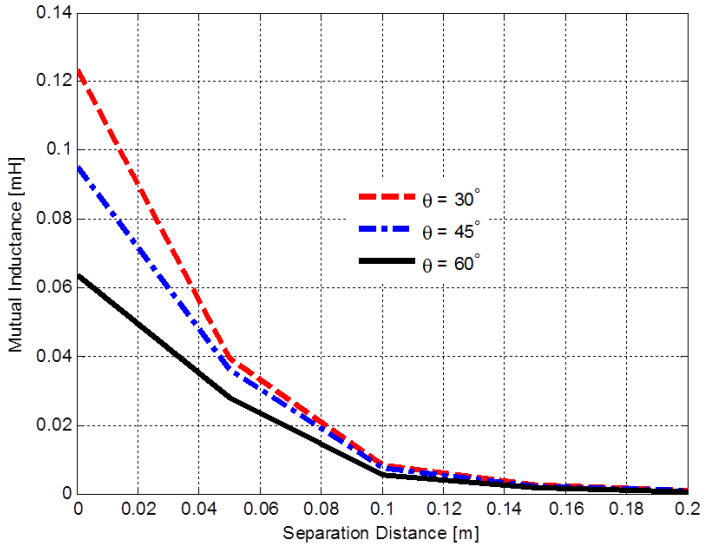

FIGURE 3.6: Mutual inductance computation versus angular misalignment
Case 3: coil separation distance with only angular misalignment "θ" (see Fig. 3.3)

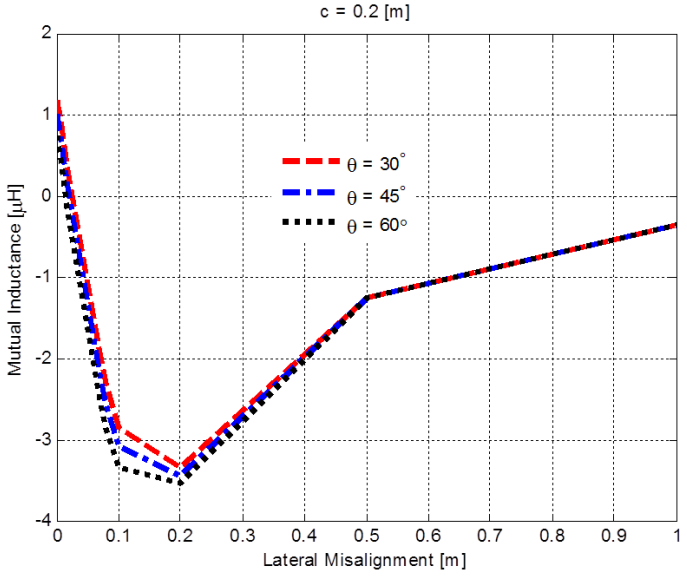

FIGURE 3.7: Mutual inductance computation versus both misalignment
Case 4: coil separation distance of 0.2 $[m]$ with both misalignment (see Fig. 2.3)

Furthermore, it can be seen in Fig. 3.5 and Table 3.1 that with the increase in lateral misalignment (see $d = 69.5\ mm$ to $200\ mm$) for $c = 0$, the mutual inductance drops quickly to zero and then to negative. The negative value of M can be explained by

the magnetic flux cancellation theory when the two coils that are far away partly overlapped such that the magnetic flux generated by the primary and secondary coils partly cancels each other so that their mutual inductance is negative (Liu & Hui, 2007; Su et al., 2009). Thus the results obtained in this section confirm with the authors of (Babic et al., 2009; Anele et al., 2015a) that the mutual inductance model formulated by (Kim et al., 1997) is wrong.

3.3 Mutual Inductance Model: Most General Case

3.3.1 Geometric Configurations and Common Notations

The geometric configurations considered in the examples studied in (Akyel et al., 2009) are shown in Figs. 2.4b to 2.4d. In order to have easier link with Grover's formula, the geometric configurations are restated in terms of a common notation namely: $h = z_C$, $d = \sqrt{x_C^2 + y_C^2}$, $\rho = \sqrt{h^2 + d^2}$, $cos\phi = \frac{h}{\rho}$. Also, in all cases, the primary coil is located in plane XOY, with its centre at the origin $O(0, 0, 0)$. The horizontal and vertical distances between the centres of the coils are d and h respectively and ρ is the lateral misalignment.

Based on example 12 (Akyel et al., 2009), in order to achieve the computation of the mutual inductance between FC coils arbitrarily positioned in space, the following common notations are substituted in equation (2.2):

- The centre of the secondary coil must be taken at point $C(x_C = 0, y_C = d, z_C = h)$ where $d = x_2 sin\theta$, $h = x_1 - x_2 sin\theta$ and $\rho = \sqrt{h^2 + d^2}$. It is vital to note that x_1 is the vertical distance when axis z'' intersects with axis z from origin O, x_2 is the distance between the intersection and the centre of the secondary coil and θ is the angular misalignment.

- The parameters defining the positioning of the secondary coil plane is that of a spherical Cartesian system of coordinates which is given by: $a = sin\psi sin\theta$, $b = -cos\psi sin\theta$ and $c = cos\theta$. where ψ is the rotation angle around axis z', which gives the complete positioning of the secondary coil.

3.3.2 Presentation and Discussion of Results

The graphical and numerical results obtained for the mutual inductance between FC coils with arbitrary lateral ρ and angular θ misalignment are shown in Fig. 3.8 and Table 3.2. Based on the parameters given in example 12 (i.e., $R_P = 16\ cm, R_S = 10\ cm,\ x_1 = 20\ cm$ and $x_2 = 5\ cm$), MATLAB software is used to achieve the coding and computation of equation (2.2).

Although the authors of (Akyel et al., 2009) studied only for the case with $\theta = 60°$ and $\rho = 0.180\ m$, cases for $\theta = 30°,\ \rho \approx 0.160\ m$ and $\theta = 45°,\ \rho \approx 0.170\ m$ are also studied in this thesis (see Fig. 3.8 and Table 3.2).

In the case with $\theta = 60°$ and $\rho = 0.180\ m$, Fig. 3.8 shows that the value of the mutual inductance increases from 13.61 nH to 26.64 nH when the variable rotation angle ψ

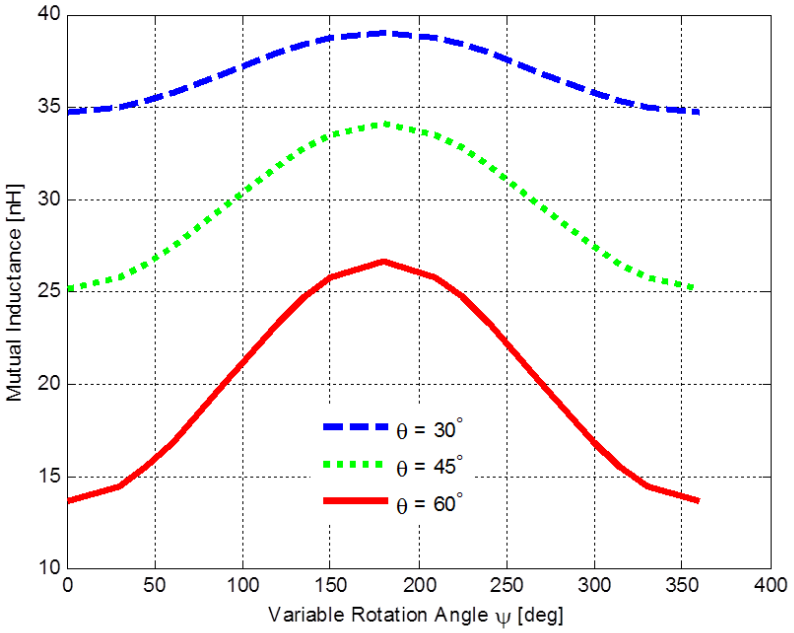

FIGURE 3.8: Mutual inductance between FC coils with arbitrary misalignment

TABLE 3.2: Example studied in (Akyel et al., 2009; Anele et al., 2015c)

Variable Rotation Angle ψ and $\theta = 60°$

ψ	(a, b, c) (Akyel et al., 2009)	M (nH) (Akyel et al., 2009)	M (nH) (Grover, 1944)	(a, b, c) (Anele et al., 2015c)	M (nH) (Anele et al., 2015c)
0	$(0; -0.086; 0.050)$	13.61	13.61	$(0; -0.866; 0.500)$	13.61
$\pi/6$	$(0.043; -0.075; 0.050)$	14.47	14.47	$(0.433; -0.750; 0.500)$	14.47
$\pi/4$	$(0.075; -0.043; 0.050)$	15.49	15.49	$(0.612; -0.612; 0.500)$	15.49
$\pi/3$	$(0.061; -0.061; 0.050)$	16.82	16.82	$(0.750; -0.433; 0.500)$	16.82
$\pi/2$	$(0.086; 0; 0.050)$	20.05	20.05	$(0.866; 0; 0.500)$	20.05
$2\pi/3$	$(0.075; 0.043; 0.050)$	23.33	23.33	$(0.750; 0.433; 0.500)$	23.33
$3\pi/4$	$(0.061; 0.061; 0.050)$	24.70	24.70	$(0.612; 0.612; 0.500)$	24.70
$5\pi/6$	$(0.043; 0.075; 0.050)$	25.75	25.75	$(0.433; 0.750; 0.500)$	25.75
π	$(0; 0.086; 0.050)$	26.64	26.64	$(0; 0.866; 0.500)$	26.64
$7\pi/6$	$(-0.043; 0.075; 0.050)$	25.75	25.75	$(0.433; 0.750; 0.500)$	25.75
$5\pi/4$	$(-0.061; 0.061; 0.050)$	24.70	24.70	$(0.612; 0.612; 0.500)$	24.70
$4\pi/3$	$(-0.075; 0.043; 0.050)$	23.33	23.33	$(0.750; 0.433; 0.500)$	23.33
$3\pi/2$	$(-0.086; 0; 0.050)$	20.05	20.05	$(0.866; 0; 0.500)$	20.05
$5\pi/3$	$(-0.075; -0.043; 0.050)$	16.82	16.82	$(0.750; -0.433; 0.500)$	16.82
$7\pi/4$	$(-0.061; -0.061; 0.050)$	15.49	15.49	$(0.612; -0.612; 0.500)$	15.49
$11\pi/6$	$(-0.043; -0.075; 0.050)$	14.47	14.47	$(0.433; -0.750; 0.500)$	14.47
2π	$(0; -0.086; 0.050)$	13.61	13.61	$(0; -0.866; 0.500)$	13.61

ranges from 0 to π and decreases from 26.64 nH to 13.61 nH when ψ ranges from π to 2π. This outcome (see Table 3.2) is in agreement with the results obtained in (Grover, 1944; Akyel et al., 2009; Anele et al., 2015c).

However, it is vital to note that the authors of (Akyel et al., 2009) obtained very wrong values for the parameters which define the centre of the secondary coil (i.e., a,

b and c). With such outcome, it is never possible for the authors to obtain the correct mutual inductance values. Nonetheless, the correct values for a, b and c are obtained in this thesis and can be obtained by substituting the variable rotation angle ψ and angular misalignment θ (see Table 3.2) in the given common notations, which are $a = sin\psi sin\theta$, $b = -cos\psi sin\theta$ and $c = cos\theta$.

3.4 Conclusion

This chapter presents the rederived models for the computation of the mutual inductance between FC coils with and without lateral and angular misalignment. Also, the computation of the mutual inductance between FC coils arbitrarily positioned in space is presented. MATLAB software is used to obtain the graphical and numerical results presented, and the clarifications concerning the errors made are presented.

Generally, the results obtained show that as the values of the coil separation distance and misalignment (e.g. lateral and angular) increase, the value of the mutual inductance M between the coils decreases (see Figs. 3.4 - 3.7 and Tables 3.1 - 3.2).

Thus it is possible for a MCS model to have an increased mutual inductance value provided that the air-cored coils have a reduced diameter and an increased number of turns. Nonetheless, the model presented in this section deals with a non realistic MCS model of LIPT systems for EVs and E-bikes.

Chapter 4

MAGNETIC FIELDS COMPUTATION and VALIDATION

4.1 Introduction

In this chapter, section 4.2 presents the models for calculating the magnetic flux through the secondary coil, the mutual inductance between the FC coils and the induced voltage in the secondary side of the coil. Section 4.3 presents the formulated model for calculating the magnetic fields between two FC coils (Anele et al., 2015c). In addition, the computed results obtained for the magnetic fields are validated with experimental measurement. Lastly, section 4.4 concludes this chapter.

It is vital to note that the non-conducting magnetic material that covers the coils of the inductive charging system, which is employed for experimental measurement in the laboratory is not considered in the models formulated.

4.2 Models: Magnetic Flux, Mutual Inductance and Induced Voltage

The model for calculating the total magnetic flux through the secondary FC coil due to the current in the primary FC coil is formulated based on Fig. 4.1. where R_P and R_S are the radii of the primary and secondary FC coils respectively, I_P and I_S are their primary and secondary currents, d is the separation distance between them, ϕ_d is the angle between the positive x_S axis and the line segment pointing from its origin to the arbitrary point E_S and ϕ_0 is the angle between the positive x_P axis and the line segment pointing from its origin to the arbitrary point B_P.

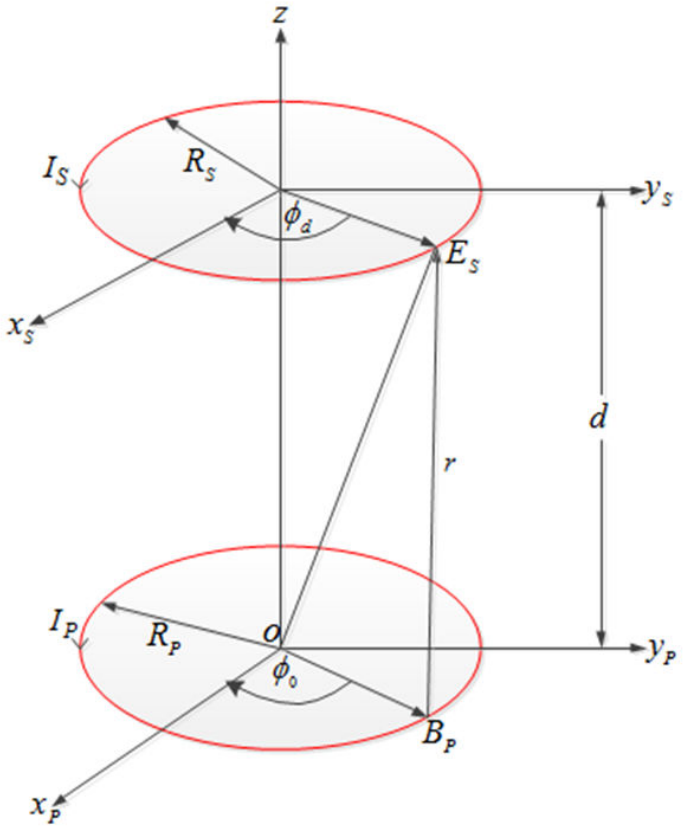

FIGURE 4.1: Coaxial filamentary circular coils

Thus in order to successfully achieve the formulation of the magnetic flux model, the following mathematical expressions are considered:

- The coil of radius R_P lies in the plane $x_P O y_P (z_P = 0)$ with its centre point at $O(0, 0, 0)$

- The parametric coordinates of the arbitrary point B_P on the primary coil are

$$x_P = R_P \cos\phi_0, \quad y_P = R_P \sin\phi_0, \quad z_P = 0 \tag{4.1}$$

  where $\phi_0 \, \epsilon \, [0, \, 2\pi]$

- The differential element located at equation (4.1) is given by

$$d\vec{l_P} = R_P(-\vec{i}\sin\phi_0 + \vec{j}\cos\phi_0)d\phi_0 \tag{4.2}$$

- The parametric coordinates of the arbitrary point E_S on the secondary coil are

$$x_S = -R_S \sin\phi_d, \quad y_S = R_S \cos\phi_d, \quad z_S = d \tag{4.3}$$

  where $\phi_d \, \epsilon \, [0, \, 2\pi]$

- The differential element located at equation (4.3) is given by

$$d\vec{l_S} = R_S(-\vec{i}\cos\phi_d - \vec{j}\sin\phi_d)d\phi_d \tag{4.4}$$

The magnetic vector potential A at point $E_S(x_S, y_S, z_S)$ produced by a circular current coil, I_P of radius R_P is given by

$$\vec{A} = \frac{\mu_0 \mu_r}{4\pi} \int_{l_P} \frac{I_P}{r} d\vec{l}_P \tag{4.5}$$

where μ_0 is the permeability of free space, μ_r is the relative permeability of air, I_P is the primary coil current and r, which is the distance between the arbitrary points B_P and E_S is given by

$$\begin{aligned} r &= |E_S - B_P| = \sqrt{(x_S - x_P)^2 + (y_S - y_P)^2 + (z_S - z_P)^2} \\ r &= \sqrt{R_S^2 + R_P^2 + d^2 + 2R_S R_P(\sin\phi_d \cos\phi_0 - \cos\phi_d \sin\phi_0)} \end{aligned} \tag{4.6}$$

According to Stokes' theorem, the magnetic flux through the secondary coil as a result of the current, I_P in the primary coil is given by

$$\begin{aligned} \Phi &= \int\int_{S_s} \vec{B} \cdot d\vec{S}_s = \int\int_{S_s} (\nabla \times \vec{A}) d\vec{S}_s \\ \Phi &= \int_{l_s} \vec{A} d\vec{l}_s \end{aligned} \tag{4.7}$$

S_s and l_s are respectively the cross-section and the perimeter of the secondary coil. Thus substituting equations (4.2), (4.4) and (4.5) into equation (4.7) result to the formulated model for calculating the total magnetic flux through the secondary coil

$$\Phi_T = \frac{\mu_0 \mu_r N_P N_S I_P R_P R_S}{4\pi} \int_0^{2\pi} \int_0^{2\pi} \frac{\sin\phi_0 \cos\phi_d - \cos\phi_0 \sin\phi_d}{r} d\phi_d d\phi_0 \tag{4.8}$$

where r is given in equation (4.6) whereas N_P and N_S are the number of turns for the primary and secondary FC coils.

Furthermore, the computation of the mutual inductance between the two FC coils is an important parameter for obtaining the voltage induced in the secondary side of the coil and by definition, it is given by

$$\begin{aligned} M &= \frac{\Phi_T}{I_P} \\ M &= \frac{\mu_0 \mu_r N_P N_S R_P R_S}{4\pi} \int_0^{2\pi} \int_0^{2\pi} \frac{\sin\phi_0 \cos\phi_d - \cos\phi_0 \sin\phi_d}{r} d\phi_d d\phi_0 \end{aligned} \tag{4.9}$$

According to Faraday's law, the induced voltage in the secondary FC coil is equal to the rate of change of the total magnetic flux Φ_T and is given by

$$V = M\omega I_{P_{pk}} \cos(\omega t) \tag{4.10}$$

where $I_{P_{p_k}}$ is the primary coil peak current

4.2.1 Presentation and Discussion of Results

The variations of the total magnetic flux Φ_T, mutual inductance M and induced voltage V versus the separation distance d between the two FC coils are shown in Figs. 4.2 and 4.3. These results are obtained by using double quadrature function in MATLAB to compute the models given in equations (4.8), (4.9) and (4.10).

Based on equation (4.6), the value of the distance r between the arbitrary points B_P and E_S is dependent on the radii of the coils (i.e., R_P and R_S) and the distance d between the centres of the coils. Thus for higher values of R_P, R_S and d, r increases. Figures 4.2 and 4.3 show that the values of Φ_T, M and V decrease as d increases.

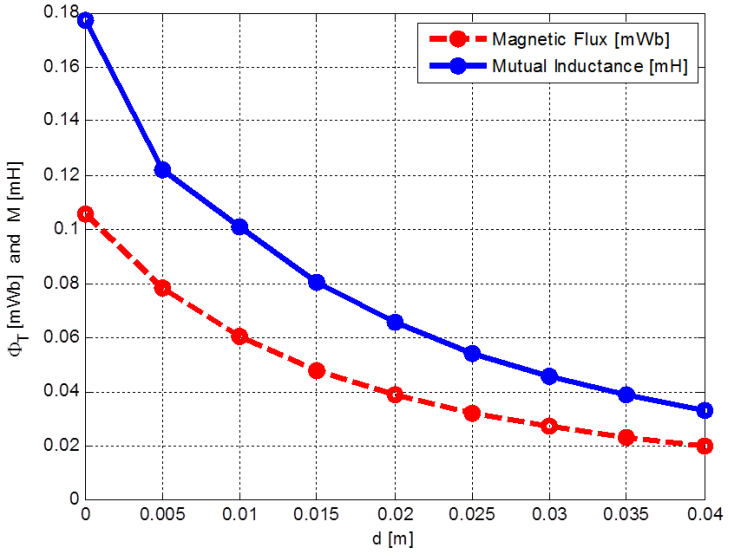

FIGURE 4.2: Mutual inductance and total magnetic flux versus separation distance

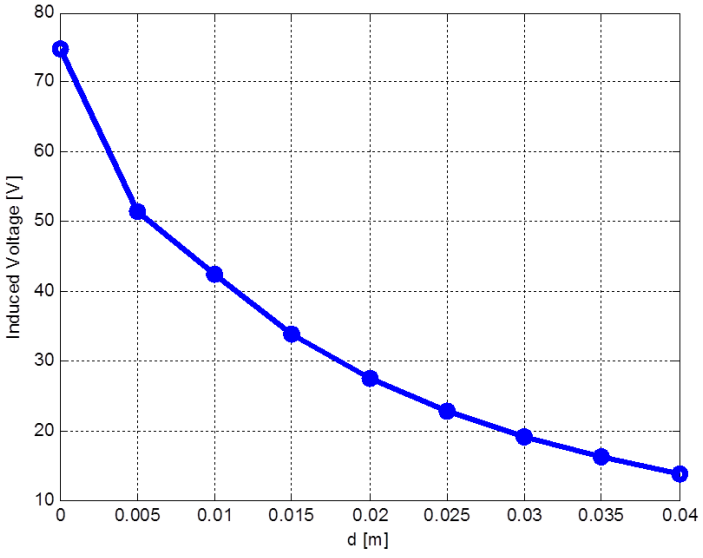

FIGURE 4.3: Induced voltage versus coil separation distance

These results are obtained based on the parameters ($N_P = N_S = 30$, $V_{rms} = 220\ V$, $I_P = 0.55\ A_{rms}$, $R_P = R_S = 0.052\ m$, $\mu_r = 1$, $\mu_0 = 4\pi \times 10^{-7}\ \frac{H}{m}$) of the inductive charging system that is employed for experimental measurement in the laboratory. In addition, it is found out from the oscilloscope that the transfer of power from the primary to the secondary side of the inductive charger is achieved at a high electromagnetic frequency of 80 kHz.

The inductive charger employed for experimental measurement is made up of primary and secondary FC coils. With the use of Multimeter, a maximum voltage of 75 V is measured from the terminal of the plug-in connector and it is obtained when the coil separation distance between the two FC coils is equal to zero. Also, at $d = 0$, a computed induced voltage of 74.70 V_{max} (see Fig. 4.3) is obtained and such outcome is in agreement with the measured value. Thus in order to obtain the induced current I_S in the secondary side of the FC coil, the inductive charger is used to power 60 W_{max} LED lamp and by measurement, a peak I_S of 0.8 A is obtained.

4.3 Model for Magnetic Fields Computation

The model for calculating the magnetic fields between two FC coils with arbitrary misalignment is formulated based on equation (2.3) (Babic & Akyel, 2012). Thus for two coils, the total magnetic fields is the sum of the magnetic fields from each of the

coils, and according to (Anele et al., 2015c), it is formulated as

$$\begin{aligned} B_x &= [-\frac{\mu_0\mu_r I_P N_P (z+\frac{d}{2})xk}{8\pi\sqrt{R_P}(x^2+y^2)^{5/4}}L_0] + [-\frac{\mu_0\mu_r I_S N_S (z-\frac{d}{2})xk}{8\pi\sqrt{R_S}(x^2+y^2)^{5/4}}L_0] \\ B_y &= [-\frac{\mu_0\mu_r I_P N_P (z+\frac{d}{2})yk}{8\pi\sqrt{R_P}(x^2+y^2)^{5/4}}L_0] + [-\frac{\mu_0\mu_r I_S N_S (z-\frac{d}{2})yk}{8\pi\sqrt{R_S}(x^2+y^2)^{5/4}}L_0] \\ B_z &= [\frac{\mu_0\mu_r I_P N_P k}{8\pi\sqrt{R_P}(x^2+y^2)^{3/4}}S_0] + [\frac{\mu_0\mu_r I_S N_S k}{8\pi\sqrt{R_S}(x^2+y^2)^{3/4}}S_0] \end{aligned} \tag{4.11}$$

where $L_0 = 2K(k) - \frac{2-k^2}{1-k^2}E(k)$, $S_0 = 2\sqrt{x^2+y^2}K(k) - \frac{2\sqrt{x^2+y^2}-(R+\sqrt{x^2+y^2})k^2}{1-k^2}E(k)$, $k^2 = \frac{4R\sqrt{x^2+y^2}}{(R+\sqrt{x^2+y^2})^2+z^2}$. Also, the two coils are separated by a distance d which is equal to the radii of the coils.

Furthermore, according to (Akyel et al., 2009), the following mathematical expressions must be considered for FC coils without lateral and angular misalignment:

- The parameters (a, b and c) which determine the positioning of the secondary coil plane are defined as $a = 0$, $b = 0$ and $c = 1$.
- The centre of the secondary coil at point C becomes $(x_C = 0, y_C = 0, z_C = h)$. In this thesis, h is the distance measured from the centre point between the two FC coils to any point along the symmetry axis of the coils.

Lastly, taking into account that the radii of the coils are equal (i.e., $R_P = R_S$), and applying the above information to the parameters (x_S, y_S, z_S) of equation (2.3), $x = -R\sin\phi$, $y = -R\cos\phi$, $z = h$.

4.3.1 Presentation and Discussion of Results

Figures 4.4 and 4.5 respectively show the magnetic field lines due to a FC coil and between two FC coils without misalignment. These results are obtained by calculating equations (2.3) and (4.11) in MATLAB using Quadrature function. The graphical representation of these field lines is very useful in visualizing the magnitude (or strength) and direction of the magnetic fields. The straight line on the plots (see Figs. 4.4 and 4.5) is simply drawn to show the physical presence of the coil.

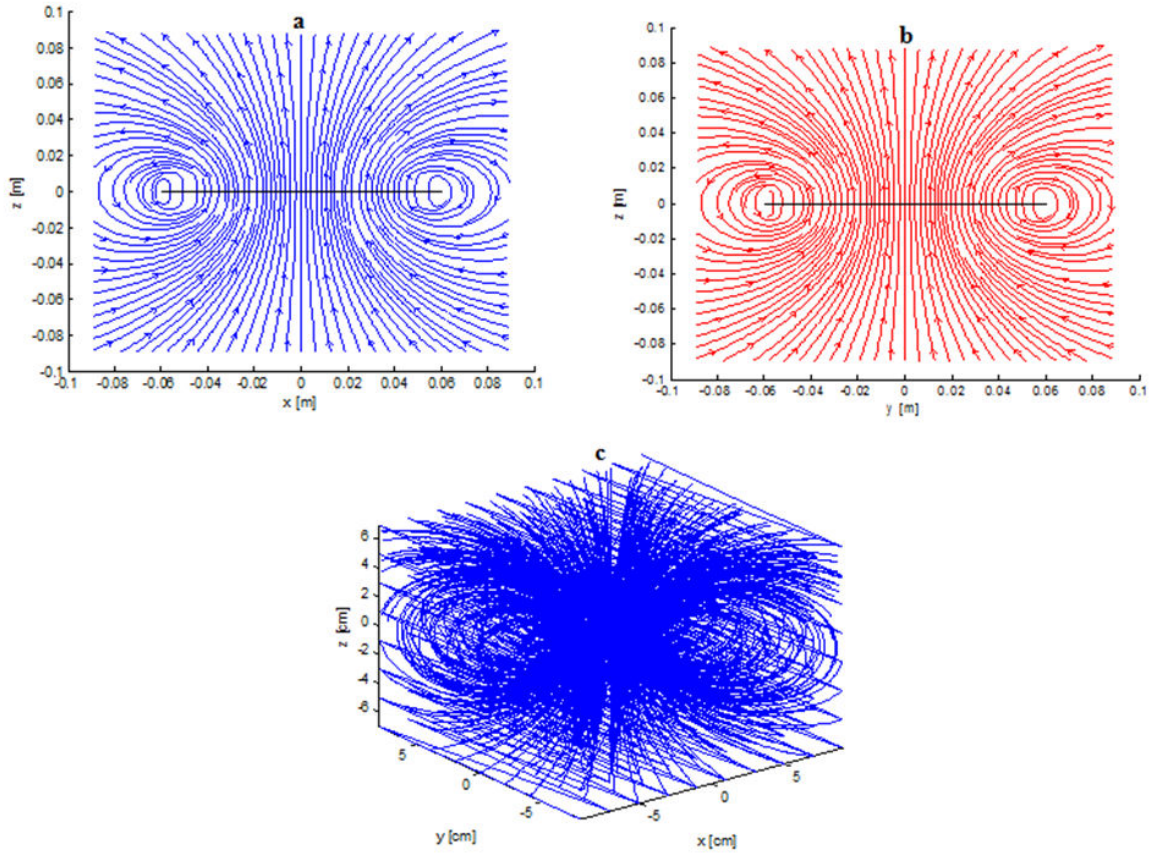

FIGURE 4.4: Magnetic field lines due to a FC coil
(a) XZ (b) YZ and (c) XYZ planes.

The results obtained show that the magnetic fields lines in 2-D (i.e., XZ and YZ) planes are symmetrical (see Figs. 4.4a and 4.4b). In addition, the 3-D (i.e., XYZ

planes) magnetic field lines are continuous, forming closed loops without beginning or end (see Fig. 4.4). The well spaced streamlines with direction arrows are obtained by using streamslice function in MATLAB. Figures 4.5 (a) and (b) show when the currents I_P and I_S of the FC coils flow in the same direction and opposite direction respectively whereas Fig. 4.5 (c) is obtained when the distance between the coils is increased.

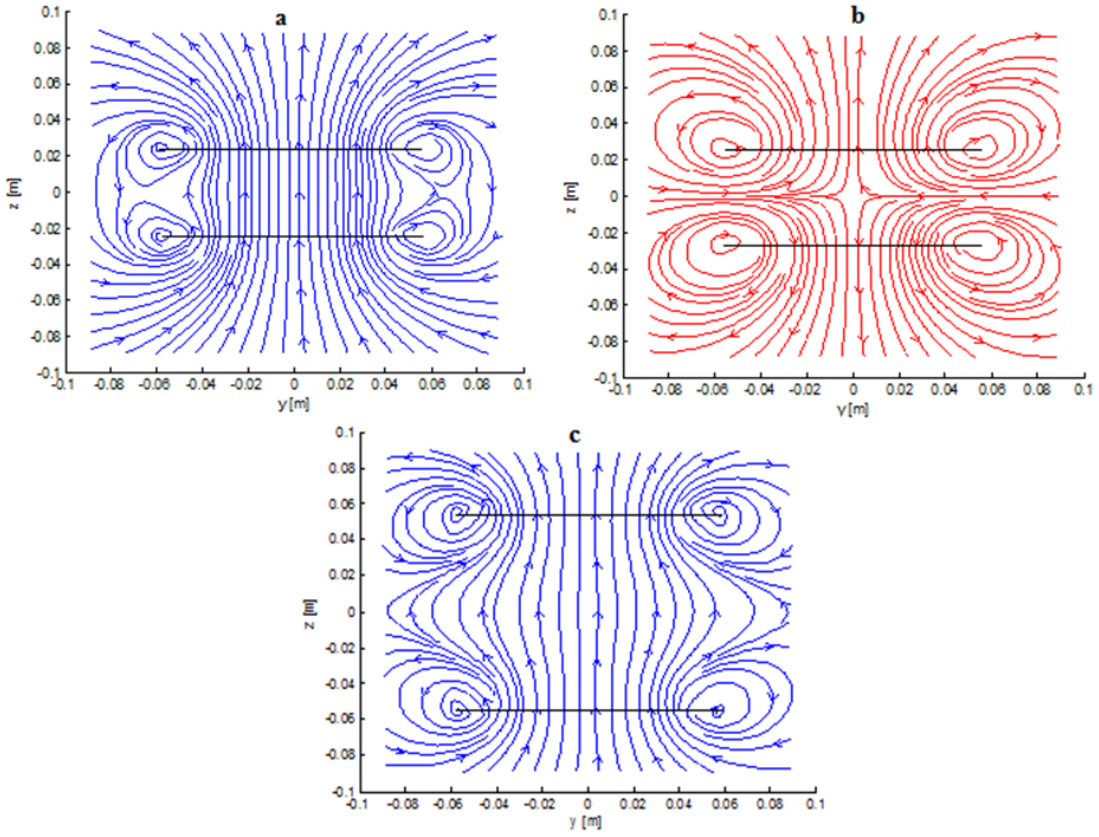

FIGURE 4.5: Magnetic field lines between two FC coils
Currents I_P and I_S flowing in the (a) same direction and (b) opposite direction and (c) when d between the coils is increased.

The results obtained for the computation and experimental validation of the magnetic fields between two FC coils are shown in Figs. 4.6 - 4.7. The magnetic fields

distribution B_x, B_y and B_z at $d = 0.052\ m$, $d = 0.03\ m$ and $d = 0.01\ m$ respectively are shown in Figs. 4.6a, 4.6c and 4.7a. The validation of the computed results (see Figs. 4.6b, 4.6d and 4.7b) are achieved based on the model formulated in equation (4.11) and the magnetic fields experimental measurements implemented in the laboratory (see Fig. 4.7c). In this thesis, experimental measurement is conducted only for B_z because B_x and B_y are symmetrical. Also, it is vital to note that the non-conducting magnetic material that covers the coils used for experimental measurement is not considered in the model formulated in equation (4.11).

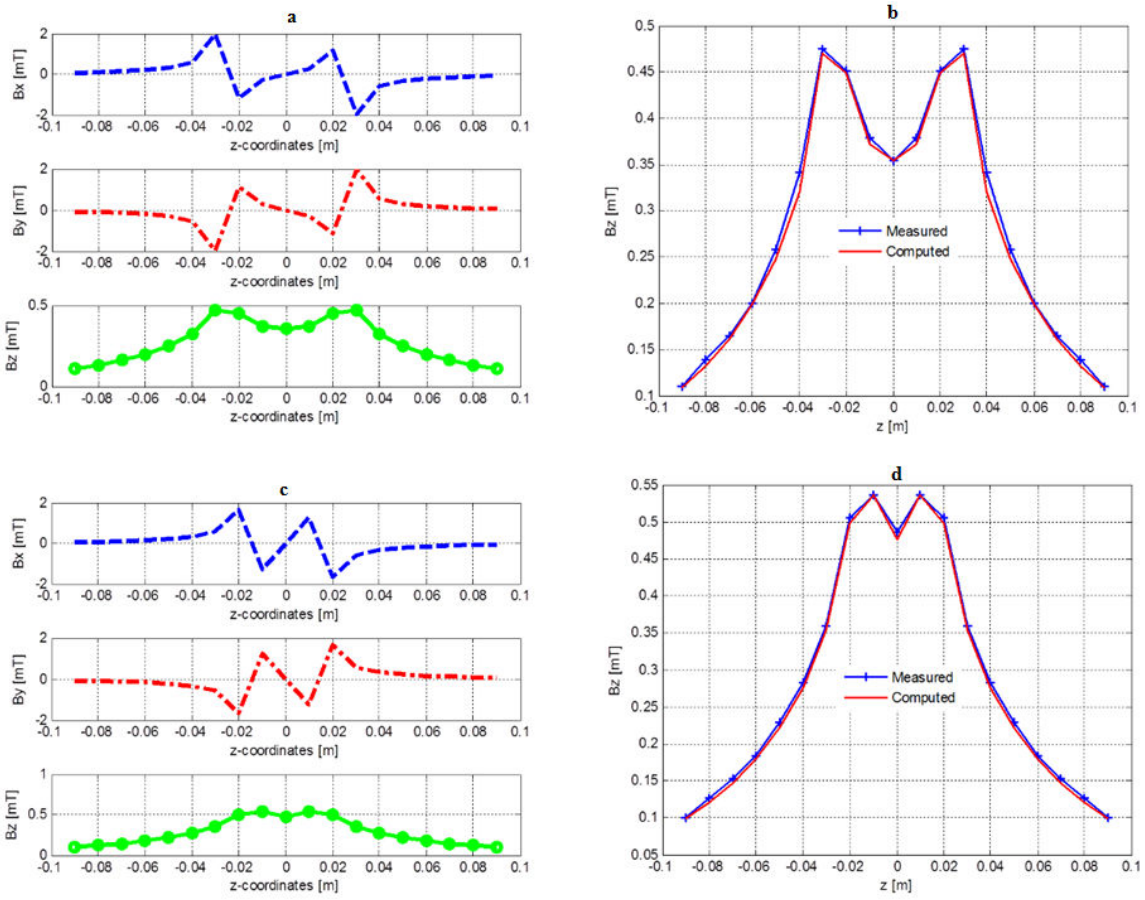

FIGURE 4.6: Magnetic fields computation and validation
(a) B_x, B_y and B_z at $d = 0.052\ m$, (b) experimental validation of B_z at $d = 0.052\ m$, (c) B_x, B_y and B_z at $d = 0.03\ m$ and (d) experimental validation of B_z at $d = 0.03\ m$

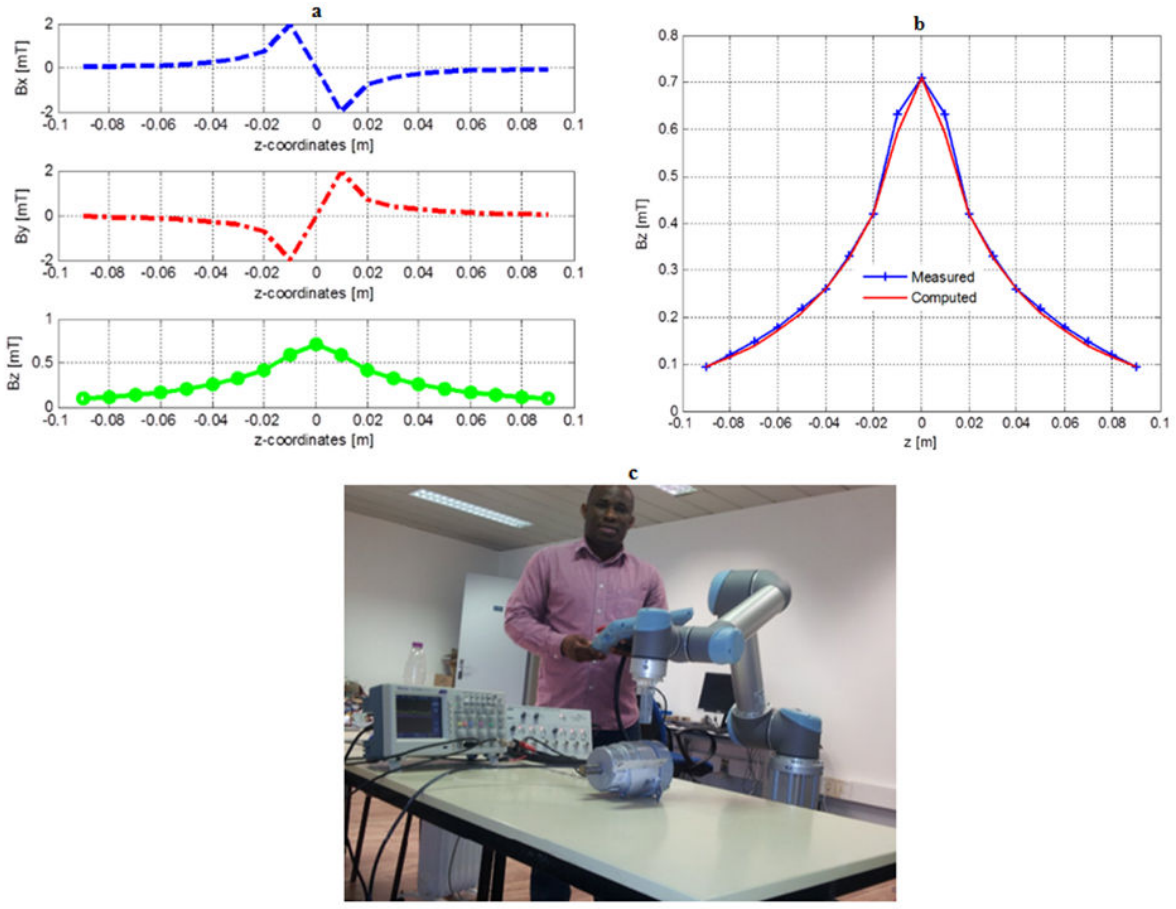

FIGURE 4.7: Magnetic fields computation and validation
(a) B_x, B_y and B_z at $d = 0.01\ m$, (b) experimental validation of B_z at $d = 0.01\ m$ and (c) experimental setup for magnetic fields measurement.

Universal robots (UR5) in connection with sensor, magnetometer and oscilloscope are used to obtain the magnetic fields results between the FC coils of the inductive charger employed for experimental measurements (see Fig. 4.7c). UR5 is a machine that can be programmed to move a tool, and communicate with other machines using electrical signals. With the aid of Polyscope that is, the graphical user interface (GUI), it is easy to program the robot to move the sensor along a desired trajectory.

In the GUI, the motions of the sensor are given using a series of way points and a way point can be given by moving the robot to a certain position. So, the robot

performs a task by moving through a sequence of way points. Figure 4.7c shows the UR5 holding the sensor of the magnetometer which is connected to the oscilloscope. By switching the control knob of the magnetometer to XY axis section, it is possible to measure the magnetic fields B_x and B_y. This is achievable because one of the technical characteristics of the sensor is that it can implement a bi-axial directional measurement (i.e., in the X and Y directions). Also, measurement for the B_z can be obtained by switching the control knob to the Z-axis section of the magnetometer.

Thus, with this experimental set up, the robot is programmed to move the sensor from the centre point (i.e, $z = h = 0$) between the two FC coils to a particular point (i.e., $z = h = 0.09\ m$), which is along the symmetric axis of the coils.

4.4 Conclusion

In order to validate the measured values of the magnetic fields which are obtained from the inductive charger employed in the Laboratory, the model for calculating the magnetic fields between the two FC coils of the inductive charger is formulated.

In comparison to chapter 3, MATLAB computation for the voltage and current induced in the secondary side of the FC coil is achieved by deriving the models for computing the total magnetic flux and the mutual inductance between the two coils. With the help of the formulated models, it is observed that the values of the magnetic fields as well as Φ_T, M and V can be increased provided a higher frequency AC

voltage is supplied to the primary coil, the number of turns of the coils are increased and the diameter of the coils are reduced.

The comparison of the results show that the model formulated and experimental measurements implemented in the laboratory are accurate. Nonetheless, it is important to note that the non-conducting magnetic material which covers the coils of the inductive charger is not considered in the formulated model. Thus there is a need to obtain a more complex and realistic MCS model.

Chapter 5

IPT MODELS FOR EV BATTERY CHARGE

5.1 Introduction

In this chapter, section 5.2 presents the analysis of the IPT transformers and the effects of capacitive compensation. Also, section 5.3 presents the computational IPT models of 3 kW single phase and 22 kW three phase systems for EV battery charge and lastly, section 5.4 concludes this chapter. In this chapter, no experimental results are implemented to validate the computed results, but the results are achieved based on the technical specification of Renault ZOE.

5.2 IPT Transformer and Effects of Compensation

The most significant part of IPT systems for EVs is its air-cored transformer. Its aim is to provide maximum electric power to the on-board battery storage system of EVs. However, it is faced with the problem of weak coupling (i.e., suffers from poor efficiency) due to the relatively large leakage reactance associated with its primary and secondary coils (Neves et al., 2011; Koo et al., 2012; Musavi & Eberle, 2014; Anele et al., 2015b). In this section, the behaviour of IPT transformer and the effects of capacitive compensation are studied based on Figs. 5.1 and 5.2.

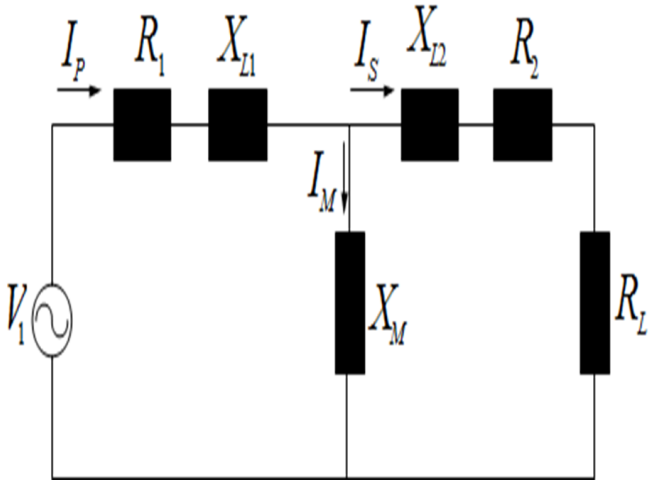

FIGURE 5.1: Equivalent circuit of a single-phase IPT transformer

I_P, I_M and I_S are the primary, mutual and secondary currents respectively, R_1, R_2 and R_L are the primary, secondary and load resistances respectively, X_{L1} and X_{L2} are the series leakage reactances, X_{C1} and X_{C2} are the capacitive reactances and V_1 is the root mean square (RMS) AC voltage. In addition, X_M is the mutual inductance between the coils. It is given by $2\pi fM$, where $M{=}k\sqrt{L_1L_2}$; k is the

coupling coefficient, f is the operating frequency whereas L_1 and L_2 are the series leakage inductances.

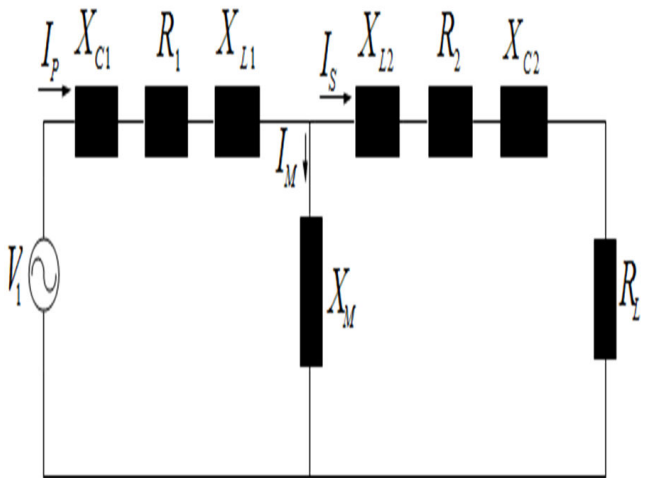

FIGURE 5.2: Compensated equivalent circuit of a single-phase IPT transformer

Based on Fig. 5.1, the equivalent impedance of the circuit as seen by the AC voltage source is given by

$$Z_{eq} = R_1 + X_{L1} + \frac{X_M R_2 + X_M R_L - X_M X_{L2}}{X_M + X_{L2} + R_2 + R_L} \tag{5.1}$$

By applying current divider rule, the current division ratio is given by

$$K_c = \frac{I_S}{I_P} = \frac{X_M}{R_2 + R_L + (X_{L2} + X_M)} \tag{5.2}$$

Also, based on Fig. 5.1, the power transfer efficiency is given by

$$\eta = \frac{R_L I_S^2}{R_L I_S^2 + R_2 I_S^2 + R_1 I_P^2} = \frac{R_L}{(R_L + R_2) + R_1(\frac{(R_2+R_L)+(X_{L2}+X_M)}{X_M})} \tag{5.3}$$

Amongst other capacitive compensation techniques proposed in (Wang et al., 2005; Barth et al., 2011; Schmuelling et al., 2012; Neves et al., 2011; Chopra & Bauer, 2011; García et al., 2015; Anele et al., 2015b), series-series (SS) technique is employed because it helps to improve the power transfer capability of the transmission line due to its partial compensation of the series leakage reactance.

Based on Fig. 5.2, the equivalent impedance of the circuit as seen by the voltage source is given by

$$Z_{eq} = X_{C1} + R_1 + X_{L1} + \frac{X_M(X_{L2} + R_2 + X_{C2} + R_L)}{X_{L2} + R_2 + X_{C2} + R_L + X_M} \tag{5.4}$$

For an exactly compensated transmission link of the IPT transformer, the following reactance conditions are vital (Schmuelling et al., 2012; Anele et al., 2015b):

$$\begin{aligned} X_{C1} + X_{L1} + X_M &= 0 \\ X_{C2} + X_{L2} + X_M &= 0 \end{aligned} \tag{5.5}$$

Thus substituting equations (5.5) into (5.4) gives the compensated equivalent impedance of the circuit as

$$Z_{eqc} = \frac{R_1R_2 + R_1R_L + X_M^2}{(R_2 + R_L)} \tag{5.6}$$

Based on Fig. 5.2, the compensated current division ratio is given by

$$K_{cc} = \frac{I_S}{I_P} = \frac{X_M}{R_2 + R_L} \tag{5.7}$$

Also, the compensated power transfer efficiency is given by

$$\eta_c = \frac{R_L I_S^2}{R_L I_S^2 + R_2 I_S^2 + R_1 I_P^2} = \frac{R_L}{(R_L + R_2) + R_1(\frac{R_2 + R_L}{X_M})} \tag{5.8}$$

5.2.1 Presentation and Discussion of Results

Figure 5.3 shows the variation of current division ratio without compensation, K_c (see Figs. 5.3 a and b) and compensated current division ratio, K_{cc} (see Figs. 5.3 c and d) as a function of frequency f for different values of mutual inductance M and resistive load R_L. Figure 5.3 is obtained by calculating the equations (5.2) and (5.7) in MATLAB M-File. In the case without compensation, the values of K_c increase as f increases, but at higher frequencies, they become constant in spite of the change in R_L. However, different values of K_c are obtained for different values of M. With capacitive compensation, the values of K_{cc} kept increasing as f increases, and different values of K_{cc} are obtained for different values of M and R_L. These results imply that SS capacitive compensation helps to improve the power transfer capability of the IPT transformer. Based on the IPT parameters used for MATLAB simulation (see Table 5.1), the results obtained show that the IPT system considered in (Chopra & Bauer, 2011; Anele et al., 2015b) must be operated above 100 kHz.

The power transfer efficiency of the IPT transformer with and without compensation is shown in Fig. 5.4, and it is obtained by calculating equations (5.3) and (5.8) in MATLAB. Without compensation, a maximum power transfer efficiency of 78.14% is obtained whereas with SS capacitive compensation, 93.18% is obtained indicating that the power transfer efficiency is increased by 15.04%.

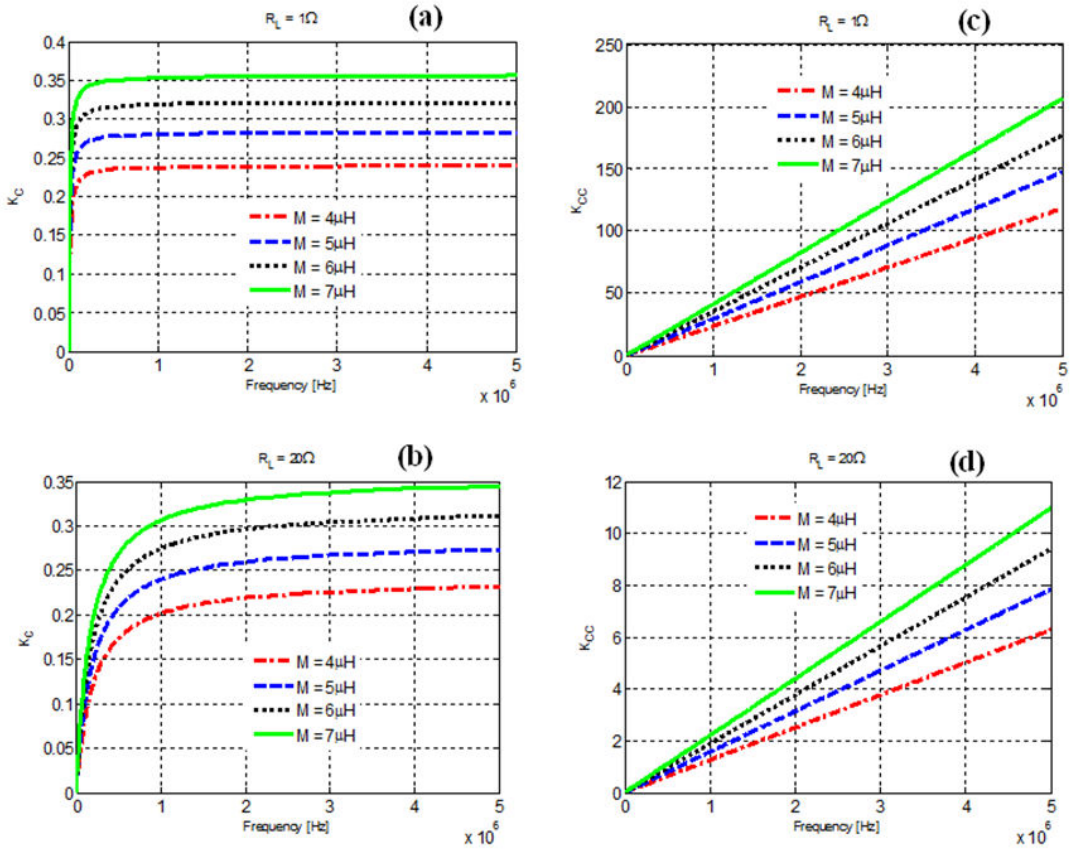

FIGURE 5.3: Variation of current division ratio with and without compensation Variation of K_c (see Figs. 5.3 a and b) and K_{cc} (see Figs. 5.3 c and d) as a function of frequency f for different mutual inductances M and resistive loads R_L.

TABLE 5.1: Parameters for IPT Transformer (Anele et al., 2015b)

Physical Parameters	Description	Values
L_1	Leakage inductance of primary coil	103.4 μH
L_2	Leakage inductance of secondary coil	12.67 μH
R_1	Resistance of primary coil	0.1530 Ω
R_2	Resistance of secondary coil	0.0660 Ω

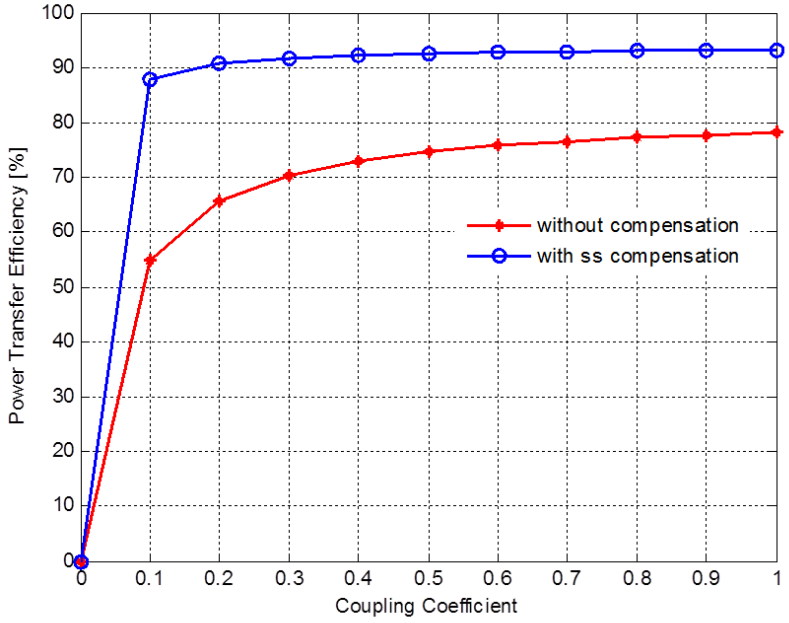

FIGURE 5.4: Power transfer efficiency vs coupling coeffiecient

5.3 IPT Models for EV Battery Charge

5.3.1 Simplified IPT Models for EVs

The simplified block diagrams of 3 kW single phase and 22 kW three phase IPT systems to be designed using MATLAB/Simulink are shown in Figs. 5.5 and 5.6. The power source, IPT transformer, compensation topology and battery charger are the major blocks of these IPT systems. The power source block of Fig. 5.5 comprises AC voltage of 220 V_{rms} at a frequency of 50 Hz, a single-phase uncontrolled bridge rectifier (UBR), an active power factor corrector (PFC) "boost converter" and a full-bridge inverter "insulated-gate bipolar transistor (IGBT)".

The single-phase UBR helps in transforming the AC voltage to a varying DC voltage.

It is employed because it is useful for supplying DC loads rarely exceeding 5 kW. An active PFC "boost converter" is a DC to DC power converter. It is used to produce a direct voltage of 400 V as input voltage for the primary full-bridge inverter. Also, a capacitor is added to the output of the boost converter to reduce voltage ripples, and this in turn produces a constant DC Voltage.

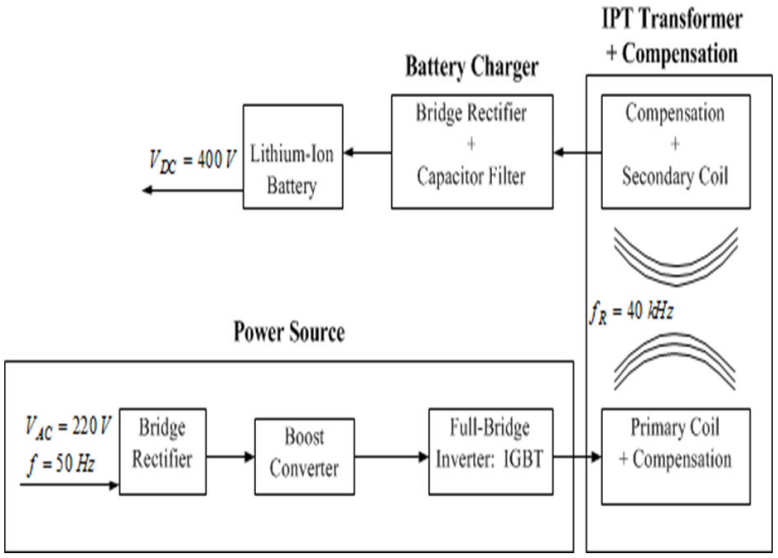

FIGURE 5.5: Simplified block diagram of a 3 kW single-phase IPT system (Anele et al., 2015b)

The power source block of Fig. 5.6 comprises AC voltage of 380 V_{rms} at a frequency of 50 Hz, a three-phase uncontrolled bridge rectifier (UBR), an active PFC "buck converter" and a full-bridge inverter "IGBT".

The three-phase UBR helps in transforming the AC voltage to a constant DC voltage. It is employed because it is the most extensively used rectifier topology from low ($>$ 5 kW) to moderately high power ($>$ 100 kW) applications. The buck converter is a voltage step down and current step up converter. In this chapter, it is used to step down the voltage produced from the three-phase UBR to a direct voltage of 400 V.

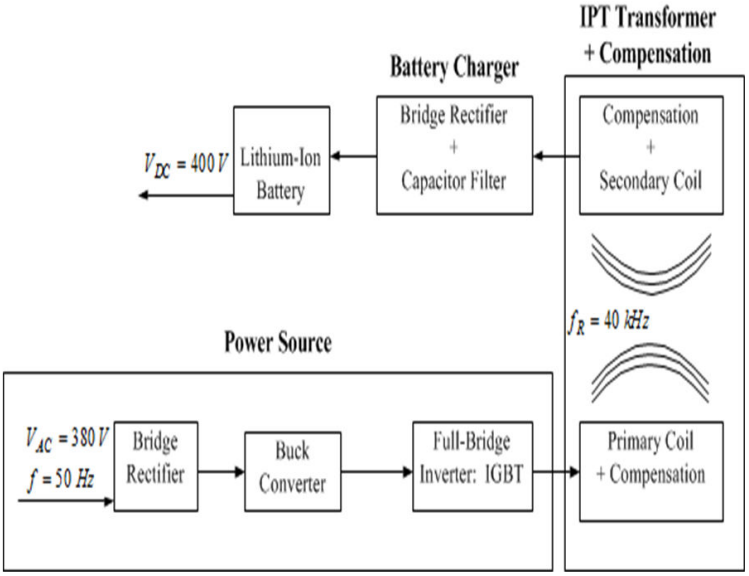

FIGURE 5.6: Simplified block diagram of a 22 kW three-phase IPT system (Anele et al., 2015b)

Furthermore, the IPT transformer block as shown in Figs. 5.5 and 5.6 is responsible for the transfer of electric power between the ground and the EV. The power coupling is established by the primary and secondary coils. The primary coil is galvanically connected to the full-bridge inverter "IGBT", which helps in converting the direct input voltage of 400 V into a higher and fixed frequency AC voltage. As a result, the primary coil generates a higher frequency electromagnetic field, which is then coupled with the secondary coil. The switching of this higher and fixed frequency is achieved with the help of a single-phase pulse width modulation (PWM) inverter circuit using IGBT. A maximum power transfer capability via the IPT transformer can be guaranteed when its reactive parts are compensated with capacitors, and this is established on the primary and secondary sides of the coils. The battery charger block is responsible for creating the connection between the IPT system and the lithium-ion battery to be charged. It consists of UBR and a capacitor filter. The

UBR is used to convert the high frequency AC voltage into a direct voltage and the capacitor is added to its output to reduce voltage ripples.

5.3.2 Presentation of Results for IPT Models

The computational models of 3 kW single phase and 22 kW three phase IPT systems designed using MATLAB/Simulink are shown in Figs. 5.7 and 5.8.

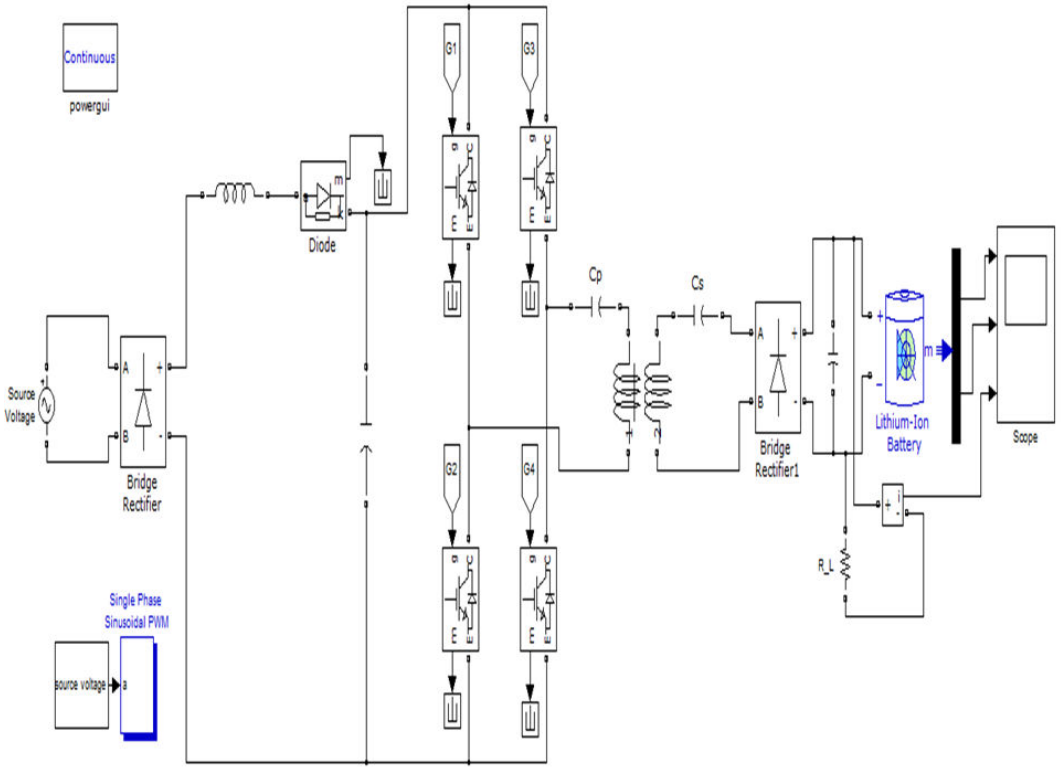

FIGURE 5.7: 3 kW single phase IPT model

The 3 kW computational IPT model is designed by using MATLAB/Simulink. The development of the model is based on the simplified block diagram shown in Fig. 5.5. It consists of (1) power source block: single-phase AC voltage source, single-phase uncontrolled bridge rectifier (UBR), boost converter and full-bridge inverter "IGBT" in connection with a single-phase pulse width modulation (PWM), (2) IPT transformer plus series series (SS) capacitive compensation, (3) battery charger: single-phase UBR plus capacitor filter and lastly, (4) lithium-ion battery. The parameter values are as follows: $C_P = 1.45 \times 10^{-2} F$, $C_S = 8.47 \times 10^{-2} F$, $M = 6.50 \times 10^{-4} H$ and $R_L = 7.27\Omega$

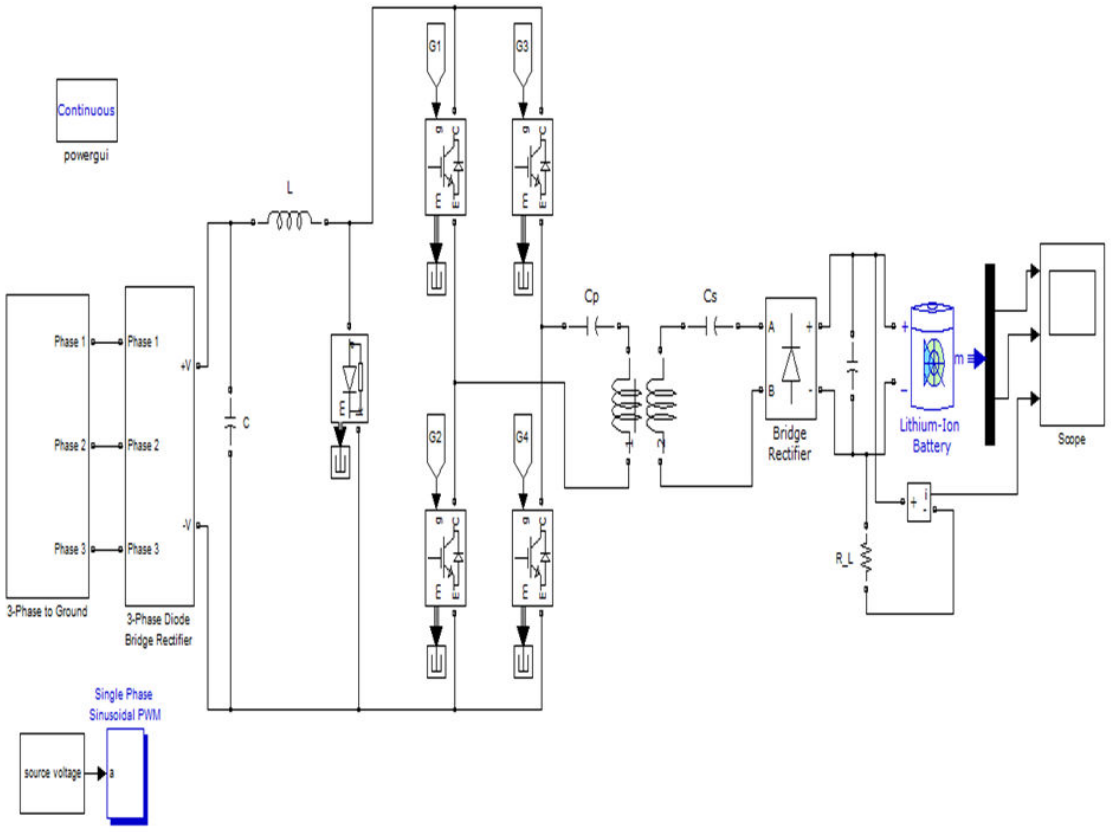

FIGURE 5.8: 22 kW three phase IPT model

The 22 kW computational IPT model is designed by using MATLAB/Simulink. The model is developed based on the simplified block diagram shown in Fig. 5.5. It consists of (1) power source block: three-phase AC voltage source, three-phase UBR, buck converter and IGBT in connection with a single-phase PWM, (2) IPT transformer plus SS capacitive compensation, (3) battery charger: single-phase UBR plus capacitor filter and lastly, (4) lithium-ion battery The parameter values are as follows: $C_P = 1.45 \times 10^{-2}F$, $C_S = 8.47 \times 10^{-2}F$, $M = 6.50 \times 10^{-4}H$ and $R_L = 53.3\Omega$

Detailed explanations concerning the modelled IPT systems have been presented in subsection 5.3.1. Nonetheless, the waveforms of 3 kW single phase AC source voltage, its full wave varying DC voltage and stepped up DC voltage are shown in Fig. 5.9. Also, the waveforms for 22 kW three phase AC source voltage, its full wave constant DC voltage and stepped down DC voltage are shown in Fig. 5.10.

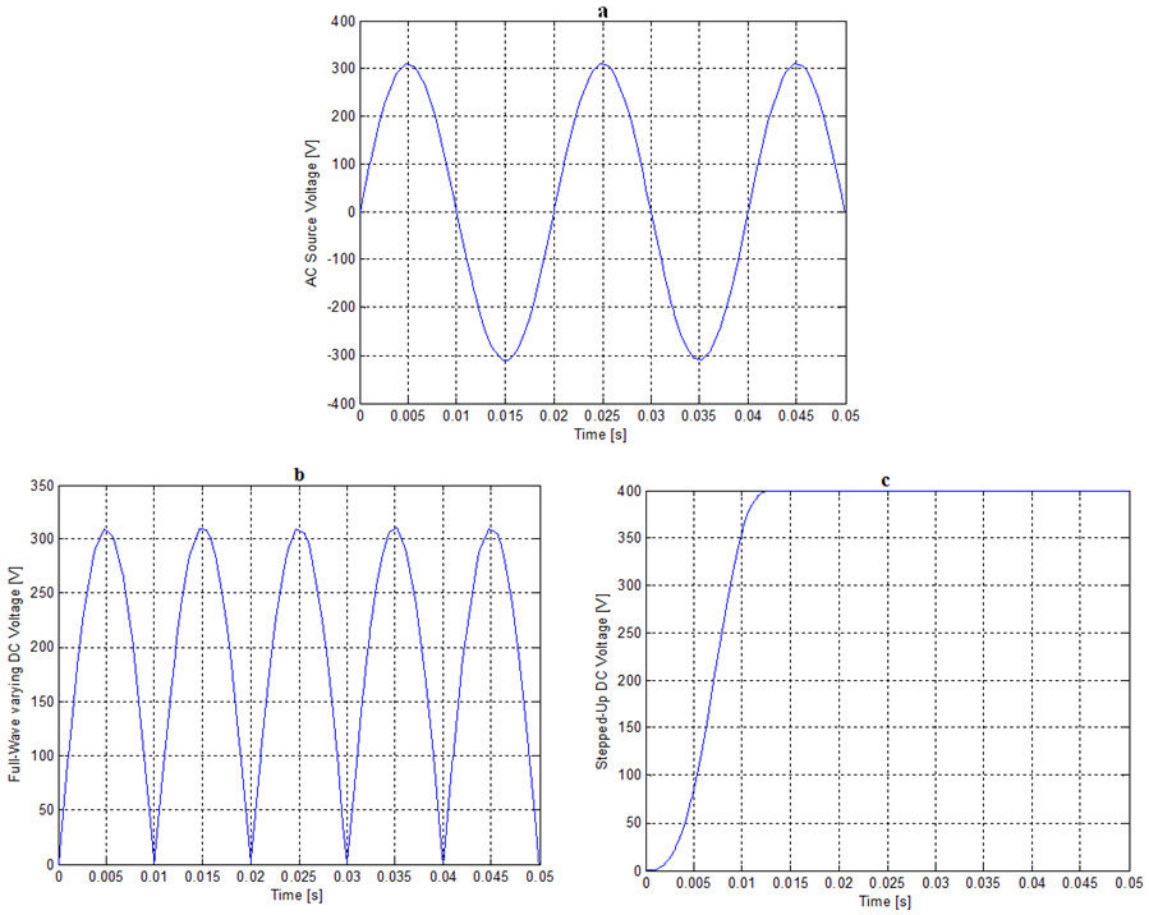

FIGURE 5.9: 3 kW single phase: AC and DC voltages
3 kW single phase (a) AC source voltage of 220 V_{RMS}, (b) full-wave varying DC voltage, which is obtained by using a single-phase uncontrolled bridge rectifier and (c) stepped up DC voltage, which is obtained using a boost converter.

Figure 5.11 shows the higher and fixed frequency AC voltage of 400 V at 40 kHz supplied to the primary coil of the IPT transformer. The full-bridge "IGBT" helps in converting the direct input voltage of 400 V into a higher and fixed frequency AC voltage. As a result, the primary coil is able to generate a higher frequency electromagnetic field which is then coupled with the secondary coil. The switching of this higher and fixed frequency is achieved with the help of single-phase PWM inverter circuit using IGBT.

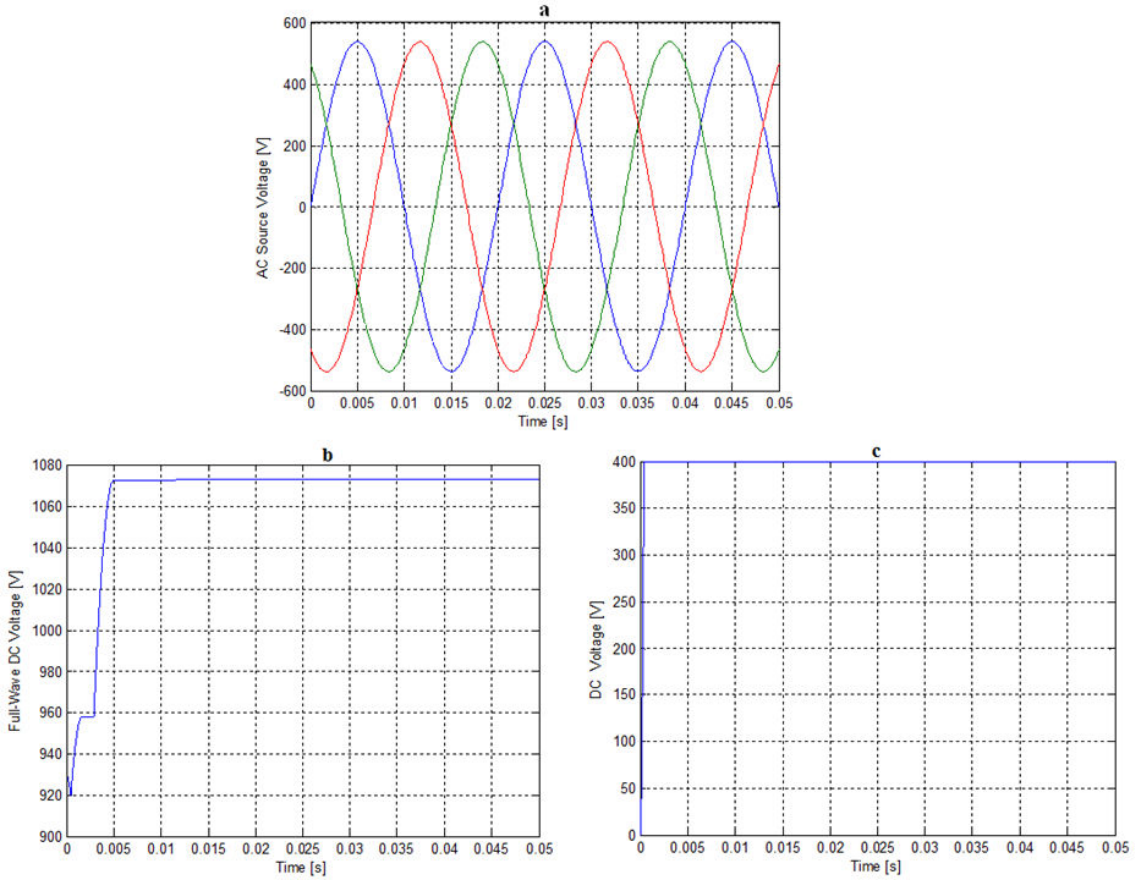

FIGURE 5.10: 22 kW three phase: AC and DC voltages
22 kW three phase (a) AC source voltage of 380 V_{RMS}, (b) full-wave constant DC voltage, which is obtained by using a three-phase uncontrolled bridge rectifier and (c) stepped down DC voltage, which is obtained using a buck converter.

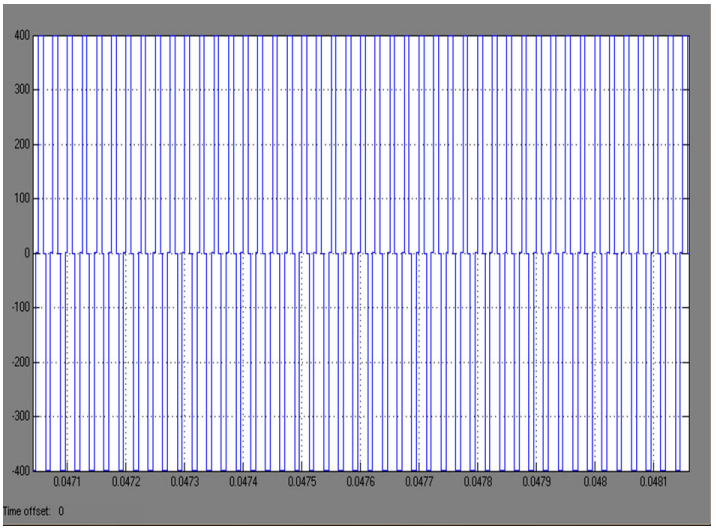

FIGURE 5.11: Higher and fixed AC voltage: primary coil
400 V at 40 kHz supplied to the primary coil of the IPT transformer

The results obtained for the load voltage, load current and state of battery charge for the 3 kW and 22 kW computational IPT models are shown in Figs. 5.12 and 5.13 respectively. These results are achieved based on the technical specifications of the lithium-ion battery and charger type of Renault ZOE (Chameleon charger type: 3 kW single-phased, 7.5 A for 6 to 9 hours charge time and 22 kW three-phased, 55 A and 80 % of the battery in 1 hour) as presented in (Anele et al., 2015b). Considering the charging time for each IPT model (see Figs. 5.14 and 5.15), the results obtained show that they are capable of delivering the electricity needed to power the battery of the Renault ZOE.

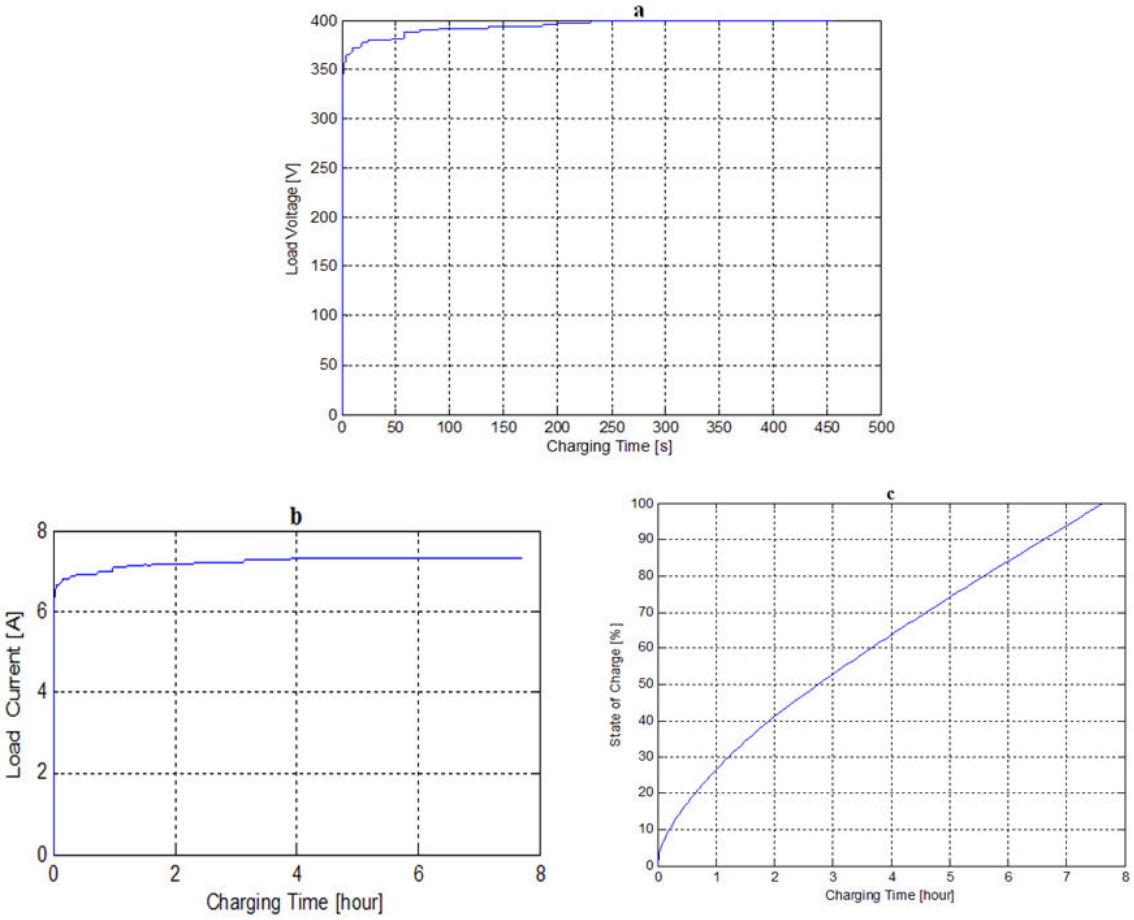

FIGURE 5.12: Results for 3 kW IPT model
Results obtained for 3 kW IPT model supplying a resistive load, R_L: (a) load voltage, (b) load current and (c) state of battery charge (Anele et al., 2015b)

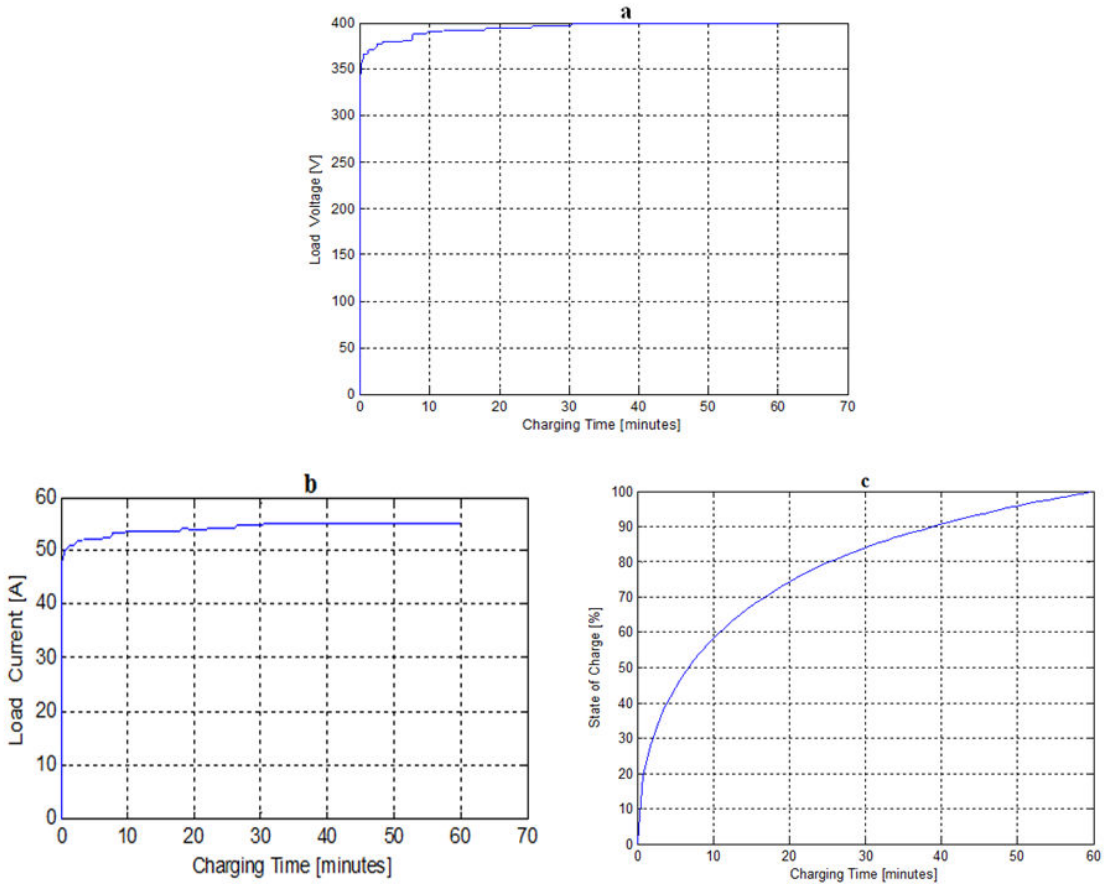

FIGURE 5.13: Results for 22 kW IPT model
Results obtained for 22 kW IPT model supplying a resistive load, R_L: (a) load voltage, (b) load current and (c) state of battery charge (Anele et al., 2015b)

Figures 5.14 and 5.15 show the results obtained for the discharge characteristics of the lithium-ion battery for 3 kW and 22 kW computational IPT models respectively. These plots which are obtained based on the IPT models given in Figs. 5.7 and 5.8 are composed of three sections: (1) discharge curve: represents the total discharge of the battery, when the voltage drops rapidly, (2) nominal area: represents the charge that can be extracted from the battery until the voltage drops below the battery nominal voltage and (3) exponential area: represents the exponential voltage drop when the battery is charged. Figure 5.16 shows the clarification on how the charging and discharging curves are obtained.

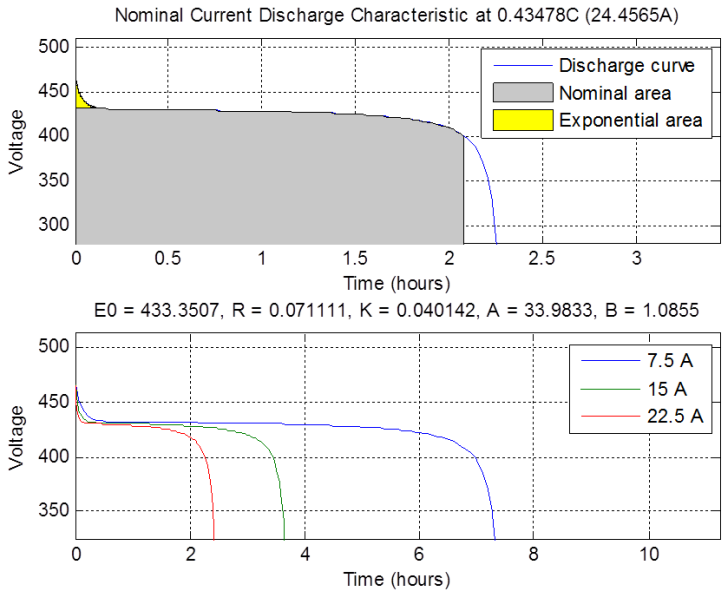

FIGURE 5.14: 3 kW IPT model: discharge characteristics of lithium-ion battery (Anele et al., 2015b)

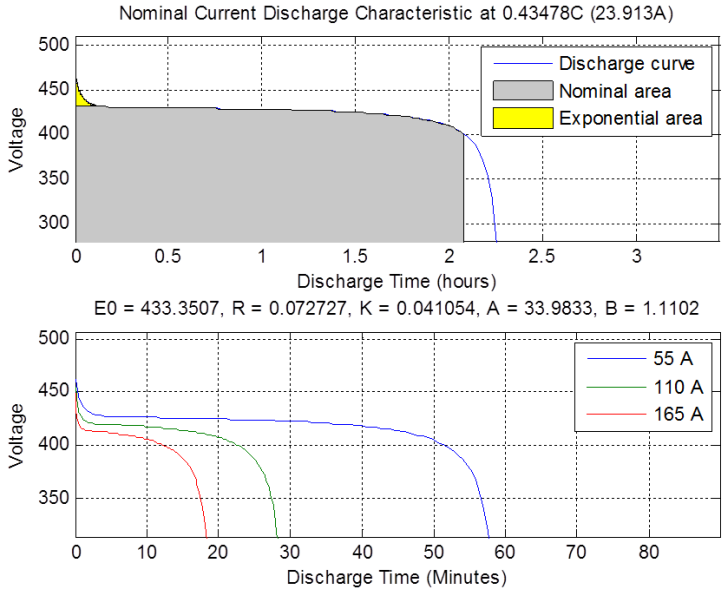

FIGURE 5.15: 22 kW IPT model: discharge characteristics of lithium-ion battery (Anele et al., 2015b)

Also, the results obtained show that the higher the load current demanded by the battery the quicker will be its discharge time. where E_0 is the constant voltage (V),

K is the polarization constant $(Ah)^{-1}$, A is the exponential voltage (V) and B is the exponential capacity $(Ah)^{-1}$.

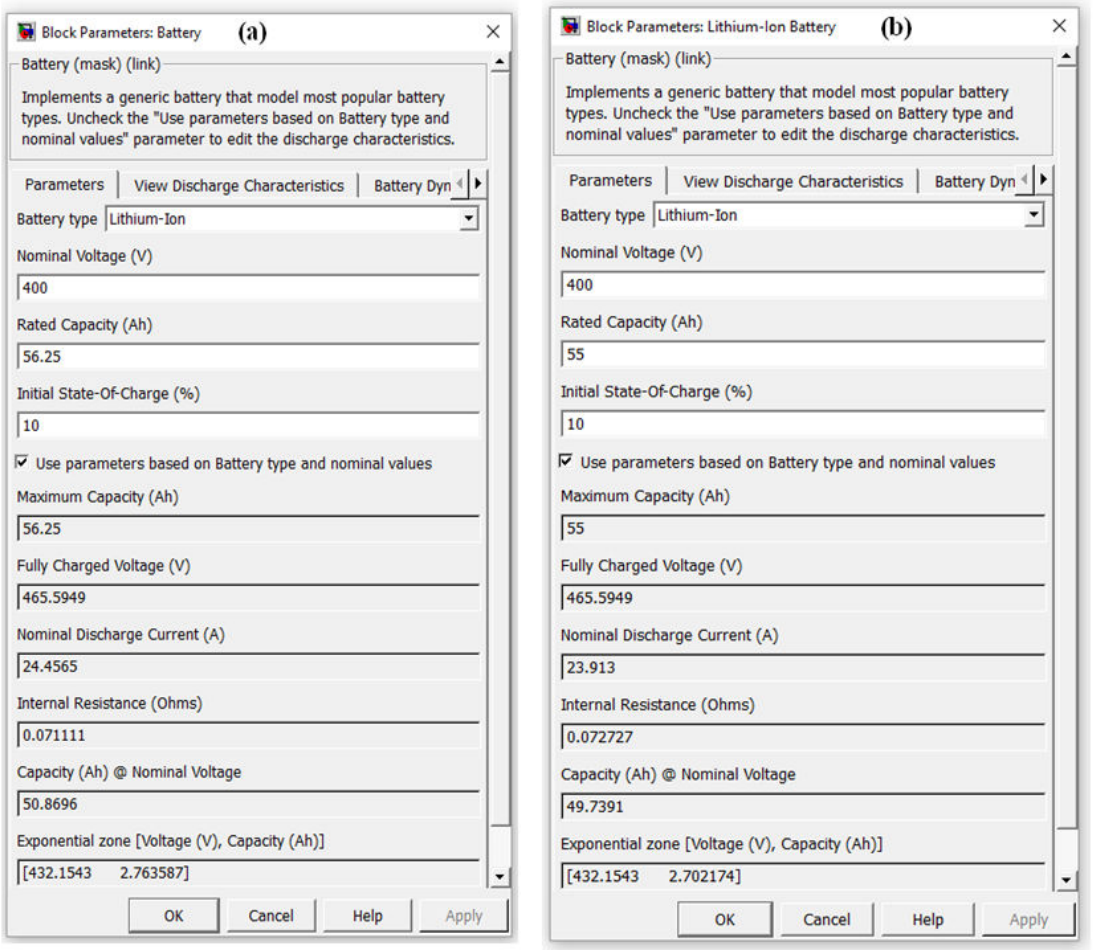

FIGURE 5.16: Block Parameters: Lithium-ion Battery
Lithium-ion battery for (a) 3 kW IPT model and (b) 22 kW IPT model

5.4 Conclusion

The main objective of the MCS model for LIPT systems is to help transfer maximum power to the on-board battery storage system of EVs. Unlike in chapters 3 and 4, series-series capacitive compensation is applied to the two sides of the air-cored coils; the results obtained show that with SS capacitive compensation, the power transfer

efficiency between the air-cored coils increased by 15.04% due to the partial compensation of the large leakage reactance associated with its primary and secondary coils, and based on that concept, computational models of a 3 kW single-phase and 22 kW three-phase IPT systems for EVs are designed using MATLAB/Simulink.

Nonetheless, since the objective of this thesis is to design a suitable and an effective MCS model of LIPT systems for EVs and E-bikes, it is seen that chapters 3 to 5 deal with a non-realistic MCS model for LIPT systems. This is because the models studied in these chapters do not incorporate air-cored coils with magnetic cores.

Chapter 6

DESIGN AND IMPROVEMENT OF MCS MODELS FOR LIPT SYSTEMS

6.1 Introduction

In this chapter, section 6.2 presents the MCS model description for E-bikes (closely-coupled LIPT system) and EVs (loosely-coupled LIPT system). Section 6.3 presents the results of the MCS models for E-bikes. Section 6.4 presents the results of the MCS models for EVs. Section 6.5 presents the results of the MCS model with misalignment: a case study for EVs and section 6.6 concludes this chapter.

6.2 MCS Model Description for E-bikes and EVs

The description of the MCS models for E-bikes and EVs are presented in this section. The technical specifications for the MCS modelling are given in Tables 6.1 and 6.2.

TABLE 6.1: Realistic parameters of MCS model for E-bike

Fixed coil separation distance of 1.8 cm

Technical specifications	Primary coil	Secondary coil
Coil used	Copper	Copper
Coil outer diameter	10 cm	10 cm
Coil thickness	2 cm	2 cm
Coil inner diameter	8 cm	8 cm
Coil wire type	Litz	Litz
Number of turns	30	30
Height of coil	10 cm	6.7 cm
Coil shape	circular cylinder	circular cylinder
Coil wire area	1.5 mm^2	1.5 mm^2
Sinusoidal current	16 A_{rms} at 20kHz	0
Litz wire diameter	1.3820 mm	1.3820 mm
Skin depth at 20kHz	460 μm	460 μm
Magnetic core	ferrite	ferrite
Magnetic core shape	circular cylinder	circular cylinder
μ_r of ferrite	2300	2300
Height of ferrite core	10 cm	6.7 cm

TABLE 6.2: Realistic parameters of MCS model for EVs

EVs require a ground clearance up to 20 cm

Technical Specifications	Primary coil	Secondary coil
Coil used	Copper	Copper
Coil outer diameter	70 cm	70 cm
Coil thickness	2.5 cm	2.5 cm
Coil inner diameter	67.5 cm	67.5 cm
Coil wire type	Litz	Litz
Number of turns	18	18
Height of coil	70 cm	46.7 cm
Coil shape	circular cylinder	circular cylinder
Coil wire area	4 mm^2	4 mm^2
Sinusoidal current	23 A_{rms} at 20kHz	0
Litz wire diameter	2.2568 mm	2.2568 mm
Skin depth at 20kHz	460 μm	460 μm
Magnetic core	ferrite	ferrite
Magnetic core shape	circular cylinder	circular cylinder
μ_r of ferrite	2300	2300
Height of ferrite core	70 cm	46.7 cm

With the objective of having a proper arrangement of the ferrite cores either within or outside the circular cylindrical coils, it is vital to ensure that the magnetic cores to be incorporated have equal radii. The formulated models given in equations (6.1)

and (6.2) are used to achieve that aim, and the equations are developed based on Fig. 6.1 (see Figs. 6.2 and 6.3 for further clarification).

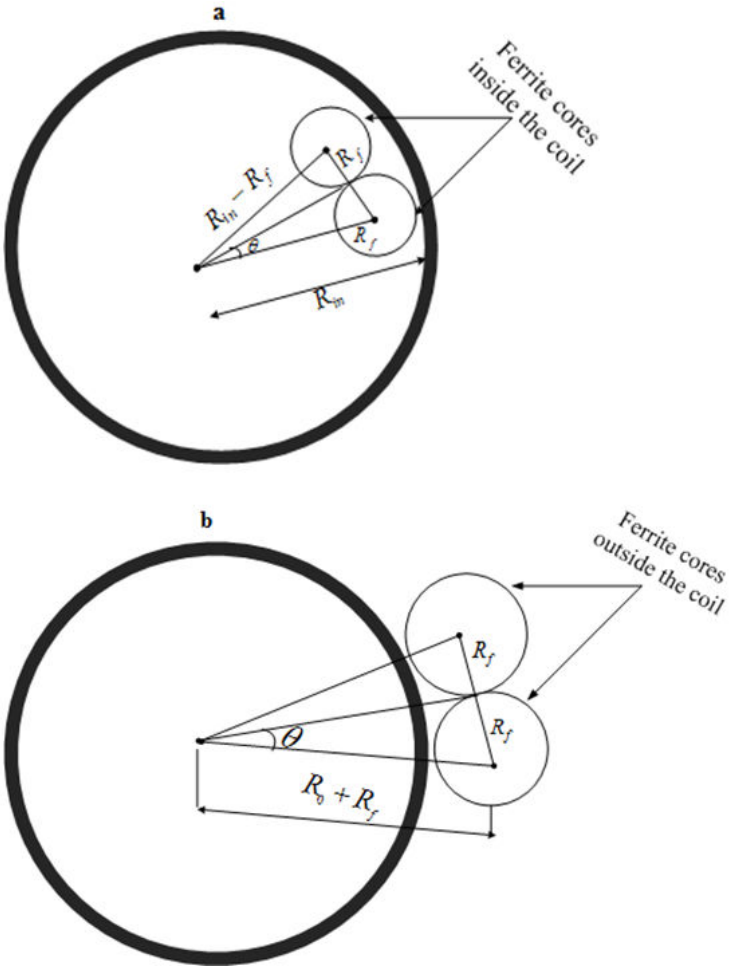

FIGURE 6.1: Sketch showing ferrite cores (a) inside and (b) outside the coils
A simple diagram for determining the general formula for calculating the radius of each ferrite core to be incorporated around the primary and secondary coils.

$$R_{f_{inside}} = R_f = \frac{R_{in} sin(\frac{\pi}{N_f})}{1 + sin(\frac{\pi}{N_f})} \tag{6.1}$$

$$R_{f_{outside}} = R_f = \frac{R_0 sin(\frac{\pi}{N_f})}{1 - sin(\frac{\pi}{N_f})} \tag{6.2}$$

where $R_{f_{inside}}$ is the radius for each ferrite core to be incorporated inside the coils, $R_{f_{outside}}$ is the radius for each ferrite core to be incorporated outside the coils, R_{in} is the coil inner radius, and it is given by $R_{in} = R_0 - R_{th}$ where R_0 is the coil outer radius and R_{th} is the coil thickness. θ is given by $\frac{\pi}{N_f}$ where N_f refers to the number of ferrite cores to be incorporated either inside or outside the coils. It is vital to note that N_f may be 6, 8, 12, 16 or 24 ferrite cores.

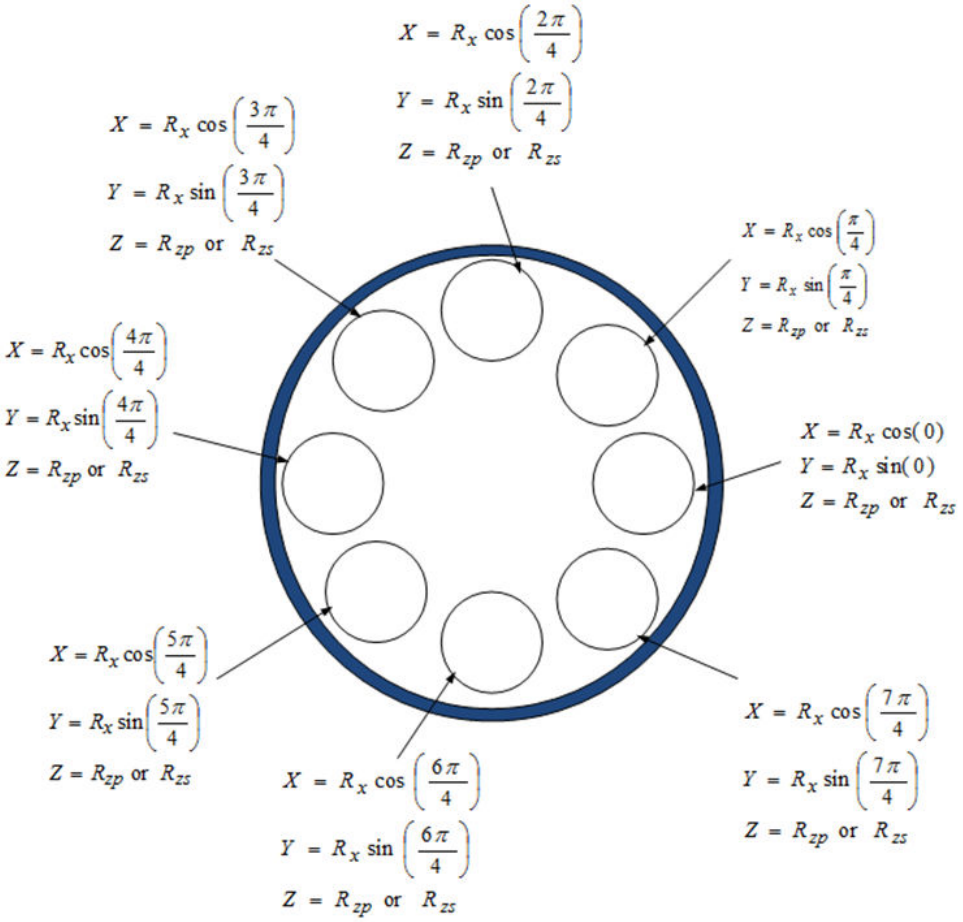

FIGURE 6.2: Proper placement of ferrite cores within the coil
Geometric formula for proper arrangement of 8 ferrite cores inside the coil. Based on equations (6.1) and (6.2) as well as the XYZ positioning given in Fig. 6.2, other proper configurations of ferrites cores within the coils can be achieved.

Furthermore, the geometric formulas given in Figs 6.2 and 6.3 are used to obtain a proper XYZ placement of the ferrite cores either within or outside the coils. Based

on Fig. 6.1, $R_x = (R_0 - R_{th}) - R_f$ and $R_{xout} = R_0 + R_f$. Concerning the MCS models for E-bike and EV, $R_{zp} = \frac{-H_P}{2}$. In this study, for the case with E-bike, $R_{zs} = \frac{H_P}{1.4706}$ whereas for EV, $R_{zs} = \frac{H_P}{1.2727}$. H_P refers to the height of the ferrite core, R_x and R_{xout} respectively define the XY positioning of the ferrite cores inside and outside the coils whereas R_{ZP} and R_{ZS} respectively define the Z positioning of the ferrite core in the primary and secondary coils.

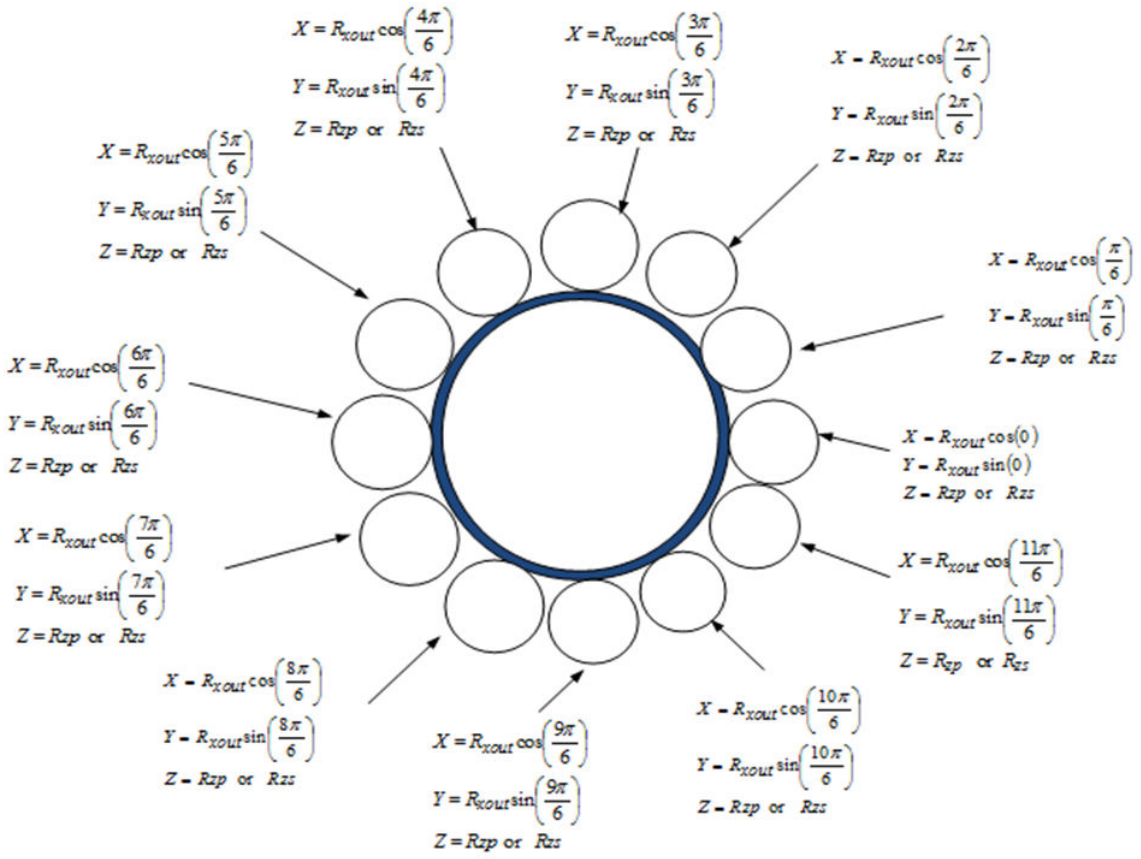

FIGURE 6.3: Proper placement of ferrite cores outside the coil
Geometric formula for proper positioning of 12 ferrite cores outside the coil. Based on equations (6.1) and (6.2) as well as the XYZ positioning given in Fig. 6.3, other proper configurations of ferrites cores outside the coils can be achieved.

With the use of COMSOL multiphysics software, the following steps are carried out in order to achieve the purpose of this thesis:

- The development of the 3-D MCS model geometry is implemented based on the technical specifications given in Tables 6.1 and 6.2.

- Air material, copper material, ferrite cores, non-conducting magnetic material that covers the coils and chassis (i.e., underbody structure) of EVs are incorporated in the MCS model geometry developed.

- Magnetic fields (mf) is the physics studied in the MCS model developed. In addition, it comprises Ampere's law, magnetic insulation and multi-turn coil domains for the primary and secondary coils.

- Finer mesh of the MCS model is implemented. This is because the finer the mesh the greater the accuracy of the results obtained.

- AC frequency domain solver is employed. That is, frequency domain electromagnetic field modelling with the AC/DC module is implemented in this research study. This is because the AC/DC module of COMSOL offers a frequency domain form of the magnetic fields interface. Thus magnetic field is not set up for time dependent solvers. Also, in COMSOL, transient analysis is not available for 3-D magnetic fields analysis.

- The model equations for the frequency domain study of magnetic fields are obtained from COMSOL as

$$J_e = (j\omega\sigma - \omega^2\epsilon_0\epsilon_r)A + \nabla \times (\mu_0^{-1}\mu_r^{-1}B) - \sigma v \times B \tag{6.3}$$

$$B = \nabla \times A \tag{6.4}$$

where $J_e = \frac{NI_{coil}}{A} e_{coil}$ and $B = \mu_0 \mu_r H$ are respectively the multi-turn coil equation and the constitutive relation. B is the magnetic flux density, H is the magnetic field strength, μ_0 is the permeability of free space, μ_r is the relative permeability of air, σ is the electrical conductivity, v is the electric scalar potential, J_e is the uniformly external current desnity in the Litz wire, A is the magnetic vector potential, N is the multi-turn coil, I_{coil} is the primary coil current, e_{coil} is the coil excitation, which is current, ω is the angular frequency, which is given by $2\pi f$, ϵ_0 is the permittivity of vacuum and ϵ_r is the relative permittivity of copper.

- Lastly, results for the AC magnetic flux density in 1-D, 2-D and 3-D are obtained as well as the values for the mutual inductance and induced voltage.

6.3 Presentation of Results: MCS for E-bike

6.3.1 MCS Models without Magnetic core

The MCS model geometry without ferrite cores, but with structural steel cover is shown in Fig. 6.4. Firstly, air material ($\mu_r = 1, \epsilon_r = 1$ and $\sigma = 0.01\ \frac{S}{m}$) is applied to the model (see Figs. 6.4a and 6.4b). Normally, $\sigma_{air} = 0$, but to avoid singularities in the model, it is arbitrarily set to a small value. In this study, in order to stabilize the frequency domain solver, $\sigma_{air} = 0.01\ \frac{S}{m}$ is used. Afterwards, copper ($\mu_r = 1, \epsilon_r = 1$ and $\sigma = 6 \times 10^7\ \frac{S}{m}$) and structural steel materials are incorporated in the model (see Figs. 6.4c and 6.4d respectively).

Structural steel is a non-conducting magnetic material ($\mu_r = 1, \epsilon_r = 1$ and $\sigma = 4.032 \times 10^7 \frac{S}{m}$), which covers the bottom part of the primary coil and the top part of the secondary coil. This is done to help improve the mutual coupling between the coils. In addition, Fig. 6.5 shows the mesh type employed (see Fig. 6.5a) and the results obtained (see Figs. 6.5b to 6.5d) for the model shown in Fig. 6.4. A finer mesh is used because the finer the mesh the greater the accuracy of the results obtained.

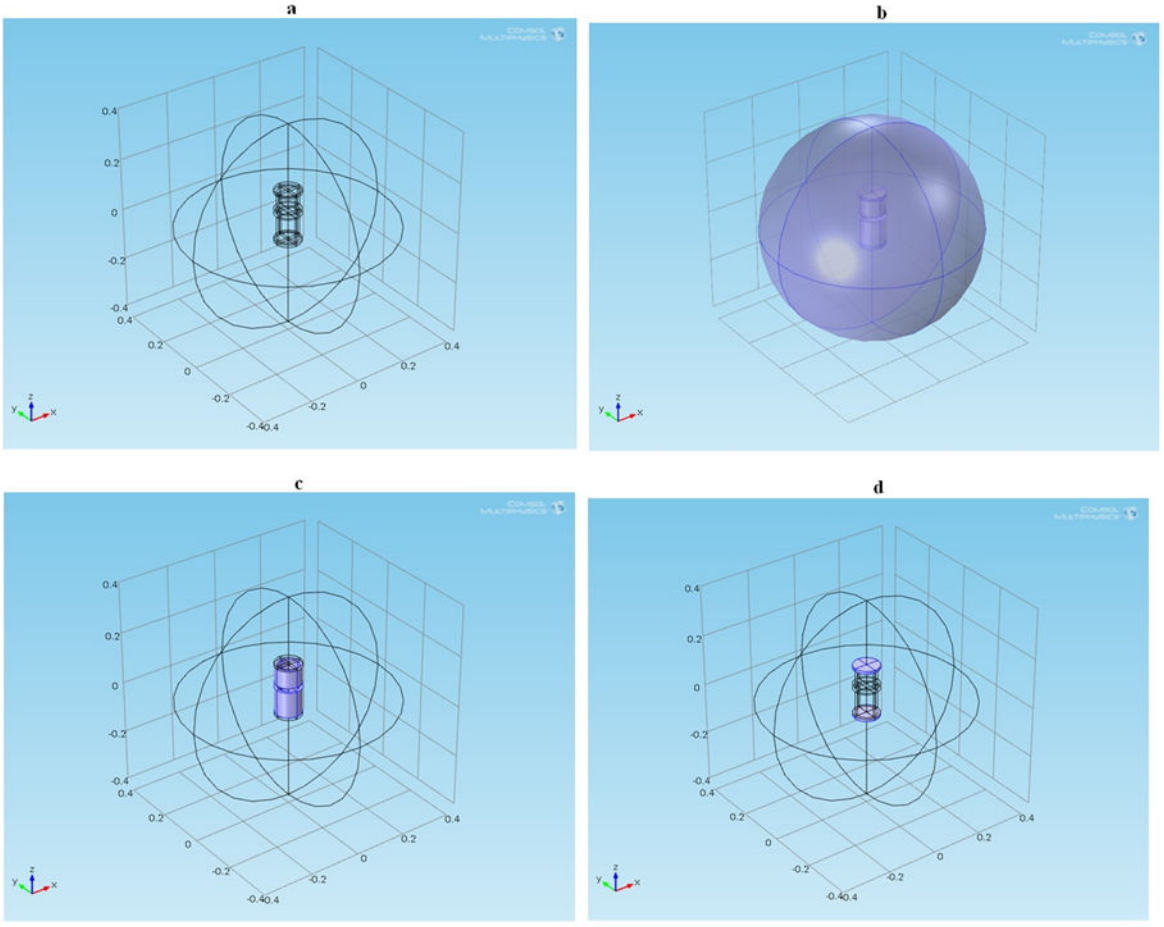

FIGURE 6.4: MCS model without ferrite core, but with structural steel cover (a) 3-D geometry (b) air material (c) copper material (d) structural steel cover

Figure 6.6 shows the MCS model geometry without ferrite cores, but with iron cover ($\mu_r = 4000, \epsilon_r = 1$ and $\sigma = 1.12 \times 10^7 \frac{S}{m}$). The results obtained for this model are given in Fig. 6.7. With the use of iron cover, the values obtained for the mutual

inductance and induced voltage are small compared to the ones obtained with structural steel cover (see Table 6.3). Also, the 1-D plots given in Figs. 6.5d and 6.7d show that with structural steel cover, a uniformly distributed magnetic flux density is obtained compared to the case with iron cover. Thus to ensure that a uniform distribution of the magnetic flux density around the coils is achieved, structural steel cover is employed in this study for the covering of the bottom part of the primary coil and the top part of the secondary coil.

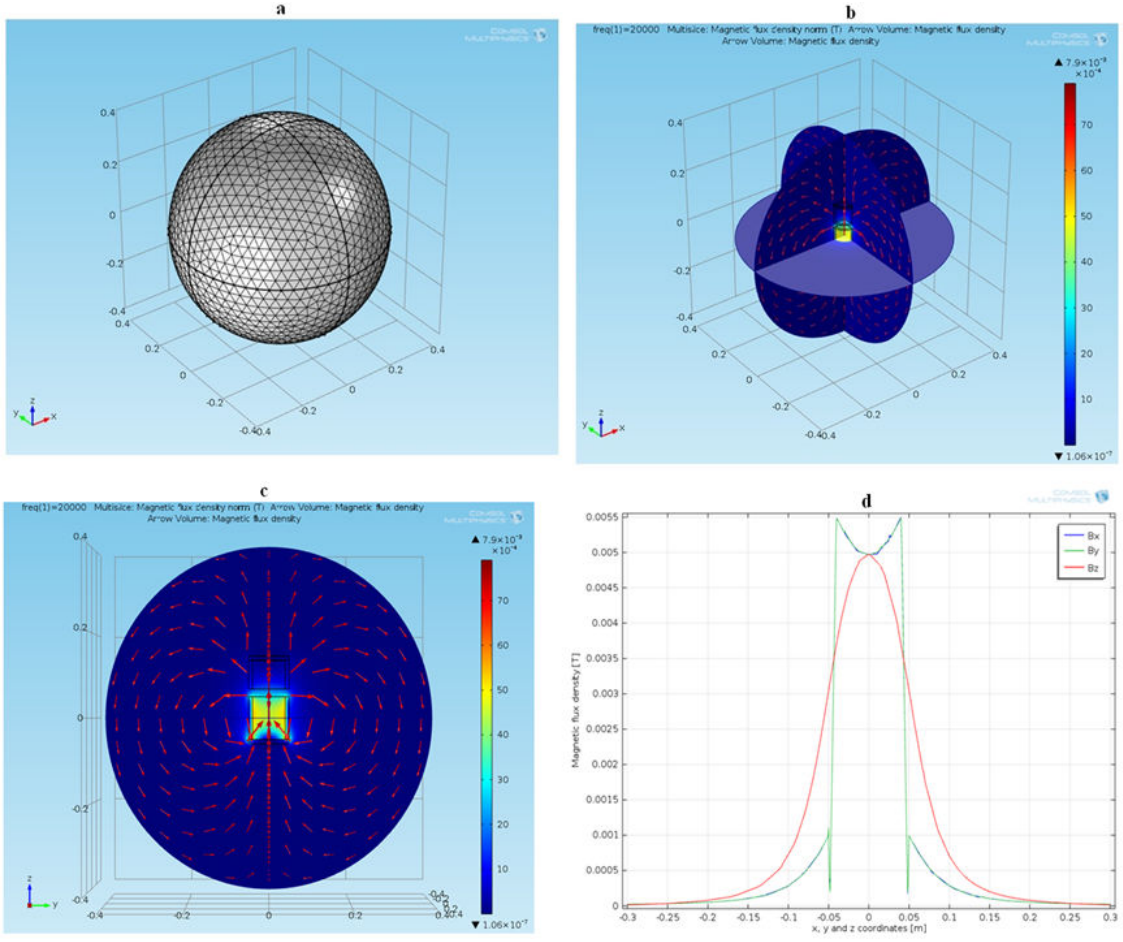

FIGURE 6.5: Results for MCS without ferrite core, but with structural steel cover (a) finer mesh, AC magnetic flux density plots in: (b) xyz plane, (c) yz plane and (d) 1-D plot: magnetic flux density versus x, y and z coordinates

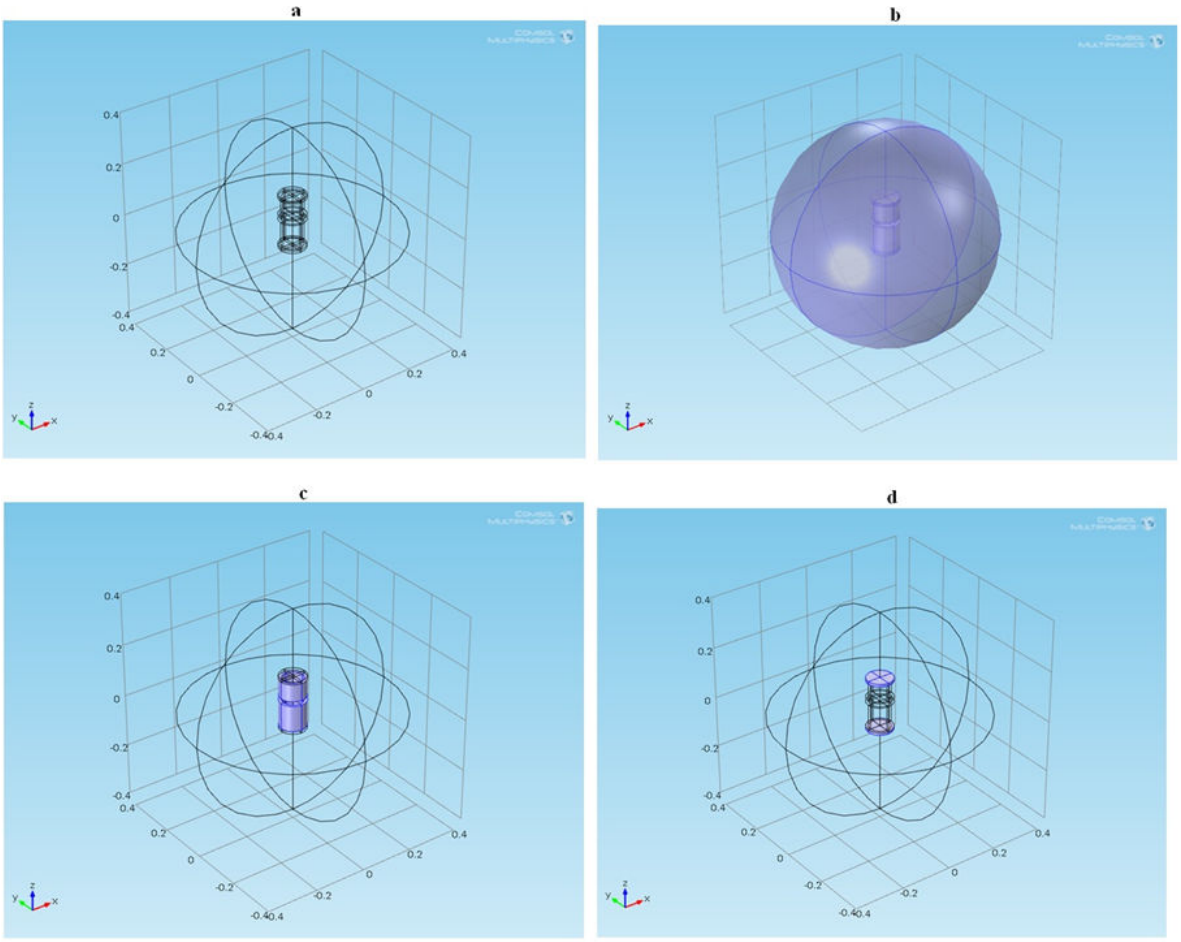

FIGURE 6.6: MCS model without ferrite core, but with iron cover
(a) 3-D geometry (b) air material (c) copper material (d) iron cover

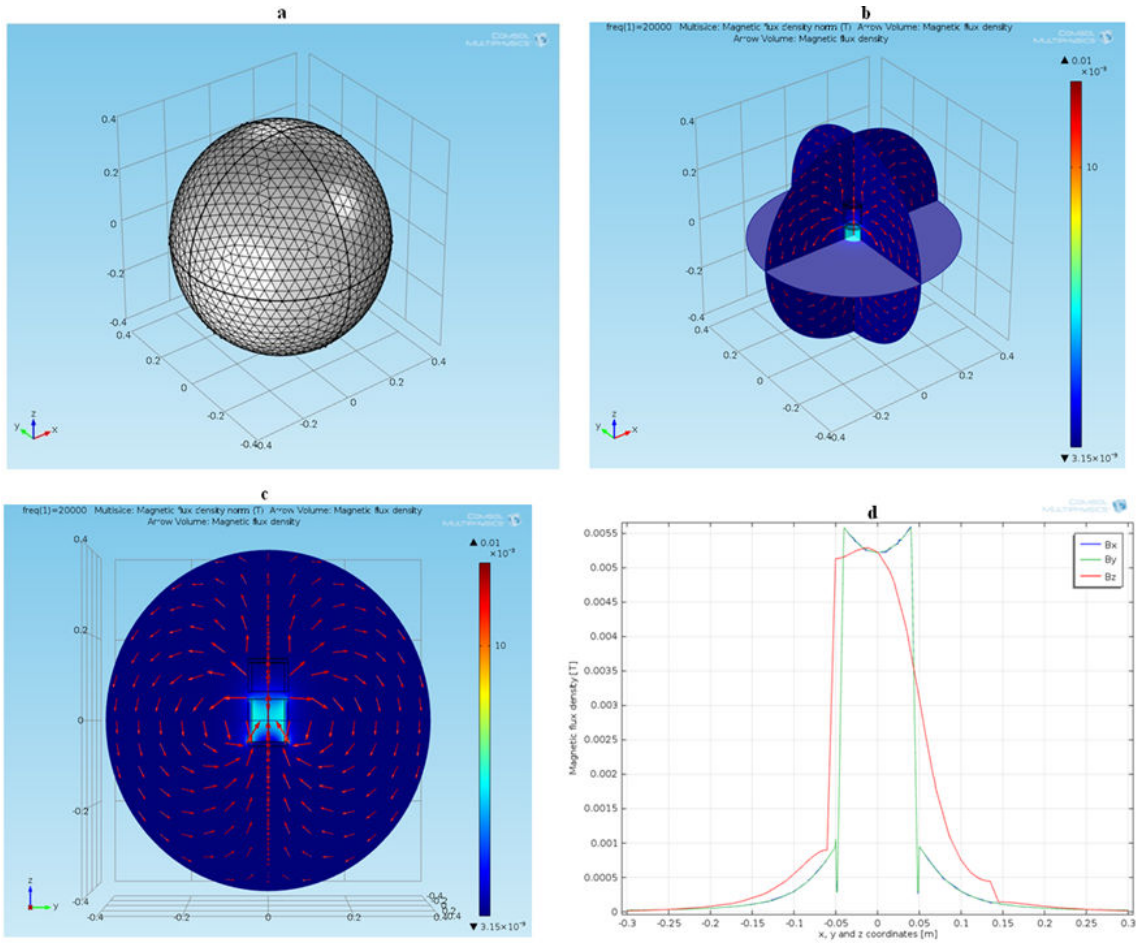

FIGURE 6.7: Results for MCS model without ferrite core, but with iron cover (a) finer mesh, AC magnetic flux density plots in: (b) xyz plane, (c) yz plane and (d) 1-D plot: magnetic flux density versus x, y and z coordinates

TABLE 6.3: Comparisons between structural steel and iron covers

MCS models	Mutual inductance (nH)	Induced voltage (V)	1-D plot
Structural steel cover	61.886	0.1240	see Fig. 6.5d
Iron cover	59.520	0.1200	see Fig. 6.7d

6.3.2 MCS Models with only Magnetic core for E-bike

The MCS models presented in subsection 6.3.1 comprise air-cored coils with cover material for the coils. They do not have magnetic core thus a very low mutual inductance and induced voltage are obtained (see Figs. 6.5 and 6.7 and Table 6.3).

A magnetic core is a piece of magnetic material with a high permeability. It is used to confine and guide magnetic fields in electrical, electromechanical and magnetic devices. The presence of the magnetic core can increase the magnetic field of a coil, the mutual inductance between the air-cored coils and induced voltage by a factor of several thousand over what it would be without the core. Thus the use of magnetic core can enormously concentrate the strength and increase the effect of magnetic fields produced by electric currents (see Figs. 6.8, 6.9 and 6.10).

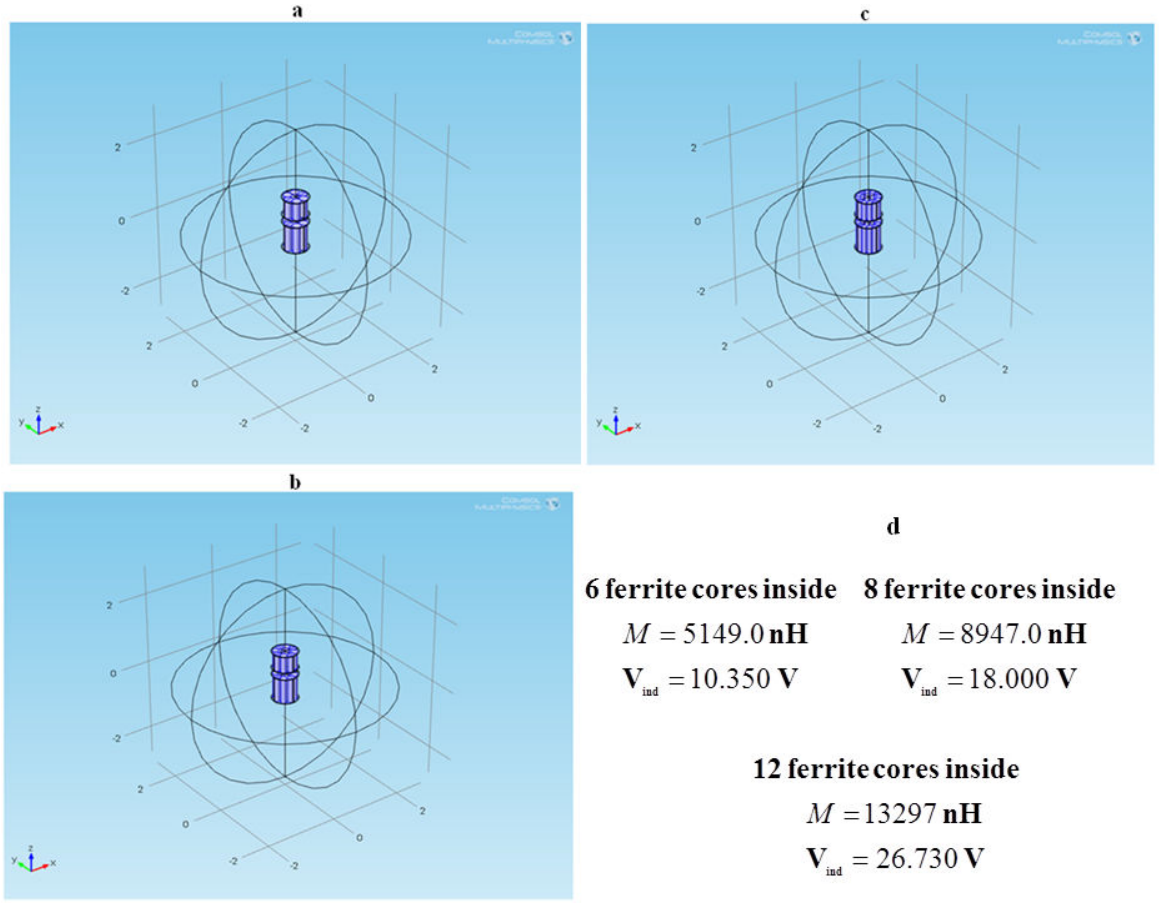

FIGURE 6.8: MCS model with ferrite cores inside: E-bike case study Proper configuration of ferrite cores inside the air-cored coils: (a) 6 ferrite cores (b) 8 ferrite cores (c) 12 ferrite cores (d) derived values for the induced voltage and mutual inductance.

In this subsection, MCS models with only ferrite cores ($\mu_r = 2300, \epsilon_r = 1$ and $\sigma = 0$)

inside, outside and both are investigated, and the proper arrangement of the ferrite cores are based on equations (6.1) and (6.2) together with the concept behind the geometric formulas given in Figs. 6.2 and 6.3.

Given in Figs. 6.8a, 6.8b and 6.8c are the MCS models with only $6, 8$ and 12 ferrite cores inside respectively. Also, Figs. 6.9a, 6.9b and 6.9c show the MCS models with only $12, 16$ and 24 ferrite cores outside respectively. Lastly, Figs. 6.10a, 6.10b and 6.10c show the MCS models with only 6 cores inside and 12 cores outside, 8 cores inside and 16 cores outside, 12 cores inside and 24 cores outside respectively.

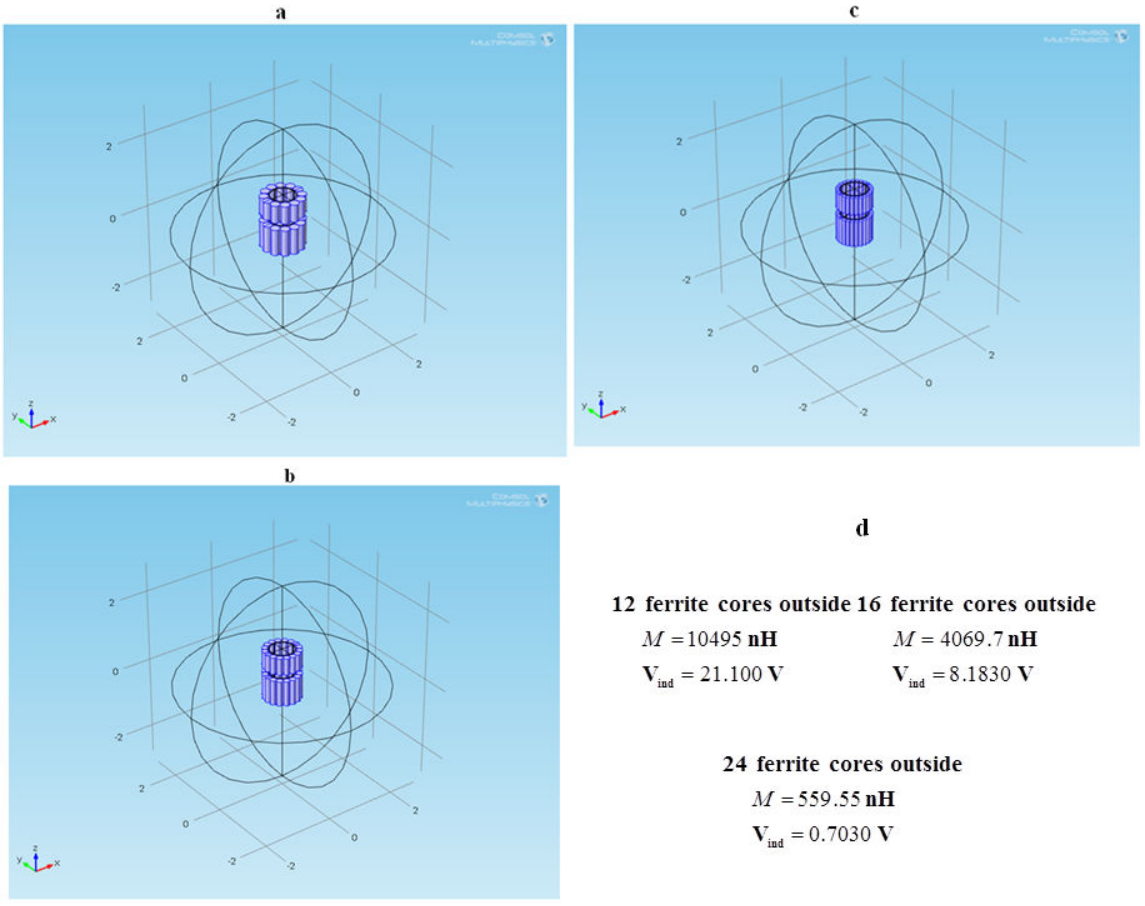

FIGURE 6.9: MCS model with ferrite cores outside: E-bike case study
Proper configuration of ferrite cores outside the air-cored coils: (a) 12 ferrite cores (b) 16 ferrite cores (c) 24 ferrite cores (d) derived values for the induced voltage and mutual inductance.

It is important to note that the performance of the designed models are determined by the values of the mutual inductance and induced voltage obtained from COMSOL. Thus based on the values obtained in Figs. 6.8d, 6.9d and 6.10d, the order of performance of the MCS models with only ferrite cores is as follows: (1^{st}) 8 ferrite cores inside and 16 ferrite cores outside, (2^{nd}) 12 ferrite cores inside and (3^{rd}) 12 ferrite cores outside (see Table 6.4).

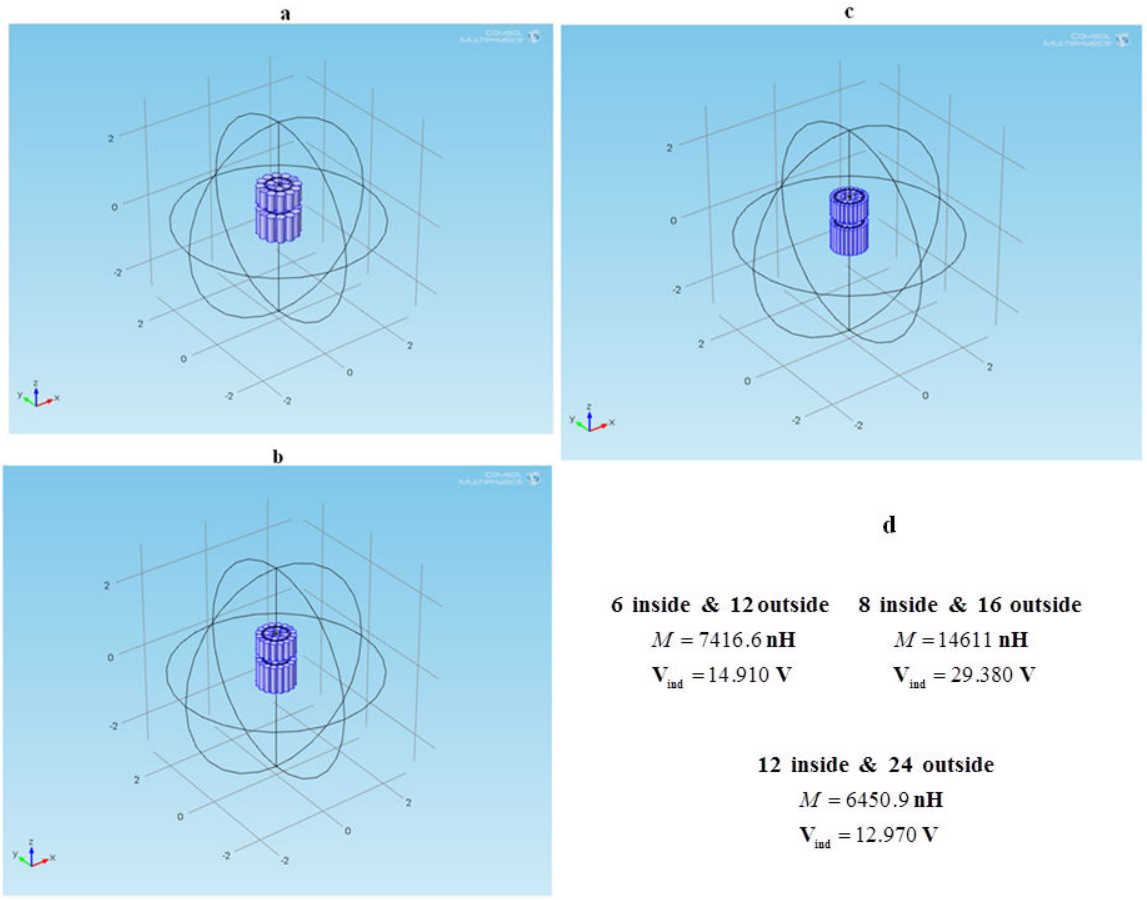

FIGURE 6.10: MCS model with ferrite cores inside and outside: E-bike case study Proper configuration of ferrite cores inside and outside the air-cored coils: (a) 6 inside and 12 outside (b) 8 inside and 16 outside (c) 12 inside and 24 outside (d) derived values for the induced voltage and mutual inductance.

TABLE 6.4: MCS models with only ferrite cores: case study for E-bike

Order of performance	Mutual inductance (nH)	Induced voltage (V)	MCS models
1	14611	29.380	see Fig. 6.10b
2	13297	26.730	see Fig. 6.8c
3	10495	21.100	see Fig. 6.9a

6.3.3 Overall Performance of MCS Model for E-bike

In this section, a complete MCS model with ferrite cores and structural steel cover (see Figs. 6.11, 6.12 and 6.13) is implemented based on the order of performance presented in Table 6.4.

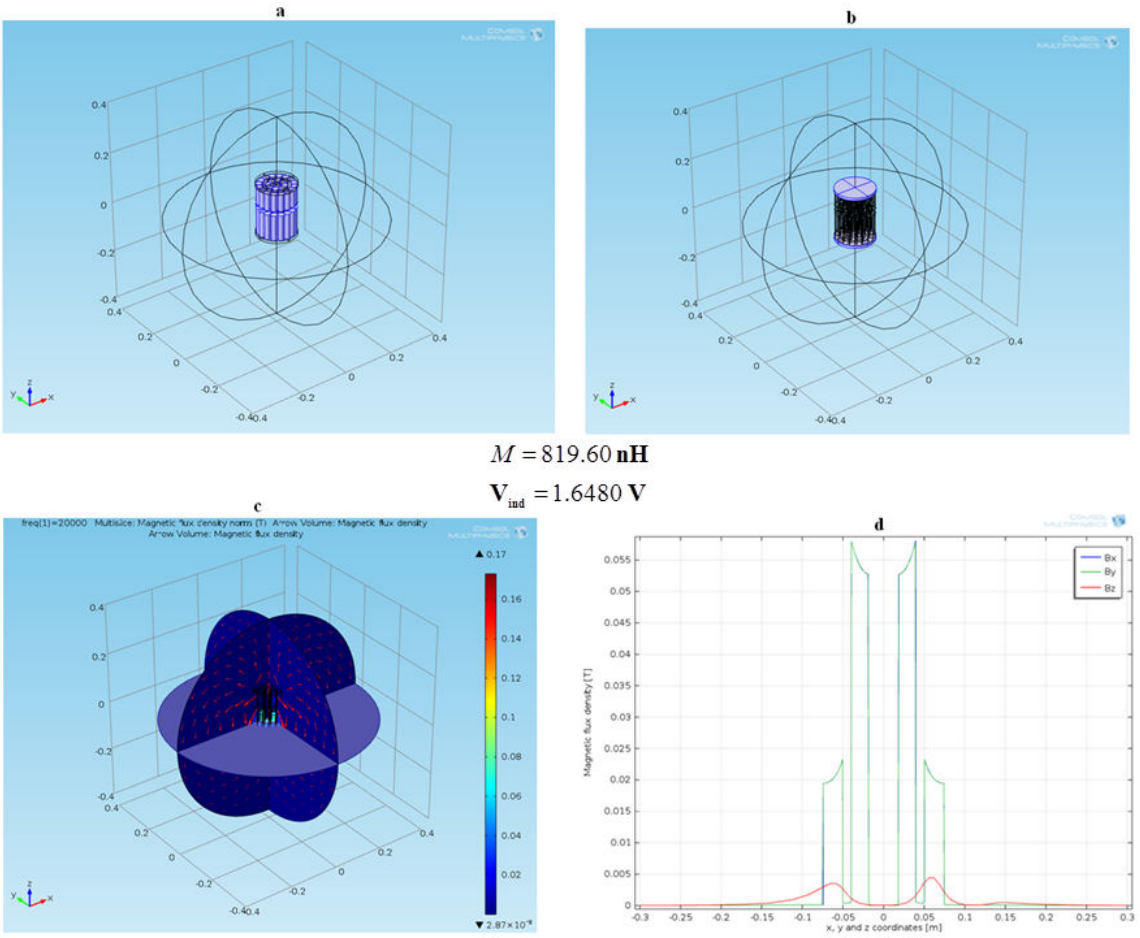

FIGURE 6.11: E-bike - a complete MCS model with cores inside and outside Incorporation of (a) 8 ferrite cores inside and 16 ferrite cores outside and (b) structural steel cover (c) AC magnetic flux density plot in 3-D and (d) 1-D plot: magnetic flux density versus x, y and z coordinates.

In this research study, the overall performance of the complete models is determined by the values of the mutual inductance and induced voltage obtained from COMSOL. Based on that information, the best MCS model design for E-bikes is as follows: The

first is the complete MCS model comprising 12 ferrite cores (see Fig. 6.13), the **second** is the complete MCS model comprising 12 ferrite cores inside (see Fig. 6.12) and the **third** is the complete MCS model comprising 8 ferrite cores inside and 16 ferrite cores outside (see Fig. 6.11).

By taking Fig. 6.5 as the basis for comparison (see Table 6.5), it is found out that with the incorporation of ferrite cores in the complete MCS models, the performance of the system is 13 times better (see Figs. 6.5 and 6.11), 27 times better (see Figs. 6.5 and 6.12) and 37 times better (see Figs. 6.5 and 6.13).

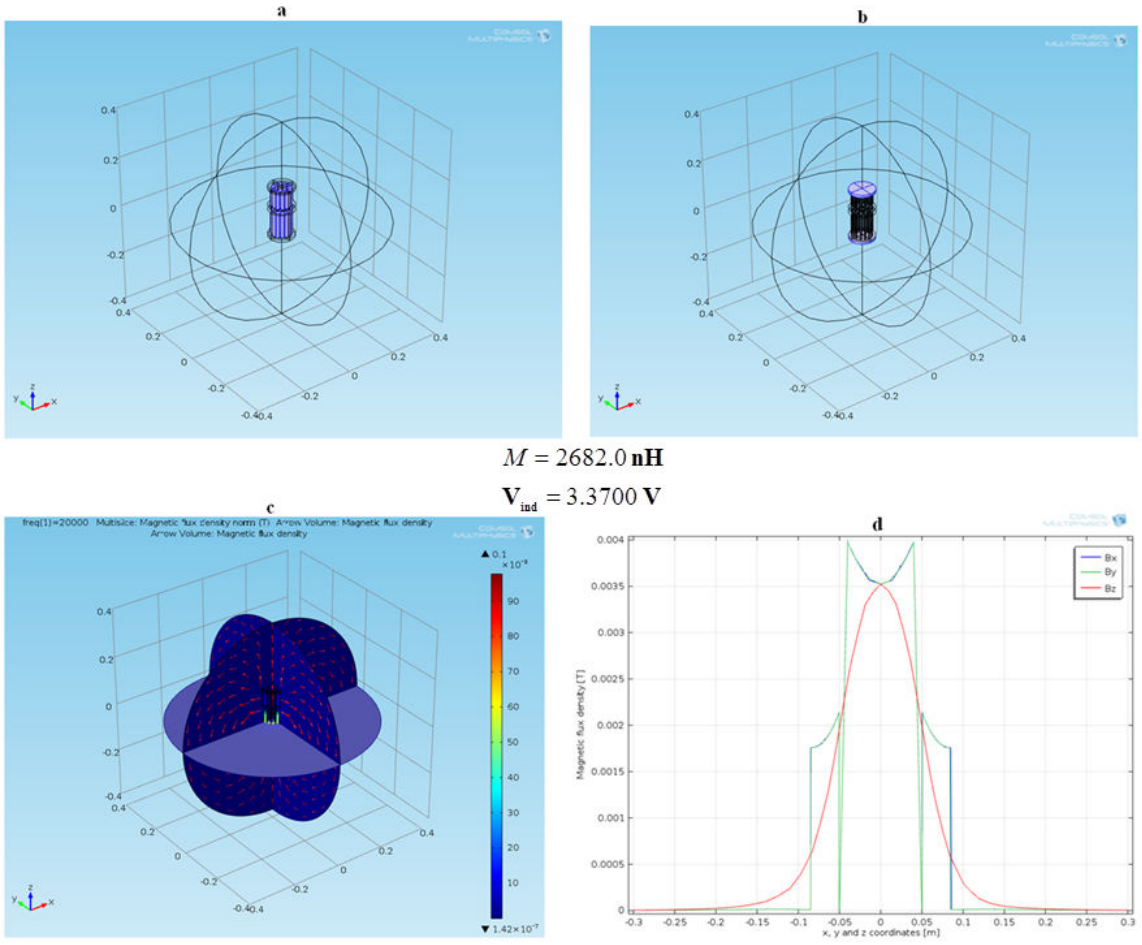

FIGURE 6.12: E-bike - a complete MCS model with cores inside
Incorporation of (a) 12 ferrite cores inside and (b) structural steel cover (c) AC magnetic flux density plot in 3-D and (d) 1-D plot: magnetic flux density versus x, y and z coordinates.

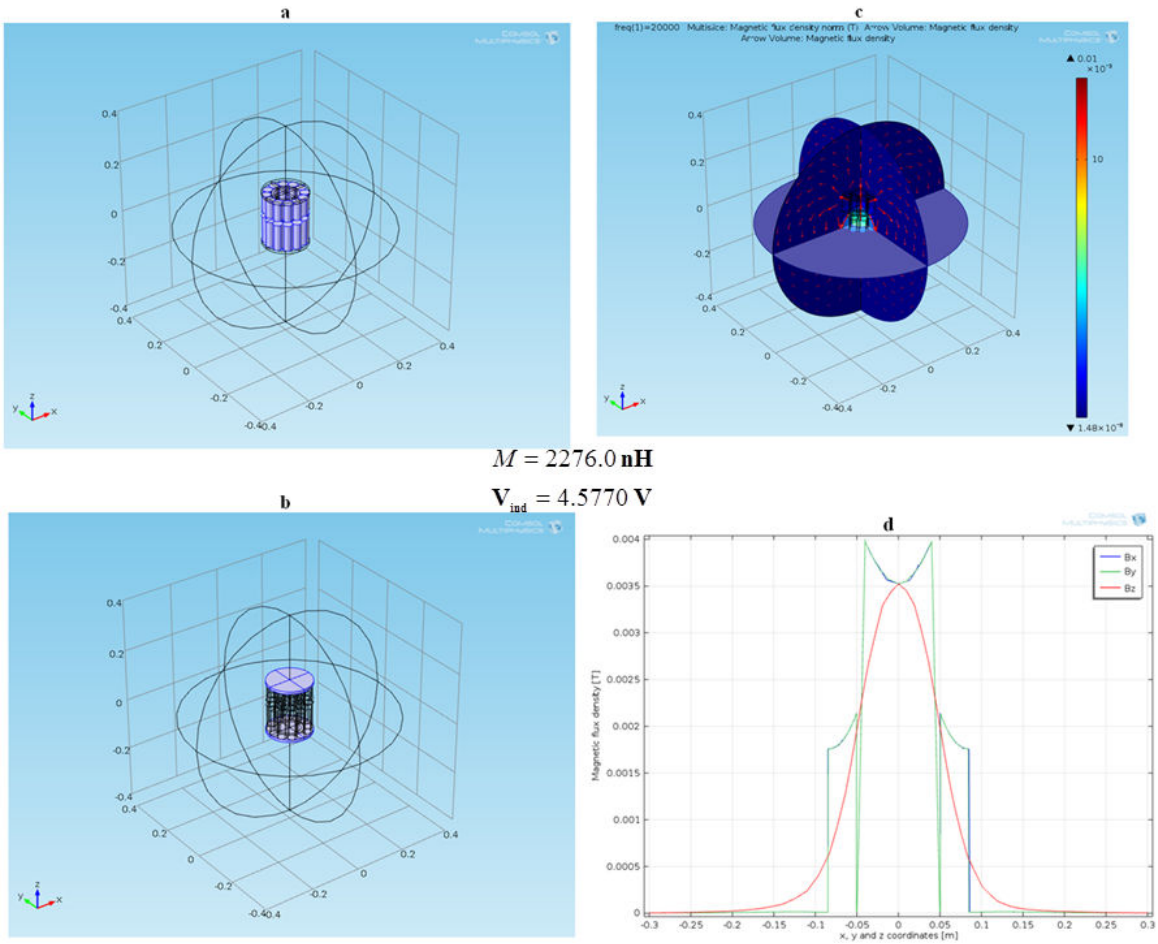

FIGURE 6.13: E-bike - a complete MCS model with cores outside Incorporation of (a) 12 ferrite cores outside and (b) structural steel cover (c) AC magnetic flux density plot in 3-D and (d) 1-D plot: magnetic flux density versus x, y and z coordinates.

TABLE 6.5: Complete MCS models: case study for E-bike

Order of performance	Mutual inductance (nH)	Induced voltage (V)	MCS models	Model Performance
1	2276.0	4.5770	compare Figs. 6.5 and 6.13	37
2	2682.0	3.3700	compare Figs. 6.5 and 6.12	27
3	819.60	1.6480	compare Figs. 6.5 and 6.11	13

This section presents a complex and realistic MCS model for a closely-coupled LIPT system: a case study for E-bike. In conclusion, the complete MCS models, which incorporate structural steel cover with several arrangements of ferrites show that the complete design of MCS model with 12 ferrite cores outside is most the suitable and effective model for the battery charging of E-bikes.

6.4 Presentation of Results: MCS Models for EVs

6.4.1 MCS Models without Magnetic core

The MCS model geometry given in Fig. 6.14a does not have ferrite cores. However, it comprises the air material (see Fig. 6.14b), copper material (see Fig. 6.14c) and structural steel that covers the bottom part of the primary coil and top part of the secondary coil (see Fig. 6.14d). The model also includes iron plate ($\mu_r = 4000, \epsilon_r = 1$ and $\sigma = 1.12 \times 10^7 \ \frac{S}{m}$).

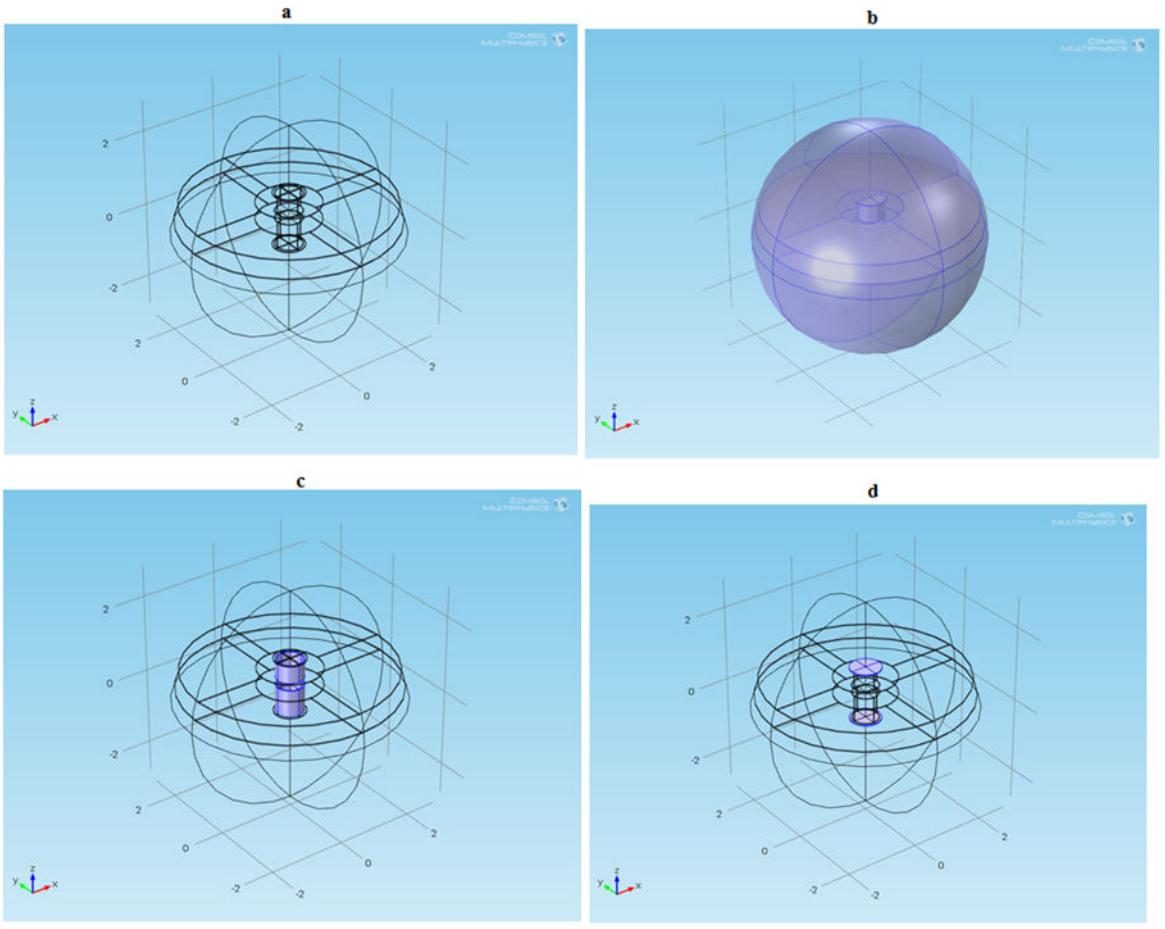

FIGURE 6.14: MCS model for EVs without ferrite cores
(a) 3-D geometry (b) air material (c) copper material (d) structural steel cover

In this study, the iron plate (Fig. 6.15a) is the chassis (i.e., the underbody structure) of EV and also the metallic part covering the primary coil installed underground. The mesh type employed for the model developed is shown in Fig. 6.15b. The results obtained for the 3-D AC magnetic flux density is shown in Fig. 6.15c and the 1-D plot for the magnetic flux density versus x, y and z coordinates are given in Fig. 6.15d.

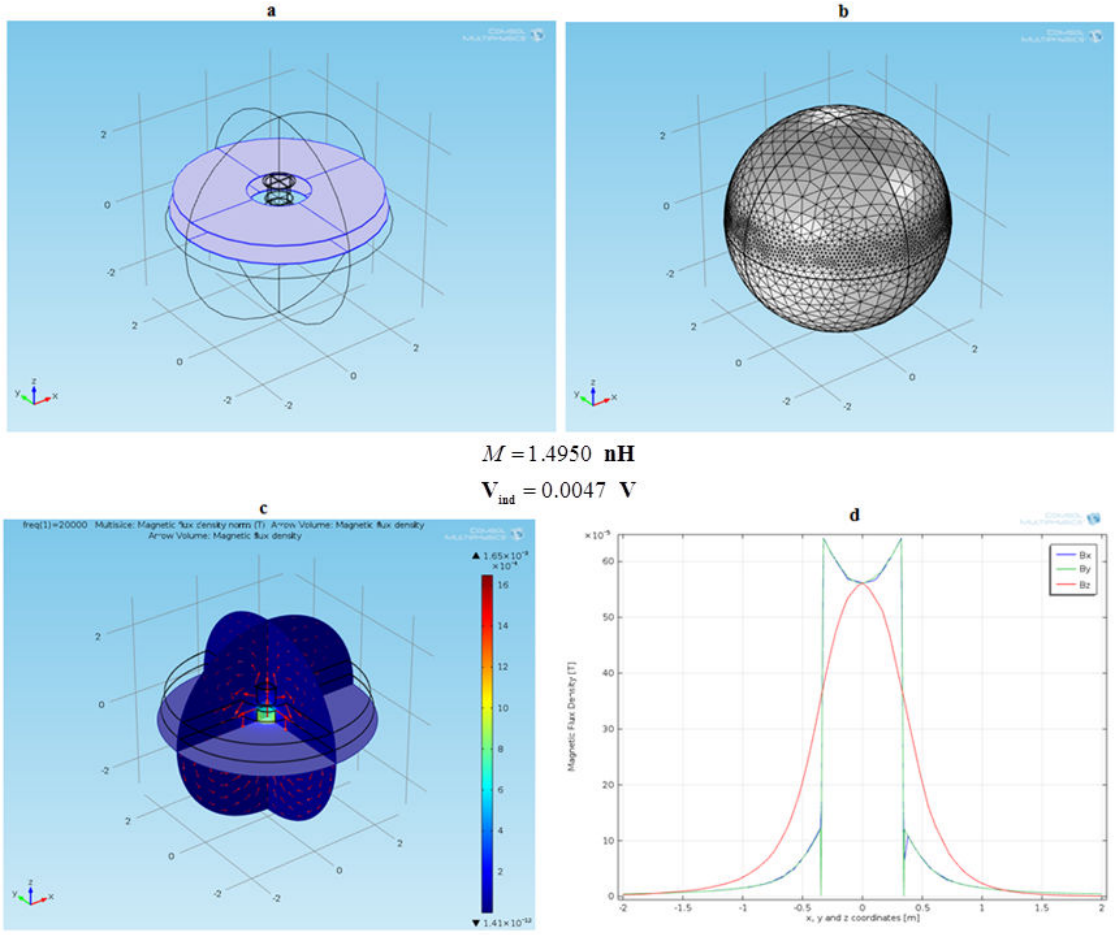

FIGURE 6.15: Results for MCS model for EVs without ferrite cores
(a) Iron plate (b) finer mesh (c) 3-D AC magnetic flux density and (d) 1-D plot for magnetic flux density versus x, y and z coordinates.

6.4.2 MCS Models with only Magnetic core for EVs

The MCS model presented in subsection 6.4.1 does not have ferrite core. Thus a very low mutual inductance and induced voltage of $M = 1.4950\ nH$ and $V_{ind} = 0.0047\ V$ are obtained (see Fig. 6.15).

In this subsection, only MCS models with ferrite cores inside, outside and both are investigated. Also, the proper placement of the cores are based on equations (6.1) and (6.2) plus the concept behind the geometric formulas given in Figs. 6.2 and 6.3.

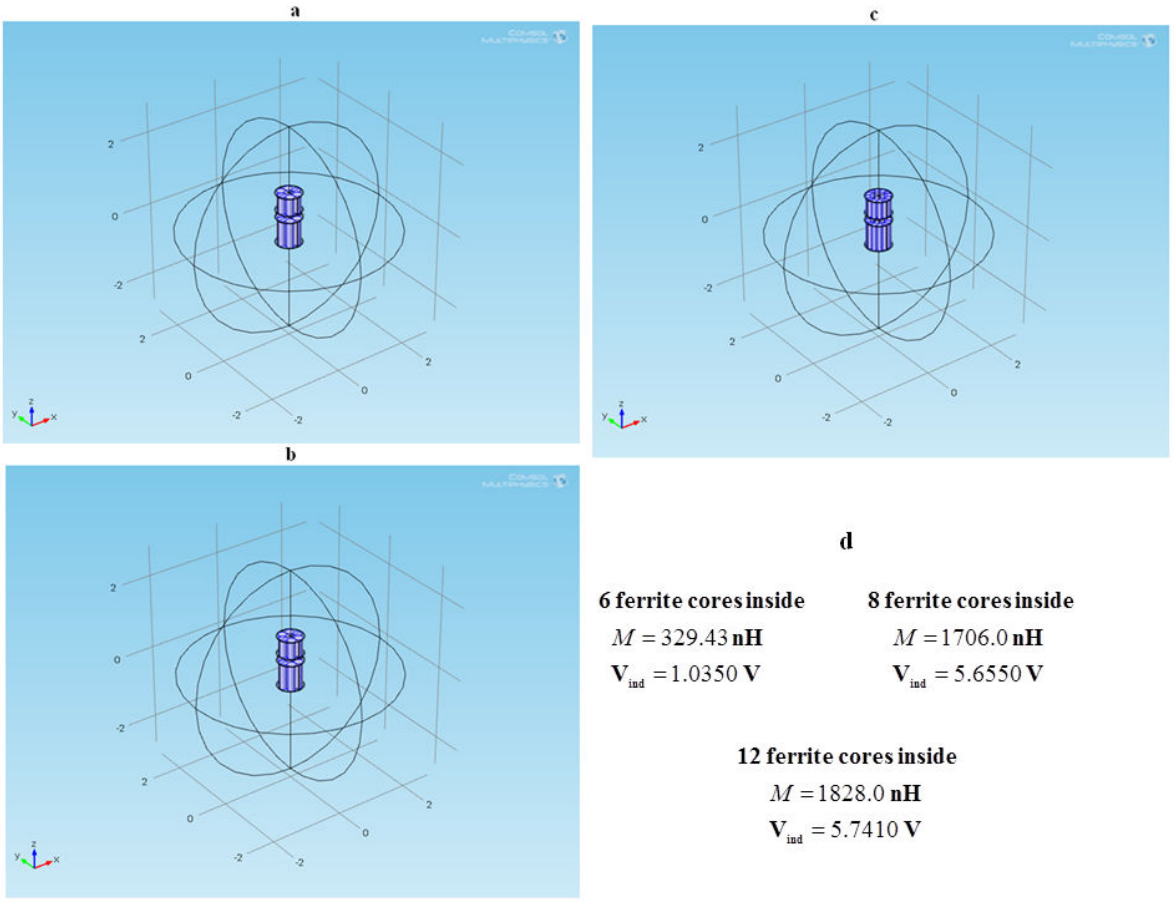

FIGURE 6.16: MCS model with ferrite cores inside: EV case study
Proper arrangement of ferrite cores inside the air-cored coils (a) 6 ferrite cores (b) 8 ferrite cores (c) 12 ferrite cores (d) derived values for the induced voltage and mutual inductance.

Given in Figs. 6.16a, 6.16b and 6.16c are the MCS models with only $6, 8$ and 12 ferrite cores inside respectively. Also, Figs. 6.17a, 6.17b and 6.17c show the MCS models with only $12, 16$ and 24 ferrite cores outside respectively. Lastly, Figs. 6.18a, 6.18b and 6.18c show the MCS models with only 6 cores inside and 12 cores outside, 8 cores inside and 16 cores outside, 12 cores inside and 24 cores outside respectively.

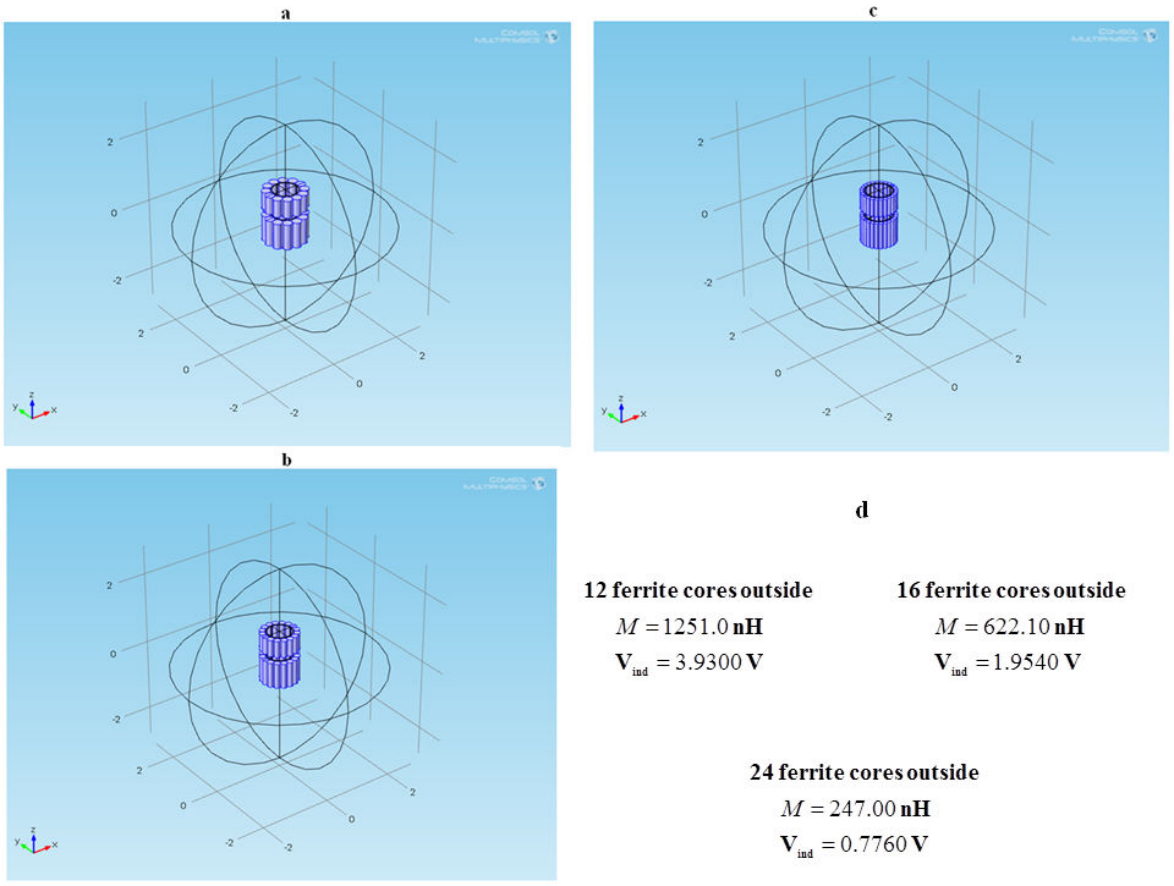

FIGURE 6.17: MCS model with ferrite cores outside: EV case study
Proper placement of ferrite cores outside the air-cored coils (a) 12 ferrite cores (b) 16 ferrite cores (c) 24 ferrite cores (d) derived values for the induced voltage and mutual inductance.

It is important to note that the performance of the designed models are determined by the values of the mutual inductance and induced voltage obtained from COMSOL. Thus based on Figs. 6.16d, 6.17d and 6.18d, the order of performance of the MCS

models with only ferrite cores is as follows: (1^{st}) 12 ferrite cores inside, (2^{nd}) 8 ferrite cores inside and (3^{rd}) 12 ferrite cores outside (see Table 6.6)

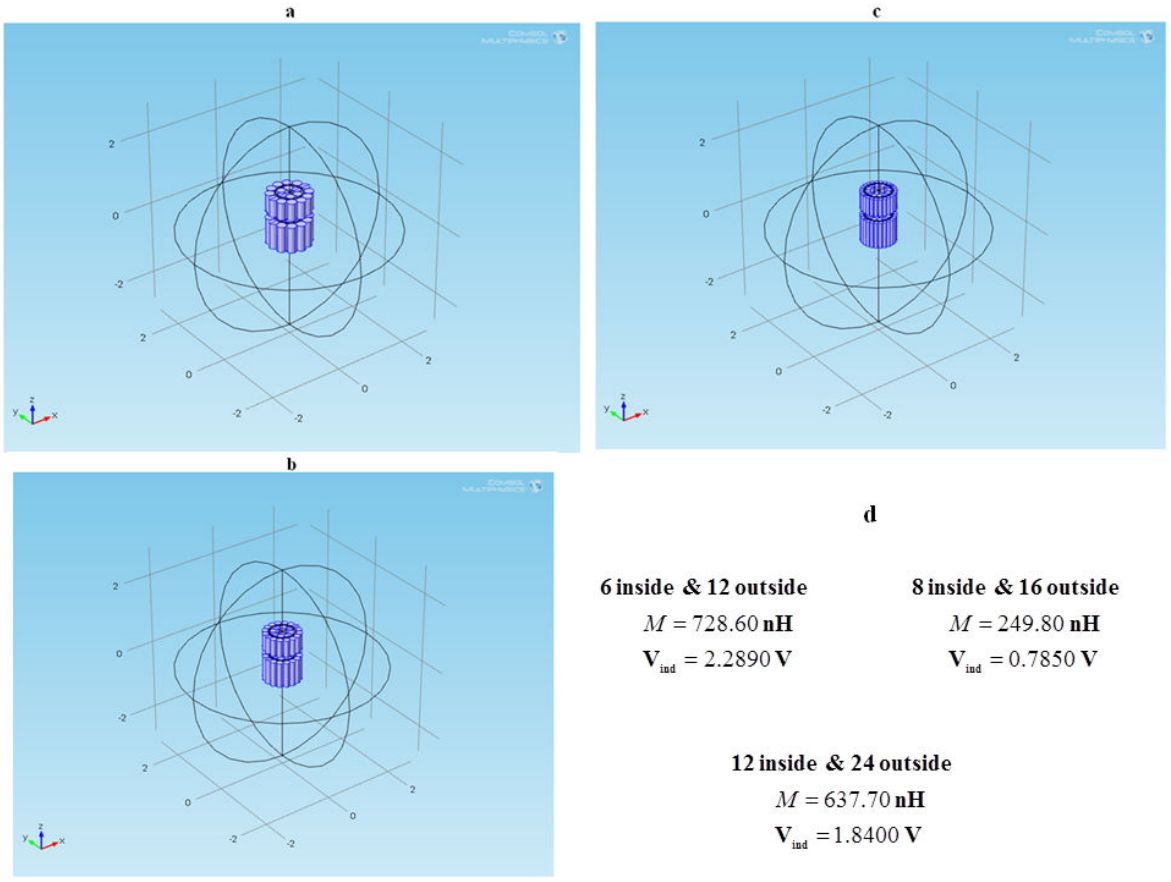

FIGURE 6.18: MCS model with ferrite cores inside and outside: EV case study Proper configuration of ferrite cores inside and outside the air-cored coils (a) 6 cores inside and 12 cores outside (b) 8 cores inside and 16 cores outside (c) 12 cores inside and 24 cores outside (d) derived values for the induced voltage and mutual inductance.

TABLE 6.6: MCS models with only ferrite cores: case study for EVs

Order of performance	Mutual inductance (nH)	Induced voltage (V)	MCS models
1	1828.0	5.7410	see Fig. 6.16c
2	1706.0	5.6550	see Fig. 6.16b
3	1251.0	3.9300	see Fig. 6.17a

6.4.3 Overall Performance of MCS Models for EVs

In this section, a complete MCS model with ferrite cores, structural steel cover, metallic covering of the primary coil installed underground and the underbody structure of EV is implemented based on the order of performance presented in subsection 6.4.2.

The overall performance of the complete MCS models (see Figs. 6.19, 6.20 and 6.21) are determined by the values of the mutual inductance and induced voltage obtained from COMSOL.

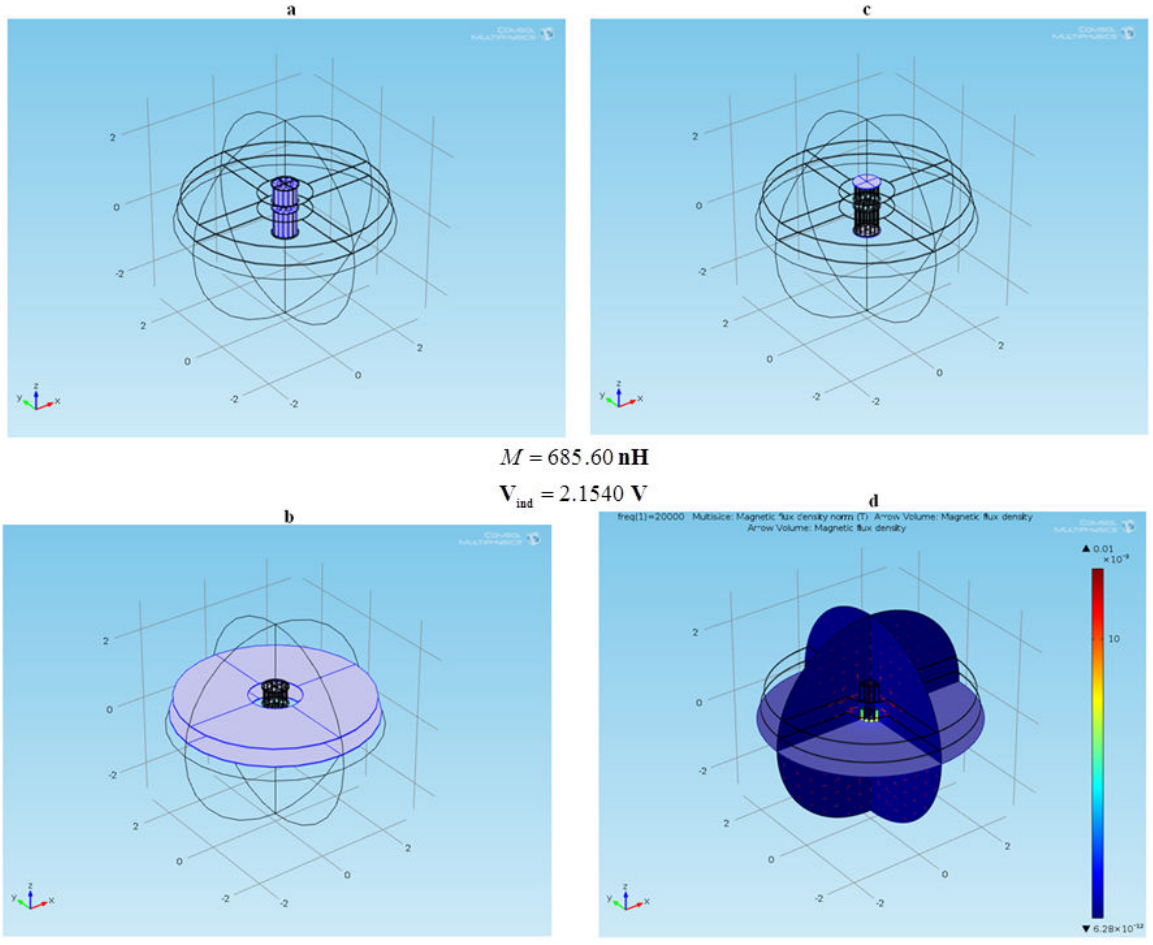

FIGURE 6.19: EV - a complete MCS model with 12 ferrite cores inside
Incorporation of (a) 12 ferrite cores inside (b) structural steel cover (c) underbody structure of EV and the metallic plate that covers the primary coil installed underground, (d) 3-D AC magnetic flux density.

Based on the complete MCS models presented in Figs. 6.19, 6.20 and 6.21, the following are the order of overall performance: the **first** is the complete MCS model with 8 ferrites inside (see Fig. 6.20), the **second** is the complete MCS model with 12 ferrite cores inside (see Fig. 6.19) and the **third** is the complete MCS model with 12 ferrite cores outside (see Fig. 6.21).

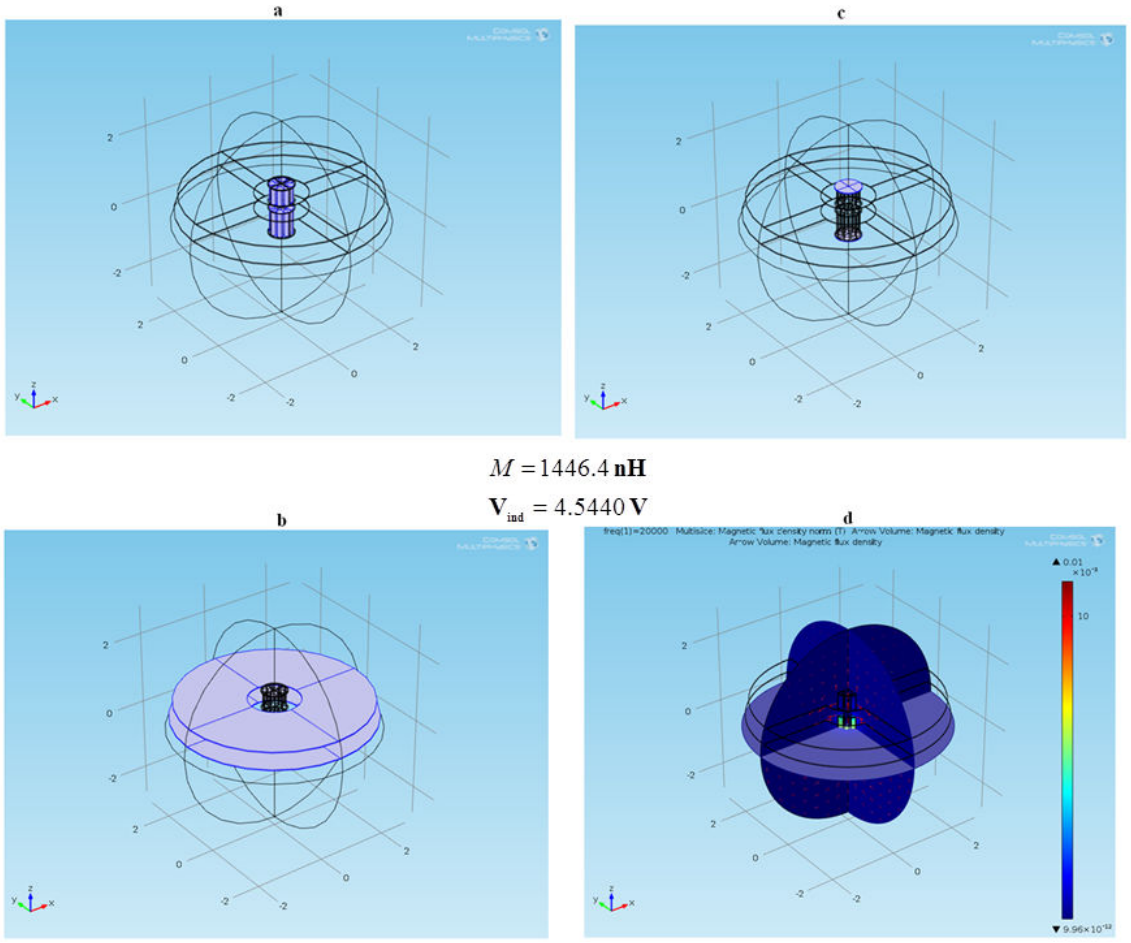

FIGURE 6.20: EV - a complete MCS model with 8 ferrite cores inside
Incorporation of (a) 8 ferrite cores inside (b) structural steel cover (c) underbody structure of EV and the metallic plate that covers the primary coil installed underground, (d) 3-D AC magnetic flux density.

Finally, by taking Fig. 6.15 as the basis for comparison, it is found out that with the incorporation of ferrite cores in the complete MCS models, the performance of the

system is 5 times better (see Figs. 6.15 and 6.19), 10 times (see Figs. 6.15 and 6.20) and 3 times (see Figs. 6.15 and 6.21).

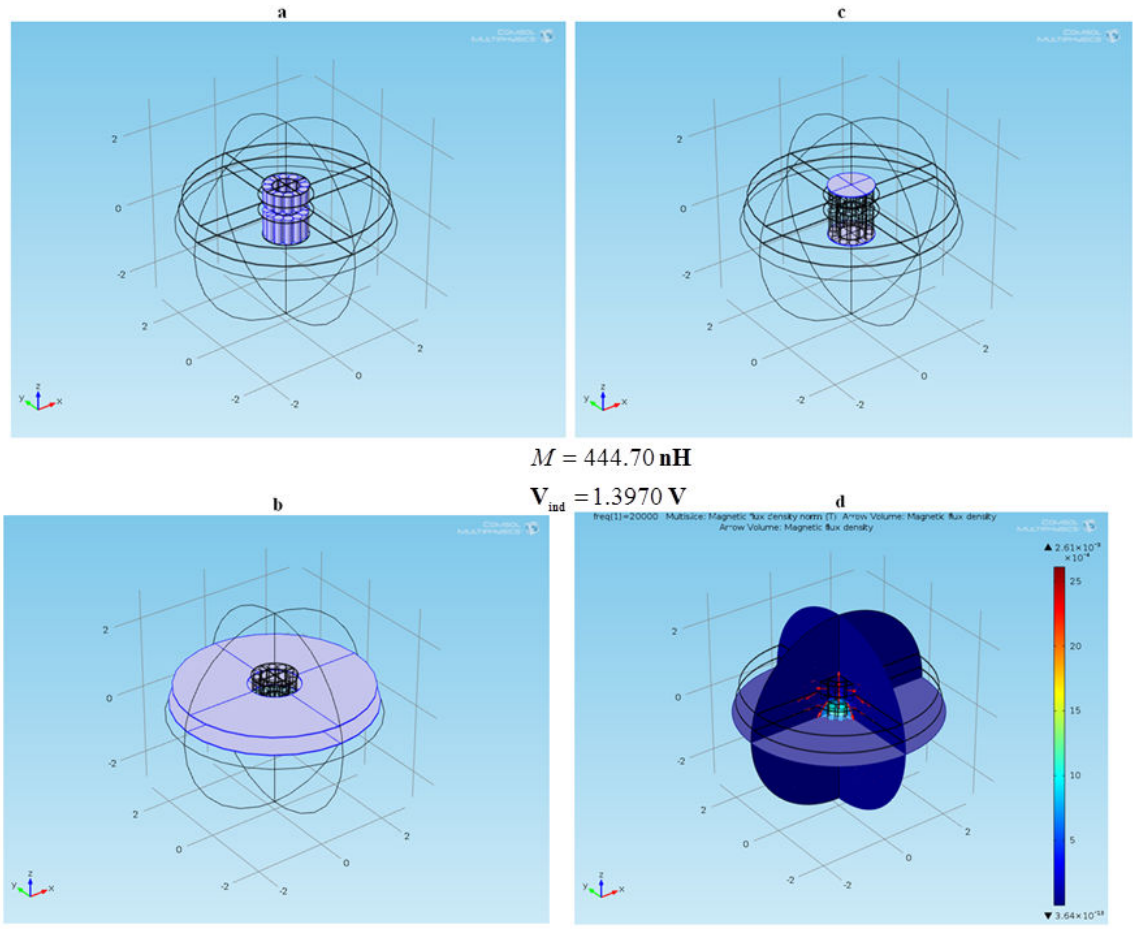

FIGURE 6.21: EV - a complete MCS model with 12 ferrite cores outside Incorporation of (a) 12 ferrite cores outside (b) structural steel cover (c) underbody structure of EV and the metallic plate that covers the primary coil installed underground, (d) 3-D AC magnetic flux density.

TABLE 6.7: Complete MCS models: case study for EVs

Order of performance	Mutual inductance (nH)	Induced voltage (V)	MCS models	Model Performance
1	1446.4	4.5440	compare Figs. 6.15 and 6.20	10
2	685.60	2.1540	compare Figs. 6.15 and 6.19	5
3	444.70	1.3970	compare Figs. 6.15 and 6.21	3

This section presents a complex and realistic MCS model for a loosely-coupled LIPT system: a case study for EVs. In conclusion, the complete MCS models, which incorporate several arrangements of ferrite cores, structural steel cover, metallic part

and chassis for the EV, show that the complete design of MCS model with 8 ferrite cores inside is the most suitable and effective model for the battery charging of EVs.

6.5 EVs: MCS Model with Misalignment

This section presents a more complex and realistic MCS model with misalignment for EVs, and it is implemented based on the best model presented in subsection 6.4.3, which is the complete MCS model with 8 ferrite cores inside (see Figs. 6.22 to 6.27).

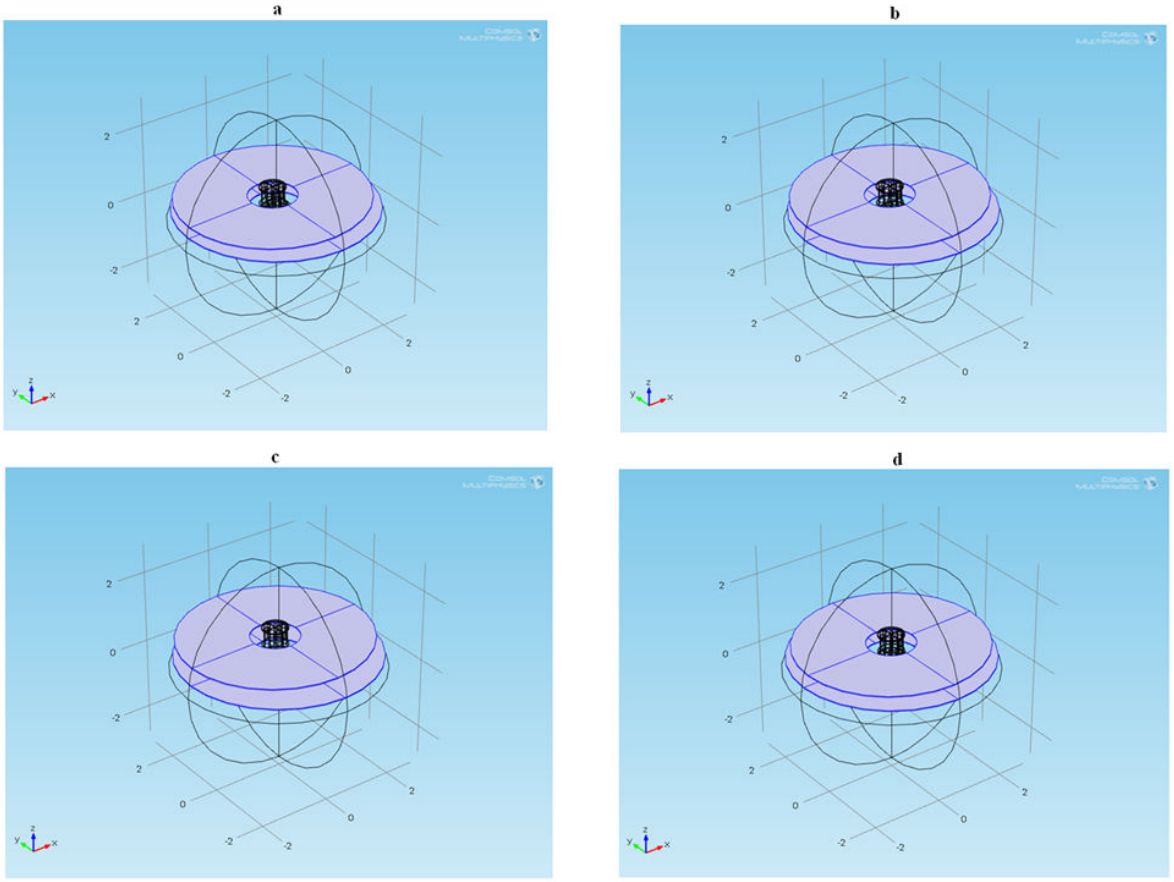

FIGURE 6.22: MCS model with misalignment: $\theta = \frac{\pi}{3}$
(a) $x = -0.1\ m$ and $z = -0.1\ m$, (b) $x = -0.1\ m$ and $z = 0$, (c) $x = -0.1\ m$ and $z = 0.1\ m$, (d) $x = 0$ and $z = -0.1\ m$

To achieve this task, lateral misalignment and coil separation distance respectively with a deviation of $\pm 0.1\ m$ in the x and z directions for a particular angular misalignment of $\theta = \frac{\pi}{3}$ and $\theta = \frac{2\pi}{2.5}$ are studied in this thesis.

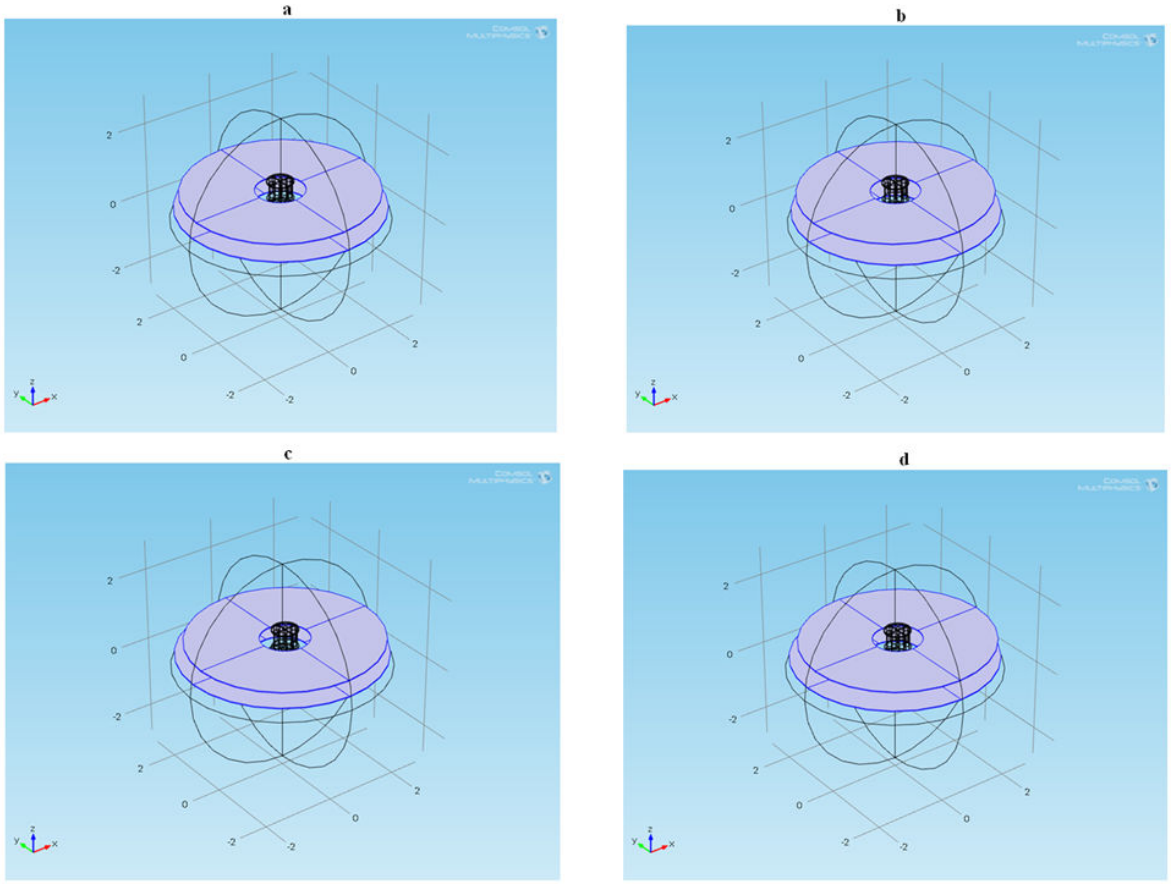

FIGURE 6.23: MCS model with misalignment: $\theta = \frac{\pi}{3}$
(a) $x = 0$ and $z = 0$, (b) $x = 0$ and $z = 0.1\ m$, (c) $x = 0.1\ m$ and $z = -0.1\ m$ and (d) $x = 0.1\ m$ and $z = 0$

The several misaligned MCS models and the results obtained for their mutual inductance and induced voltage are shown in Figs. 6.22 to 6.27. These models consist of air-cored coils with 8 ferrite cores inside, structural steel covering for the bottom part of the primary coil and top part of the secondary coil, metallic plate which covers the primary coil installed underground and the iron plate which serves as the chassis or underbody structure of EVs.

In this section, a more complex and realistic MCS model for EVs are implemented (case studies with several coil separation distances and misalignment). The results (see values for the mutual inductance and induced voltage in Figs. 6.24 and 6.27) obtained show that the best MCS model for EVs (see Fig. 6.20) has the capacity to tolerate the several coil separation distances and misalignment studied in this thesis.

a

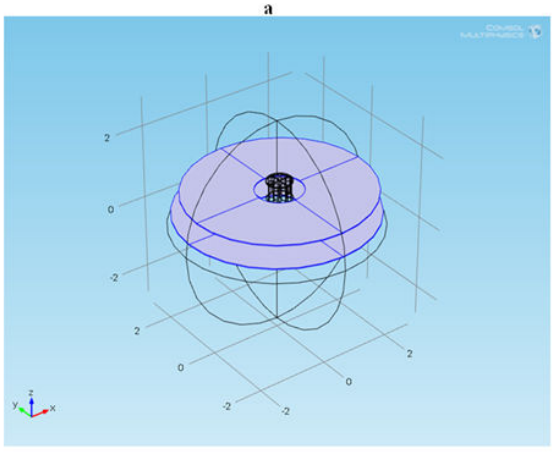

b

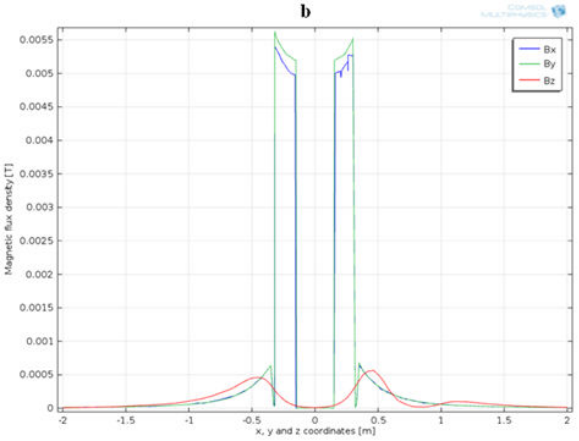

c

Δz (m) \ Δx (m)	**-0.1**	**0**	**0.1**
-0.1	$M = 7252.9$ nH $V_{ind} = 52.405$ V	$M = 3626.5$ nH $V_{ind} = 26.192$ V	$M = 1661.5$ nH $V_{ind} = 12.005$ V
0	$M = 7301.37$ nH $V_{ind} = 53.425$ V	$M = 3650.7$ nH $V_{ind} = 26.712$ V	$M = 1746.7$ nH $V_{ind} = 12.784$ V
0.1	$M = 2900.8$ nH $V_{ind} = 10.521$ V	$M = 1388.0$ nH $V_{ind} = 5.0356$ V	$M = 664.11$ nH $V_{ind} = 2.4110$ V

FIGURE 6.24: Results for MCS model with misalignment: $\theta = \frac{\pi}{3}$
(a) $x = 0.1\ m$ and $z = 0.1\ m$, (b) 1-D plot for magnetic flux density versus x, y and z coordinates, and (d) values for the mutual inductance and induced voltage.

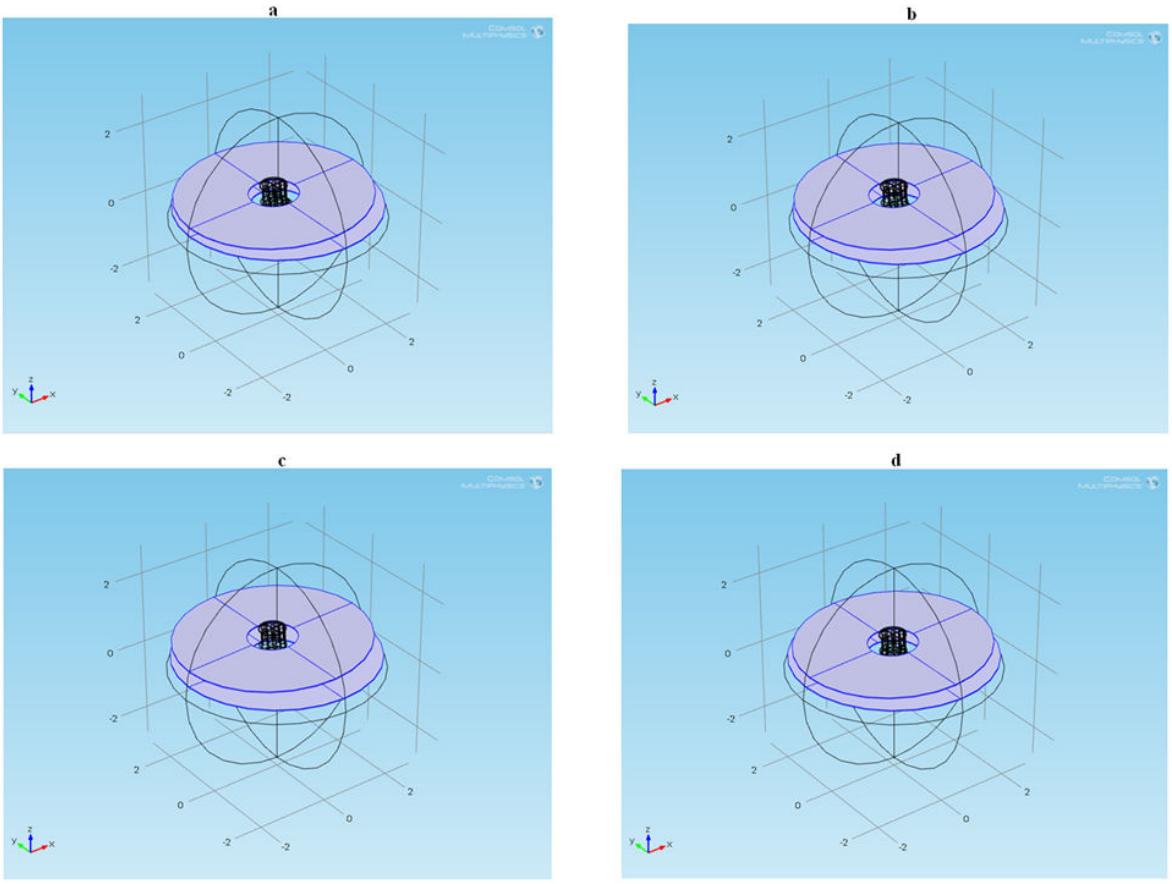

FIGURE 6.25: MCS model with misalignment: $\theta = \frac{2\pi}{2.5}$
(a) $x = -0.1\ m$ and $z = -0.1\ m$, (b) $x = -0.1\ m$ and $z = 0$, (c) $x = -0.1\ m$ and $z = 0.1\ m$, (d) $x = 0$ and $z = -0.1\ m$

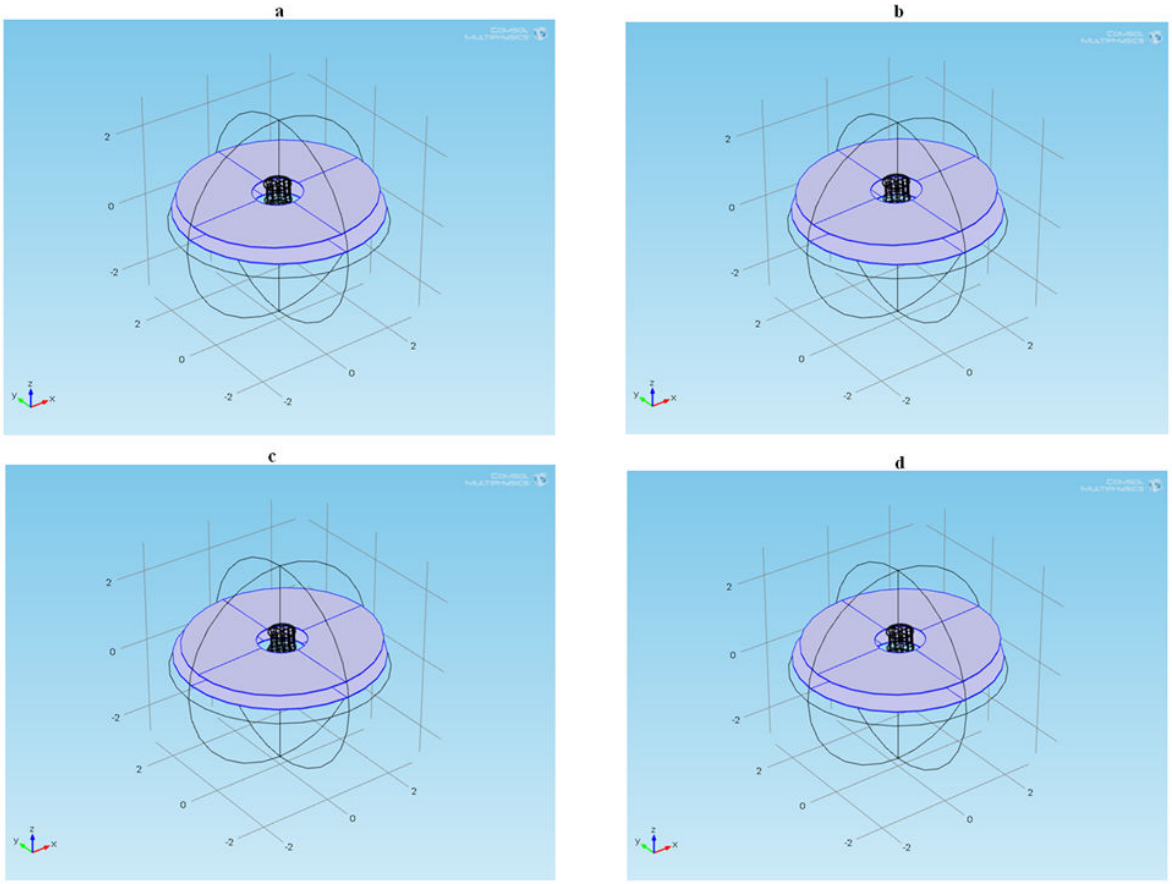

FIGURE 6.26: MCS model with misalignment: $\theta = \frac{2\pi}{2.5}$
(a) $x = 0$ and $z = 0$, (b) $x = 0$ and $z = 0.1\ m$, (c) $x = 0.1\ m$ and $z = -0.1\ m$ and (d) $x = 0.1\ m$ and $z = 0$

a

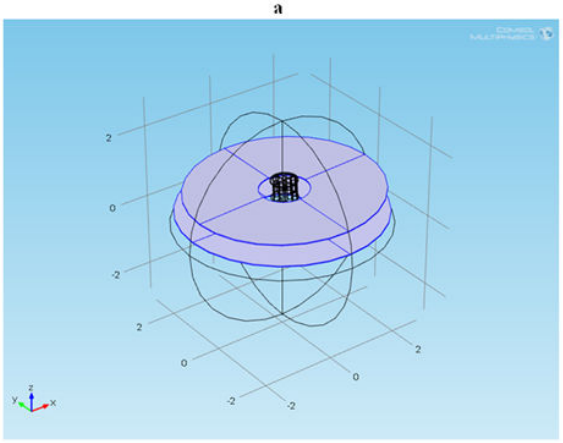

b

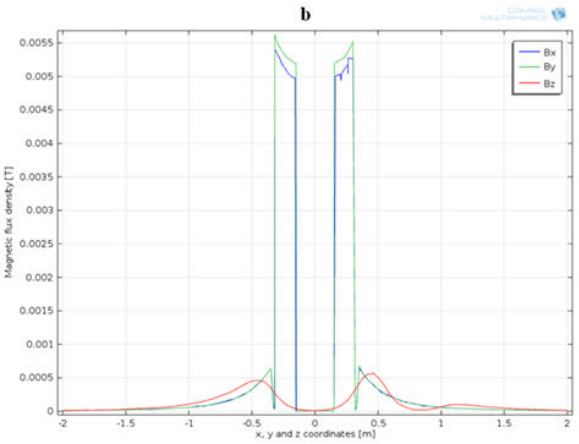

c

Δx (m) / Δz (m)	**-0.1**	**0**	**0.1**
-0.1	$M = 3373.4\,nH$ $V_{ind} = 24.374\,V$	$M = 1686.7\,nH$ $V_{ind} = 12.182\,V$	$M = 772.79\,nH$ $V_{ind} = 5.5837\,V$
0	$M = 3395.9\,nH$ $V_{ind} = 24.849\,V$	$M = 1698.0\,nH$ $V_{ind} = 12.424\,V$	$M = 812.42\,nH$ $V_{ind} = 5.9460\,V$
0.1	$M = 1349.2\,nH$ $V_{ind} = 12.182\,V$	$M = 645.58\,nH$ $V_{ind} = 2.3421\,V$	$M = 308.88\,nH$ $V_{ind} = 1.1213\,V$

FIGURE 6.27: MCS model with misalignment: $\theta = \frac{2\pi}{2.5}$
(a) $x = 0.1\ m$ and $z = 0.1\ m$, (b) 1-D plot for magnetic flux density versus x, y and z coordinates, and (d) values for the mutual inductance and induced voltage.

6.6 Conclusion

The aim of this thesis is to investigate the best design of MCS model that is suitable and effective for the battery charging of EVs and E-bikes.

In this chapter, a more complex and realistic MCS models for a closely and loosely coupled LIPT systems are designed, computed and investigated by using a 3-D FEA package called COMSOL multiphysics. The designed MCS models incorporate air-cored coils with proper configuration of magnetic cores (e.g ferrite), structural steel

covering for the bottom part of the primary coil and top part of the secondary coil and iron plate which serves as a covering for the primary coil installed underground and the chassis or underbody structure of EVs.

Section 6.2 presents the MCS model description for E-bikes (closely-coupled LIPT system) and EVs (loosely-coupled LIPT system). Section 6.3 presents the results of the MCS models for E-bikes. Section 6.4 presents the results of the MCS models for EVs. Section 6.5 presents the results of the MCS model with misalignment: a case study for EVs.

The performance of the designed models are determined by the values of the mutual inductance and induced voltage obtained from COMSOL. Based on that information, the results obtained show that the complete design of MCS model with 12 ferrite cores outside is the most suitable and effective model for the battery charging of E-bikes. Furthermore, the results obtained show that the complete design of MCS model with 8 ferrite cores inside is the most suitable and effective model for the battery charging of EVs. Lastly, the results obtained show that the best MCS model for EVs can tolerate the several coil separation distances and misalignment considered.

Chapter 7

CONCLUSION

Users and owners of electric vehicles (EVs) feel uncomfortable because EVs require sufficient electrical energy battery storage on-board to provide sufficient driving autonomy. Lumped inductive power transfer (LIPT) system is a modern technology that allows the transfer of electric power between its air-cored primary and secondary coils via a high frequency magnetic field to a consuming device. Unlike the conventional plug-in system (see Fig. 2.1), LIPT system is capable of providing a safe, efficient and convenient overnight recharging of EVs. However, its main limiting factor is the poor performance of its magnetic coupling structure (MCS), which is intended to transfer power efficiently. Thus the problem statement of this thesis is to improve the performance of MCS models for a closely and loosely coupled LIPT systems. With the objective of investigating the best design of MCS model for LIPT systems that is suitable and effective for the battery charging of EVs and E-bikes, the following sub-problems are studied:

- Implementation of MATLAB codes to compute the mutual inductance between air-cored FC coils with and without lateral and angular misalignment, and also the computation of the mutual inductance between FC coils arbitrarily positioned with respect to each other.

- MATLAB computation and experimental validation of the magnetic fields between two FC coils.

- Design of computational models of a 3 kW single-phase and 22 kW three-phase IPT models by using MATLAB/Simulink.

- 3-D FEA modelling, computation and investigation of a more complex and realistic MCS of a closely and loosely coupled LIPT systems for E-bikes and EVs respectively.

7.1 Summary of Research Results

Chapter 3 of this thesis presents the rederived models for the computation of the mutual inductance between FC coils with and without lateral and angular misalignment. Also, the computation of the mutual inductance between FC coils arbitrarily positioned in space is presented. MATLAB software is used to obtain the graphical and numerical results presented, and the clarifications concerning the errors made are presented. Generally, the results obtained show that as the values of the coil separation distance and misalignment (e.g. lateral and angular) increase, the value of the mutual inductance M between the coils decreases (see Figs. 3.4 - 3.7 and

Tables 3.1 - 3.2). Thus it is possible for a MCS model to have an increased mutual inductance value provided that the air-cored coils have a reduced diameter and an increased number of turns. Nonetheless, the model presented in this section deals with a non realistic MCS model of LIPT systems for EVs and E-bikes.

In comparison to chapter 3, MATLAB computation for the voltage and current induced in the secondary side of the FC coil is achieved by deriving the models for computing the total magnetic flux and the mutual inductance between the two coils. With the help of the formulated models, it is observed that the values of the magnetic fields as well as Φ_T, M and V can be increased provided a higher frequency AC voltage is supplied to the primary coil, the number of turns of the coils are increased and the diameter of the coils are reduced. The comparison of the results show that the model formulated and experimental measurements implemented in the laboratory are accurate. Nonetheless, it is important to note that the non-conducting magnetic material which covers the coils of the inductive charger is not considered in the formulated model. Thus there is a need to obtain a realistic MCS model.

Unlike in chapters 3 and 4, series-series capacitive compensation is applied to the two sides of the air-cored coils; the results obtained show that with SS capacitive compensation, the power transfer efficiency between the air-cored coils increased by 15.04% due to the partial compensation of the large leakage reactance associated with its primary and secondary coils, and based on that concept, computational models of a 3 kW single-phase and 22 kW three-phase IPT systems for EVs are designed using MATLAB/Simulink. Nonetheless, since the objective of this thesis is to design

a suitable and an effective MCS model of LIPT systems for EVs and E-bikes, it is seen that chapters 3 to 5 deal with a non-realistic MCS model for LIPT systems. This is because the models studied do not incorporate magnetic cores (e.g. ferrite).

In order to recommend a suitable and an effective MCS model that can help transfer electric power more efficiently for the battery charging of EVs and E-bikes, a 3-D finite element analysis (FEA) package called COMSOL multiphysics is used to design, compute and investigate a more complex and realistic MCS model for LIPT systems. The designed MCS models incorporate air-cored coils with proper configuration of ferrite cores, structural steel covering for the bottom part of the primary coil and top part of the secondary coil and lastly, iron plate which serves as a covering for the primary coil installed underground and the chassis or underbody structure of EVs. The performance of the designed models are determined by the values of the mutual inductance and induced voltage obtained from COMSOL. Based on that information, the results obtained show that the complete design of MCS model with 12 ferrite cores outside is the most suitable and effective for the battery charging of E-bikes, and by taking Fig. 6.5 as the basis for comparison, it is found out that the performance of the complete MCS models with 12 ferrite cores outside is 37 times better than in the case without ferrites (see Figs. 6.5 and 6.13). Also, the results obtained show that the complete design of MCS model with 8 ferrite cores inside is the most suitable and effective for the battery charging of EVs, and by taking Fig. 6.15 as the basis for comparison, it is found out that the performance of the complete MCS models with 8 ferrite cores inside is 10 times better than in the case without ferrites (see Figs. 6.15 and 6.20).

Finally, MCS model with misalignment is implemented based on the complete design of MCS model with 8 ferrite cores inside, and the results obtained show that the model can tolerate the several coil separation distances and misalignment considered.

7.2 Recommendation for Future Research Work

This research study is worth doing because of the useful and relevant information it provides to electrical engineers and researchers in the field of electromagnetic coupling structure for LIPT systems (most especially, case studies for EVs and E-bikes).

Concerning the design of electromagnetic systems (e.g. LIPT systems), leakage magnetic fields are one of the primary issues to be studied. This is because they contribute to various undesirable effects in many electromagnetic applications. In order to reduce such fields, one of the future research studies is to investigate the leakage magnetic fields due to the MCS models for LIPT systems (most especially, case studies for E-bikes and EVs).

Furthermore, based on the objective of this thesis, another future research work is to validate the results obtained in Chapter 6. Firstly, this will be done by implementing a physical prototype of MCS model for a closely-coupled LIPT system (case study for E-bike battery charging) and secondly, by constructing MCS model for a loosely-coupled LIPT system (case study for EV battery charging).

Finally, an important future research study concerning the design of MCS models for LIPT systems is to evaluate the radiation of electromagnetic fields on human body.

Bibliography

Acero J., Carretero C., Lope I., Alonso R., Lucia O., & Burdio J.M. 2013. Analysis of the mutual inductance of planar-lumped inductive power transfer systems. *Industrial Electronics, IEEE Transactions on*, 60(1):410–420.

Aditya K., Peschiera B., Youssef M., & Williamson S.S. 2015. Modelling and calculation of key design parameters for an inductive power transfer system using finite element analysis-a comprehensive discussion. In *Transportation Electrification Conference and Expo (ITEC), 2015 IEEE*, 1–6. IEEE.

Agbinya J.I. 2012. *Wireless power transfer*. River Publishers.

Akyel C., Babic S.I., & Mahmoudi M.M. 2009. Mutual inductance calculation for non-coaxial circular air coils with parallel axes. *Progress In Electromagnetics Research*, 91:287–301.

Amos A.O., Yskandar H., Yasser A., & Karim D. 2013a. Computation of magnetic field and force between circular filaments arbitrarily positioned in space. In *Information Science, Computing and Telecommunications (PACT), 2013 Pan African International Conference on*, 110–115. IEEE.

Amos A.O., Yskandar H., Yasser A., & Karim D. 2013b. Computation of the mutual inductance between circular filaments with coil misalignment. In *AFRICON, 2013*, 1–5. IEEE.

Amos A.O., Yskandar H., Yasser A., & Karim D. 2013c. Effects of misalignment between filamentary circular coils arbitrarily positioned in space. In *Information Science, Computing and Telecommunications (PACT), 2013 Pan African International Conference on*, 200–205. IEEE.

Amos A.O., Yskandar H., Yasser A., & Karim D. 2014a. Effects of coil misalignments on the magnetic field and magnetic force components between circular filaments. *Journal of Machine to Machine Communications*, 1:31–50.

Amos A.O., Yskandar H., Yasser A., & Karim D. 2014b. Investigating the impacts of lateral and angular misalignments between circular filaments. *Journal of Machine to Machine Communications*, 1:83–104.

Anele A., Hamam Y., Chassagne L., Linares J., Alayli Y., & Djouani K. 2015a. Computation of the mutual inductance between air-cored coils of wireless power transformer. In *Journal of Physics: Conference Series*, volume 633, 12011–12016. IOP Publishing.

Anele A., Hamam Y., Chassagne L., Linares J., Alayli Y., & Djouani K. 2015b. Computational models of an inductive power transfer system for electric vehicle battery charge. In *Journal of Physics: Conference Series*, volume 633, 12010–12017. IOP Publishing.

Anele A., Hamam Y., Chassagne L., Linares J., Alayli Y., & Djouani K. 2015c. Evaluation of the magnetic fields and mutual inductance between circular coils arbitrarily positioned in space. In *Journal of Physics: Conference Series*, volume 633, 12012–12017. IOP Publishing.

Auvigne C.B. 2015. Electrical and magnetical modeling of inductive coupled power transfer systems.

Babic S.I. & Akyel C. 2012. Magnetic force between inclined circular loops (lorentz approach). *Progress In Electromagnetics Research B*, 38:333–349.

Babic S.I., Sirois F., & Akyel C. 2009. Validity check of mutual inductance formulas for circular filaments with lateral and angular misalignments. *Progress In Electromagnetics Research M*, 8:15–26.

Barth H., Jung M., Braun M., Schmülling B., & Reker U. 2011. Concept evaluation of an inductive charging system for electric vehicles. In *3rd European Conference Smart Grids and E-Mobility, Munich, Germany.*

Boys J. & Covic G. 2012. Ipt fact sheet series: No. 1–basic concepts.

Budhia M., Boys J.T., Covic G., Huang C.Y., et al. 2013. Development of a single-sided flux magnetic coupler for electric vehicle ipt charging systems. *Industrial Electronics, IEEE Transactions on*, 60(1):318–328.

Budhia M., Covic G., Boys J.T., et al. 2011. Design and optimization of circular magnetic structures for lumped inductive power transfer systems. *Power Electronics, IEEE Transactions on*, 26(11):3096–3108.

Butterworth S. 1916. Liii. on the coefficients of mutual induction of eccentric coils. *The London, Edinburgh, and Dublin Philosophical Magazine and Journal of Science*, 31(185):443–454.

Chopra S. & Bauer P. 2011. Analysis and design considerations for a contactless power transfer system. In *Telecommunications Energy Conference (INTELEC), 2011 IEEE 33rd International*, 1–6. IEEE.

Conway J.T. 2008. Noncoaxial inductance calculations without the vector potential for axisymmetric coils and planar coils. *Magnetics, IEEE Transactions on*, 44(4):453–462.

Covic G., Elliott G., Stielau O., Green R., & Boys J. 2000. The design of a contact-less energy transfer system for a people mover system. In *Power System Technology, 2000. Proceedings. PowerCon 2000. International Conference on*, volume 1, 79–84. IEEE.

Dai J. & Ludois D.C. 2015. A survey of wireless power transfer and a critical comparison of inductive and capacitive coupling for small gap applications. *Power Electronics, IEEE Transactions on*, 30(11):6017–6029.

Fotopoulou K. & Flynn B.W. 2011. Wireless power transfer in loosely coupled links: Coil misalignment model. *Magnetics, IEEE Transactions on*, 47(2):416–430.

García X.d.T., Vázquez J., & Roncero-Sánchez P. 2015. Design, implementation issues and performance of an inductive power transfer system for electric vehicle chargers with series–series compensation. *Power Electronics, IET*,

8(10):1920–1930.

Grover F.W. 1944. The calculation of the mutual inductance of circular filaments in any desired positions. *Proceedings of the IRE*, 32(10):620–629.

Grover F.W. 1946. *Inductance calculations: working formulas and tables*. Courier Corporation.

Han Y. & Wang X. 2015. Calculation of mutual inductance based on 3d field and circuit coupling analysis for wpt system. *International Journal of Control & Automation*.

Hasanzadeh S. & Vaez-Zadeh S. 2015. A review of contactless electrical power transfer: Applications, challenges and future trends. *Automatika–Journal for Control, Measurement, Electronics, Computing and Communications*, 56(3).

Hata T. & Ohmae T. 2004. Position detection method using induced voltage for battery charge on autonomous electric power supply system for vehicles. In *Advanced Motion Control, 2004. AMC'04. The 8th IEEE International Workshop on*, 187–191. IEEE.

Huang C.Y., Boys J.T., Covic G., Budhia M., et al. 2009. Practical considerations for designing ipt system for ev battery charging. In *Vehicle Power and Propulsion Conference, 2009. VPPC'09. IEEE*, 402–407. IEEE.

Huang C.Y., James J.E., Covic G., et al. 2015. Design considerations for variable coupling lumped coil systems. *Power Electronics, IEEE Transactions on*, 30(2):680–689.

Hui S. & Ho W.W. 2005. A new generation of universal contactless battery charging platform for portable consumer electronic equipment. *Power Electronics, IEEE Transactions on*, 20(3):620–627.

Kalwar K.A., Aamir M., & Mekhilef S. 2015. Inductively coupled power transfer (icpt) for electric vehicle charging–a review. *Renewable and Sustainable Energy Reviews*, 47:462–475.

Khaligh A. & Dusmez S. 2012. Comprehensive topological analysis of conductive and inductive charging solutions for plug-in electric vehicles. *Vehicular Technology, IEEE Transactions on*, 61(8):3475–3489.

Kim C.G., Seo D.H., You J.S., Park J.H., & Cho B.H. 2001. Design of a contactless battery charger for cellular phone. *Industrial Electronics, IEEE Transactions on*, 48(6):1238–1247.

Kim K.B., Levi E., Zabar Z., & Birenbaum L. 1997. Mutual inductance of non-coaxial circular coils with constant current density. *Magnetics, IEEE Transactions on*, 33(5):4303–4309.

Kim K.Y. 2012. Wireless power transfer-principles and engineering explorations. *Janeza Trdine*, 9:51000.

Klontz K.W., Divan D.M., & Novotny D.W. 1995. An actively cooled 120 kw coaxial winding transformer for fast charging electric vehicles. *Industry Applications, IEEE Transactions on*, 31(6):1257–1263.

Koo K.W., Kim D.H., Woo D.G., & Lee B.K. 2012. Topology comparison for 6.6 kw on board charger: Performance, efficiency, and selection guideline. In *Vehicle Power and Propulsion Conference (VPPC), 2012 IEEE*, 1520–1524. IEEE.

Laouamer R., Brunello M., Ferrieux J., Normand O., & Buchheit N. 1997. A multi-resonant converter for non-contact charging with electromagnetic coupling. In *Industrial Electronics, Control and Instrumentation, 1997. IECON 97. 23rd International Conference on*, volume 2, 792–797. IEEE.

Liu X. & Hui S.R. 2007. Equivalent circuit modeling of a multilayer planar winding array structure for use in a universal contactless battery charging platform. *Power Electronics, IEEE Transactions on*, 22(1):21–29.

Madzharov N.D. & Tonchev A.T. ???? Ipt station for static and dynamic charging of electric vehicles.

Maxwell J.C. 1881. *A treatise on electricity and magnetism*, volume 1. Clarendon press.

Miller J.M., Onar O.C., White C., Campbell S., Coomer C., Seiber L., Sepe R., & Steyerl A. 2014. Demonstrating dynamic wireless charging of an electric vehicle: The benefit of electrochemical capacitor smoothing. *Power Electronics Magazine, IEEE*, 1(1):12–24.

Mou X. & Sun H. 2015. Wireless power transfer: Survey and roadmap. In *Vehicular Technology Conference (VTC Spring), 2015 IEEE 81st*, 1–5. IEEE.

Musavi F. & Eberle W. 2014. Overview of wireless power transfer technologies for electric vehicle battery charging. *Power Electronics, IET*, 7(1):60–66.

Nakao F., Matsuo Y., Kitaoka M., & Sakamoto H. 2002. Ferrite core couplers for inductive chargers. In *Power Conversion Conference, 2002. PCC-Osaka 2002. Proceedings of the*, volume 2, 850–854. IEEE.

Neves A., Sousa D.M., Roque A., & Terras J. 2011. Analysis of an inductive charging system for a commercial electric vehicle. In *Power Electronics and Applications (EPE 2011), Proceedings of the 2011-14th European Conference on*, 1–10. IEEE.

Raval P., Kacprzak D., & Hu A.P. 2014. Computational finite element software assisted development of a 3d inductively coupled power transfer system. *Advanced Electromagnetics*, 2(3):11–18.

Schmuelling B., Cimen S.G., Vosshagen T., & Turki F. 2012. Layout and operation of a non-contact charging system for electric vehicles. In *Power Electronics and Motion Control Conference (EPE/PEMC), 2012 15th International*, 1–7. IEEE.

Sergeant P. et al. 2008. Inductive coupler for contactless power transmission. *Electric Power Applications, IET*, 2(1):1–7.

Severns R., Yeow E., Woody G., Hall J., & Hayes J. 1996. An ultra-compact transformer for a 100 w to 120 kw inductive coupler for electric vehicle

battery charging. In *Applied Power Electronics Conference and Exposition, 1996. APEC'96. Conference Proceedings 1996., Eleventh Annual*, volume 1, 32–38. IEEE.

Snow C. 1954. *Formulas for computing capacitance and inductance*, volume 544. US Govt. Print. Off.

Stielau O.H. & Covic G.A. 2000. Design of loosely coupled inductive power transfer systems. In *Power System Technology, 2000. Proceedings. PowerCon 2000. International Conference on*, volume 1, 85–90. IEEE.

Su Y., Liu X., & Hui S.R. 2009. Mutual inductance calculation of movable planar coils on parallel surfaces. *Power Electronics, IEEE Transactions on*, 24(4):1115–1123.

Subotic I. & Levi E. 2015. A review of single-phase on-board integrated battery charging topologies for electric vehicles. In *Electrical Machines Design, Control and Diagnosis (WEMDCD), 2015 IEEE Workshop on*, 136–145. IEEE.

Van der Pijl F.F., Ferreira J., Bauer P., Polinder H., et al. 2006. Design of an inductive contactless power system for multiple users. In *Industry Applications Conference, 2006. 41st IAS Annual Meeting. Conference Record of the 2006 IEEE*, volume 4, 1876–1883. IEEE.

Villa J.L., Sallán J., Llombart A., & Sanz J.F. 2009. Design of a high frequency inductively coupled power transfer system for electric vehicle battery charge. *Applied Energy*, 86(3):355–363.

Wang C.S., Stielau O.H., Covic G., et al. 2000. Load models and their application in the design of loosely coupled inductive power transfer systems. In *Power System Technology, 2000. Proceedings. PowerCon 2000. International Conference on*, volume 2, 1053–1058. IEEE.

Wang C.S., Stielau O.H., Covic G., et al. 2005. Design considerations for a contactless electric vehicle battery charger. *Industrial Electronics, IEEE Transactions on*, 52(5):1308–1314.

Wei X., Wang Z., & Dai H. 2014. A critical review of wireless power transfer via strongly coupled magnetic resonances. *Energies*, 7(7):4316–4341.

Wu H.H., Gilchrist A., Sealy K., Israelsen P., & Muhs J. 2011. A review on inductive charging for electric vehicles. In *Electric Machines & Drives Conference (IEMDC), 2011 IEEE International*, 143–147. IEEE.